Image Cover Sheet

CLASSIFICATION	SYSTEM NUMBER
UNCLASSIFIED	58878

TITLE

ELECTROMAGNETIC REMOTE SENSING: LOW FREQUENCY ELECTROMAGNETICS

System Number:

Patron Number:

Requester:

Notes:

DSIS Use only:

Deliver to: TC

National Defence / Défense nationale

UNCLASSIFIED

DEFENCE RESEARCH ESTABLISHMENT SUFFIELD
RALSTON, ALBERTA

SUFFIELD SPECIAL PUBLICATION NO. 124

ELECTROMAGNETIC REMOTE SENSING

LOW FREQUENCY ELECTROMAGNETICS

John E. McFee
Ordnance Detection Group

PCN 031SD

January 1989

UNCLASSIFIED

Canada

ELECTROMAGNETIC REMOTE SENSING
Low Frequency Electromagnetics

John E. McFee
Ordnance Detection Group

Defence Research Establishment Suffield
Ralston AB, Canada
T0J 2N0

Abstract

A series of lectures are presented on the topic of the location and identification of compact objects by low frequency electromagnetics. These lectures were presented as a portion of two graduate level courses in electrical engineering at the University of Toronto in 1985 and 1987. Magnetostatics, electrostatics and electromagnetic induction techniques are discussed in detail.

Forward

In the Fall of 1985, a pilot course was offered to graduate students in electrical engineering at the University of Toronto. The course, entitled "Topics in Electromagnetic Theory : Latest Techniques in Remote Sensing", was taught by Professors J.L. Yen and K. Iizuka of the Department of Electrical Engineering and me. Professor Yen lectured on microwave radiometry, Professor Iizuka covered subsurface rada and I dealt with low frequency electromagnetics.

The material met with considerable enthusiasm to the end that it was offered again in the Fall of 1987 under the new title "Electromagnetic Remote Sensing" with the same lecturers and general topics.

These notes are a compilation of the material that was presented for the low frequency electromagnetic remote sensing portion of both courses. The general subject has been covered extensively in textbooks in the context of geological exploration. Objects of interest are typically considered to be very large, often infinite in extent in one or two dimensions. I have approached these lectures from the viewpoint of the location and identification of relatively small compact objects by low frequency electromagnetics. This is an area which has been surprisingly neglected in textbooks even though it is a very relevant topic which is of practical interest to many researchers in areas as diverse as submarine detection, pipe location, archaeology and mine and artillery shell detection. I hope these notes will fill that gap in the available textbooks.

Finally, I must thank my colleague Dr. Yogadhish Das. Much of the work presented in these notes represents published (and some unpublished) collaborative research by the two of us. Our general discussions have been invaluable and have had a distinct influence on these notes.

1 Low Frequency Electromagnetic Remote Sensing

The present course is concerned with remote sensing, particularly as it relates to electromagnetics. Remote sensing may be defined as the acquisition of information about an object without physical contact. Although a host of sensors might qualify as remote sensors under this broad definition, remote sensing usually refers to the collection and processing of information about the earth or objects on the earth through the use of photographs and sensor data acquired from a satellite or aircraft. We will refer to this as "classical remote sensing (CRS)".

The problem of detecting objects concealed from view at distances of between, say, 1 and 100 times a characteristic dimension of the object is an area of remote sensing which is of much interest. We shall call this problem, for lack of a better term, "quasi- remote sensing (QRS)". The boundary between QRS and CRS is fuzzy. Computed axial tomography might be considered to QRS when used to image the body or a buried object in soil, but tomography using radar signals to image an airplane lies more in the realm of CRS. Detecting ore bodies using an airborne electromagnetic induction detector might be considered CRS but locating the same bodies from the ground using the same type of detector might be QRS. We shall not attempt to clearly delineate the boundary between CRS and QRS but rather shall give representative examples of the latter. Some of these are:

1. Geophysical exploration of compact ore bodies from the ground (magnetics, electromagnetic induction, electrostatics)
2. Nondestructive testing (electromagnetic induction, neutron tomography, x-ray imaging)
3. Detection of submarines from aircraft or ships (magnetics, electromagnetic induction)
4. Detection of land vehicles using buried sensors (magnetics, electromagnetic induction)
5. Detection of buried ordnance (artillery shells and mines) (low frequency electromagnetics)
6. Detection of trapped miners (low frequency electromagnetics)
7. Imaging of body parts (x-rays, electrostatics, acoustics)
8. Measurement of electric fields of body organs (electrocardiogram, electroencephalogram)
9. Measurement of magnetic fields of body organs (magnetocardiogram, magnetoencephalogram)
10. Measurement of contaminants in the body such as dust in lungs or metal fragments (magnetics, electromagnetic induction)

In the previous list, some technologies applicable to each problem have been noted, although this is by no means an exhaustive compilation. To illustrate the wide spectrum of methods available for QRS, we shall focus for a moment on the problem of detecting unexploded ordnance. Table 1.1 shows the main characteristics of the three major types of unexploded ordnance. Keeping these traits in mind, one can think of a number of possible methods which could conceivably detect buried ordnance. These are shown in Table 1.2, where they are categorized as "Q" or "R" for quasi-remote or remote sensing.

A discussion of the principles and techniques behind all the methods listed is beyond the scope of the course, however, details may be found in [22].

In keeping with the theme of the course, we shall restrict ourselves to quasi-remote sensing methods which are related to electromagnetism. Although one could argue eloquently that all the above methods are indirectly related to electromagnetism, we shall be less philosophical and focus on those that directly involve the generation and/or measurement of electromagnetic fields. These include magnetostatics, electrostatics, electromagnetic induction, ground penetrating radar, magnetic resonance, and the sensing of ultraviolet, visible and thermal infrared radiation. The last three are usually considered to be classical remote sensing techniques and ground penetrating radar is covered elsewhere in the course. Although magnetic resonance involves the generation and sensing of radio frequency radiation coupled with static

magnetic fields, it requires a quantum mechanical treatment and could easily fill one or more courses by itself.

Thus, we will restrict this portion of the course to magnetostatics, electrostatics and electromagnetic induction, particularly as they apply to detecting nearby concealed objects. In particular, we shall concentrate on "compact" objects, that is, those which have a finite, closed bounding surface and hence are finite in extent. All three methods are in the low frequency portion of the EM spectrum (DC to sub-RF). This is necessary because the materials concealing the object of interest attenuate electromagnetic radiation and the attenuation generally increases with frequency. For example, Table 1.3 shows the skin depth at a few frequencies for two of the most common barriers encountered in practice, saline (the major EM attenuating constituent of the body) and soil.

Since minimum torso thickness is approximately 0.16 m and minimum soil penetration depths are of the order of 1 to 2 m, solely from the standpoint of signal attenuation it is desirable to use frequencies less than 1 MHz. There is, however, a tradeoff. Because of the small distances and long wavelengths, measurements are usually in the near field. Thus, the approximations of geometrical or physical optics do not hold and imaging of a source is not a straightforward matter. In fact, as we shall see, the inverse problem at these low frequencies is quite challenging.

2 Magnetostatic Methods

2.1 Introduction

The object of magnetostatic methods is to measure the static magnetic field associated with a ferrous object and to use this information to locate and identify the object.[1] Ferrous objects, when placed in a magnetic field, such as that of the earth, acquire magnetization of their own. This is normally referred to as "induced magnetization". The magnitude and direction of the induced magnetization is a function of the ferromagnetic susceptibility of the body, its shape and its orientation with respect to the ambient field. Ferrous objects may also have permanent or intrinsic magnetization, usually called "remnant magnetization". Remnant magnetization is a function solely of the thermal, mechanical and geomagnetic history of the object.

We will be dealing primarily with "compact" objects. The spatial extent of the measureable fields associated with such objects is generally less than a few meters and the time taken to measure the fields is less than a minute. It is important that the earth's field not change significantly during that period.

2.2 Geomagnetic Field

When the geographical variations are averaged out, the earth's magnetic field is very similar to that of a magnetic dipole located $\sim$ 400 km ($\sim \frac{1}{16}$ of the earth's radius) due north of the geometrical center of the earth (Fig. 2.1, Table 2.1). Its axis lies in the meridian plane defined by 69° W and is tilted 11° from the geographical N-S axis. The south pole of the dipole points toward geographical north. The magnitude of the dipole moment is approximately 8×10^{22} A$\cdot$m^2 which produces an average polar field of 65000 nanoTeslas (nT) and an average equatorial field of 35000 nT at the earth's surface (Figs. 2.2, 2.3). This average geomagnetic field is mainly due to currents in the highly conductive core of the earth (self-exciting dynamo action of thermal currents)

The geomagnetic field possesses a high degree of spatial uniformity.[2] For example, near latitude 45°N where F is approximately 45000 nT, the field gradient is approximately 20 nT/km in altitude and 5 nT/km in latitude.[3] If the sensor is less than 5 m above ground surface, inhomogeneity of magnetic properties of soil and magnetotelluric currents may disturb the local spatial uniformity. Buried ferrous objects, geological anomalies and pockets of residual magnetization (the latter sometimes the result

[1] Static magnetic fields are measured for other reasons too. For example one can study the field itself as in interplanetary field measurements or determine current distributions within the human body from biomagnetic measurements.

[2] This is because large variations are unlikely over the large volumes of fluid in the earth's core and the high core temperature eradicates large contrasts after a short time.

[3] The horizontal gradient $\sim 0 - 10$nT/km from equator to pole; -0.03 nT/m at magnetic poles; -0.015 nT/m at magnetic equator; or $\pm 0.047F$ nT/m (+ north of equator, - south, F in Oe).

of currents due to ancient lightning strikes) will also disturb the uniformity but may be detectable at standoffs greater than 5 m.

Temporal fluctuations are 25% attributable to currents internal to the earth and 75% due to external currents. The latter are mainly located in the ionosphere and variations are caused primarily by fluctuations in the solar wind. The internal and external currents are coupled and lead to a complex temporal variation which can be resolved into several components (Figs. 2.4-2.6):

1. **Secular variations:** Occur at a rate of typically 30 nT/year.

2. **Diurnal variations:** At mid-latitudes, F decreases rapidly soon after sunrise, reaches a minimum at noon and increases during afternoon and night. The amplitude of oscillation is a maximum in June ($\sim \pm 25$ nT) and is minimum in January ($\sim \pm 2.5$ nT). The direction of the field also changes by a similar amount.[4]

3. **Fast variations (micropulsations):** There are several types including Eschenhagen fluctuations (amplitude $\sim$ 0.5 - 5.0 nT, period $\sim$ 25 sec, total duration $\sim$ few minutes); hydromagnetic pearls (amplitude $\sim$ 0.02 nT, period $\sim$ 0.3 - 3. sec); oscillation of the earth/ionosphere cavity (amplitude $\sim$ 0.002 nT, period $\sim$ 0.025 - 0.2 sec).

4. **Exceptional variations (magnetic storms):** These happen several times per year and are linked with solar activity. In fact, they occur $\sim$30 hr after strong pulse-like eruptions on the solar surface (solar flares). The typical variations are from 500 - 1500 nT with a wide range of frequency components. In extreme cases, the fluctuations are so strong as to produce visible deflections in compasses.[5] During magnetic storms, the only thing that can be measured are magnetic storms. Such storms may last several hours.

2.3 Interplanetary Field

Remote sensing also includes measurements in outer space and magnetic measurements are a very important component. There are three main areas of interest:

1. $\mathbf{300km \leq r \leq 800km}$: Measurement of the geomagnetic field is of interest, particularly small Gaussian deviations from the dipole model. Most of the geographical heterogeneity has been smoothed out at this height.

2. $\mathbf{1000km \leq r \leq 20R_E}$: This includes the Van Allen radiation belts. The field is generally dipolar, being approximately 300 nT at $5R_E$ and 10 nT at $20R_E$ (R_E is the radius of the earth, $\approx$ 6400 km).[6] Here, deviations due to intense ionic currents produced by the belts are of interest. (Fig. 2.7)

3. $\mathbf{r \geq 20R_E}$: Field values are less well known in this region, but are typically 5 nT. Spatial and temporal variations are of the order of 1 nT and are due to phenomena associated with the solar wind.

2.4 Magnetic Units

The subject of electromagnetic units is a thorny one and no where is this more evident than for magnetic units. Historical reasons brought about the plethora of units which has led to considerable confusion. The reader can remove much of the mystery concerning magnetic units by referring to the excellent discussion by Jackson [5]. Here we shall only list the units which are normally used (Table 2.2). Fortunately, SI units are now considered to be the standard for all but certain theoretical physics applications and we will use them in this course. SI units are in boldface in Table 2.2.

[4] As a crude estimate of the maximum angular change, $\Delta\theta \sim \cos^{-1}\left(\frac{60000}{60025}\right) \sim 1.7^{\circ}$.

[5] The magnetic storm of 1859 produced $(\Delta F/F) \sim 10\%$.

[6] The field obeys an r^{-3} law.

2.5 Fields of Magnetic Anomalies

Deviations of the measured magnetic field due to sources other than those of geomagnetic origin previously mentioned are usually called "anomaly fields" or "magnetic anomalies". Geological anomalies, due to ore bodies, are typically in the range of 100 - 1000 nT. Virtually all magnetic anomalies are due to magnetite concentrations which are associated with the ore of interest (gold, asbestos, uranium-niobium).

Magnetite, being ferrimagnetic, has a magnetic susceptibility typically between 1.2 and 13. Ferromagnetic materials have susceptibilities almost always greater than 50 in the earth's field. Man-made ferromagnetic objects have much smaller dimensions than magnetite formations but sensors can usually get much closer to them. Thus, on the whole, the fields associated with ferromagnetic objects of interest tend to be of the same order of magnitude as geological anomalies.

Typical nongeological objects of interest may include armoured vehicles (peak field $\sim$ 10000 nT), submarines ($\sim$ 1 - 10 nT), buried mines and artillery shells ($\sim$ 10 - 1000 nT), archaeological artifacts, parts of the human body ($\leq 10^{-2}$ nT)(Fig. 2.8).

2.6 Methods of Detection

Sensors which measure magnetic fields are called magnetometers, although usually the term is reserved for sensors measuring fields less than the typical geomagnetic field. Generally, there are two types of magnetometer - vector sensors and total field sensors. The former, which include fluxgate sensors, optical fiber interferometers, thin film sensors and Superconducting Quantum Interference Devices or SQUIDs measure a single component of the field. The latter, which includes all magnetic resonance magnetometers (proton precession, optically pumped alkali vapour), measure the magnitude of the field but not its direction. Fig. 2.8 shows minimum sensitivities of typical magnetometers and clearly several of these are sufficiently sensitive for our purposes.

Principles of operation of various magnetometers are beyond the scope of these lectures, but this information may be found in the bibliographic references. As an example, the operation of a commonly used vector magnetometer, the fluxgate, is illustrated in Fig. 2.9.

In general, if the anomaly field is denoted by $\vec{b} = (b_1, b_2, b_3)$and the earth's field is $\vec{b_0} = (b_{01}, b_{02}, b_{03})$, then a vector magnetometer would measure

$$b_{vj} = b_{0j} + b_j \quad j = 1, 2 \text{ or } 3 \tag{1}$$

whereas a total field magnetometer would measure

$$b_t = \left\| \vec{b_0} + \vec{b} \right\| = \left(b_0^2 + b^2 + 2\vec{b_0} \cdot \vec{b} \right)^{1/2} \tag{2}$$

Generally $b_0 \gg b$ and a Taylor expansion can be performed. We get

$$b_t \approx b_0 + \hat{\gamma} \cdot \vec{b} + \frac{1}{2b_0} \left[b^2 - \left(\hat{\gamma} \cdot \vec{b} \right)^2 \right] - \frac{1}{2b_0^2} \left[\hat{\gamma} \cdot \vec{b} \right] \left[b^2 - \left(\hat{\gamma} \cdot \vec{b} \right)^2 \right] + \cdots \tag{3}$$

where

$$\hat{\gamma} = b_0^{-1} \vec{b_0} \tag{4}$$

Thus to first order, a total field magnetometer measures the magnitude of the earth's field plus the projection of the magnitude of the anomaly field along the direction of the earth's field vector.

The chief advantage of total field magnetometers is that they are insensitive to small changes in the orientation of the sensor. Vector magnetometers will suffer large baseline fluctuations when rotated by only a small angle, due to the large ambient field (Fig. 2.10).

One way of eliminating such baseline fluctuations is to use two sensors, precisely aligned and spaced far enough apart that different anomaly field values exist at the different sensors. Such an instrument is called a gradiometer (although a true gradient is measured only if the sensor spacing is much less than the sensor-to-object distance). Alignment of sensors is very critical as Fig. 2.10 shows.

If 3 vector magnetometers are situated close together and oriented to measure 3 orthogonal components of the field, they can be used as a total field magnetometer. One advantage of this method is that the

baseline field b_{0j} may be subtracted from each jth component by extrapolating from an anomaly free region and thus $\left\|\vec{b}\right\|$ may be measured instead of $\left\|\vec{b_0}+\vec{b}\right\|$. Generally, the 3 sensors are made orthogonal only to $\sim 0.01^{\circ}$ and software compensation is applied to effectively improve the alignment.

Baseline drift due to temporal fluctuations of the earth's field may be eliminated by the use of a "baseline" or reference magnetometer. Simultaneous field readings are obtained both for the reference magnetometer and another which is used to measure the field near an anomaly. If the reference magnetometer is situated far from any anomalies, its field reading may be subtracted from the reading of the second magnetometer. Spatial uniformity of the geomagnetic field (Section 2.2) ensures that geomagnetic fluctuations will be eliminated from the second magnetometer signal by such a method. Baseline elimination using total field magnetometers is slightly trickier if very high precision is required due to the nonlinear nature of Equation 2.

High accuracy magnetic measurements must be performed in a low magnetic noise environment. There are 4 ways of achieving such an environment.

1. **Low metallic content laboratories:** These are situated in remote locations (at least 40 km from high-voltage power lines and a few km from other buildings). There is very little metal present and none of it is ferrous. All power lines are shielded. In such locations, field gradients as low as 0.1 nT/m are obtainable. The schematic for a low metallic content laboratory is shown in Figures 2.11 and 2.12.

2. **Magnetic shields:** These usually consist of layers of high permeability material with insulating gaps between them. Gap spacing and material thickness are chosen to optimize field attenuation. A properly designed shield can reduce the interior field by as much as 10^{-6} over the external field. Whole rooms as well as small cylindrical volumes can be shielded in this manner.

3. **Active compensation:** A field free region may be obtained by measuring three orthogonal components of the external field using a magnetometer and applying an electrical current to a set of 3 Helmholtz coils with mutually orthogonal axes to produce a field opposite to the external field.

4. **Gradiometer or double gradiometer measurement:** If it is desired to measure the very weak field of a source in close proximity to the sensor, one can measure the derivative or second derivative of the field using a gradiometer or double gradiometer respectively. Biomagnetic measurements, such as measuring the field of the heart or magnetite in lungs, are typical applications of this technique. Roughly speaking, the field of a dipolar source falls off as r^{-3}, r being the source-to-sensor distance. The derivative and second derivative fall off as r^{-4} and r^{-5} respectively and thus unless a source is close to the detector, its measured gradient or double gradient will be quite small. For example, if a source at 1 cm from a sensor is moved to 10 m, its measured field is reduced by 10^{-9}, its gradient by 10^{-12} and its double gradient by 10^{-15}. Biomagnetic sources have been measured using double gradiometers in unshielded, uncompensated rooms immediately above subway stations.

2.7 Rotational Properties of Magnetostatic Measured Quantities

2.7.1 Rotationally Invariant Measurements

The most commonly measured quantities derived from the magnetostatic field vector, $\vec{B}$, are the three components, B_i, the magnitude of the field, B, the gradient tensor, $\mathbf{G}$ and the double gradient tensor, $\mathbf{\Gamma}$. The i,j component of the gradient tensor is

$$G_{ij} = \frac{\partial B_i}{\partial X_j} \tag{5}$$

where a cartesian system with position given by

$$\vec{X}^T = (X_1, X_2, X_3) \tag{6}$$

is assumed (superscript T denotes the transpose). Likewise the double gradient is defined by

$$\Gamma_{ijk} = \frac{\partial G_{ij}}{\partial X_k} \tag{7}$$

Because measurement platforms are seldom stable, it is very important to know how these quantities behave under a rotation of the coordinate system.

If a rotation from an unprimed to a primed coordinate system is defined by an (orthogonal) rotation matrix, $\mathbf{A}$, whose elements are the direction cosines for the transformation, then the vector $\vec{B}$ transforms according to [9]

$$\vec{B}' = \mathbf{A}\vec{B} \tag{8}$$

$\mathbf{G}$ is a second rank tensor and transforms according to

$$\mathbf{G}' = \mathbf{AGA}^T = \mathbf{AGA}^{-1} \tag{9}$$

We wish to determine what quantities exist that are invariant under a rotation. Clearly the magnitude B, being a scalar, is invariant. Invariant quantities associated with the gradient tensor become apparent when we attempt to find its eigenvalues and eigenvectors. To do this one must set $\det(\mathbf{G} - \lambda\mathbf{I}) = 0$, where λ is an eigenvalue and $\mathbf{I}$ is the 3×3 unit matrix. It is easy to show that $\det(\mathbf{G} - \lambda\mathbf{I})$ is an invariant quantity for any λ and thus

$$\det(\mathbf{G}' - \lambda\mathbf{I}) = \det(\mathbf{G} - \lambda\mathbf{I}) \tag{10}$$

Direct evaluation leads to

$$\det(\mathbf{G} - \lambda\mathbf{I}) = D + \lambda Q + \lambda^2 T - \lambda^3 \tag{11}$$

where

$$\begin{aligned} D = &(G_{11}G_{22}G_{33} + G_{12}G_{23}G_{31} + G_{13}G_{21}G_{32}) \\ &- (G_{11}G_{23}G_{32} + G_{12}G_{21}G_{33} + G_{13}G_{31}G_{22}) \end{aligned} \tag{12}$$

$$Q = -\frac{1}{2}\mathrm{Tr}\left(\mathbf{G}^T\mathbf{G}\right) =$$

$$(G_{12}G_{21} + G_{13}G_{31} + G_{23}G_{32}) - (G_{11}G_{22} + G_{11}G_{33} + G_{22}G_{33}) \tag{13}$$

$$T = G_{11} + G_{22} + G_{33} \tag{14}$$

Inspection reveals that D is the determinant, Q is the negative sum of principal axis cofactors and T is the trace of $\mathbf{G}$.

By substituting Equation 11 in 10 we get

$$\lambda^0(D - D') + \lambda^1(Q - Q') + \lambda^2(T - T') = 0 \tag{15}$$

and since λ is an arbitrary constant we have

$$D = D' \tag{16}$$

$$Q = Q'$$

$$T = T'$$

From Maxwell's equations we have

$$\nabla \cdot \vec{B} = 0 \tag{17}$$

But $\mathrm{Trace}(\mathbf{G}) = \nabla \cdot \vec{B}$ and hence

$$T = 0 \tag{18}$$

Furthermore, if the region is source free, then Maxwell's equations also state

$$\nabla \times \vec{B} = 0 \tag{19}$$

which implies that

$$G_{ij} = G_{ji} \quad i \neq j \tag{20}$$

The field gradient tensor is thus symmetric and is specified by only 5 independent elements (any two of the diagonal elements and either the upper or lower off-diagonal elements). The invariant forms D and Q can be reduced to

$$D = (G_{22} + G_{33})\left(G_{23}^2 - G_{22}G_{33}\right) + 2G_{12}G_{13}G_{23} - \left(G_{12}^2 G_{33} + G_{13}^2 G_{22}\right) \tag{21}$$

$$Q = G_{12}^2 + G_{13}^2 + G_{23}^2 + G_{22}^2 + G_{33}^2 + G_{22}G_{33} \tag{22}$$

In order to investigate the properties of D and Q we choose a rotation that diagonalizes $\mathbf{G}$. This is called a "principal axis transformation" and the coordinate system axes are called the "principal axes". We denote this coordinate system by a double prime ($''$).

$$\mathbf{G}'' = G_{33}'' \begin{pmatrix} \frac{1}{2}(\eta - 1) & 0 & 0 \\ 0 & -\frac{1}{2}(\eta + 1) & 0 \\ 0 & 0 & 1 \end{pmatrix} \tag{23}$$

where the asymmetry factor η is given by

$$\eta = \frac{G_{22}''^2 - G_{11}''^2}{G_{33}''^2} \tag{24}$$

and G_{11}'', G_{22}'', G_{33}'' are the principal axis components of the gradient tensor. Without loss of generality we choose

$$|G_{33}''| \geq |G_{22}''| \geq |G_{11}''| \tag{25}$$

and thus

$$0 \leq \eta \leq 1 \tag{26}$$

Substitution of Equations 23 and 24 into 21 and 22 yields

$$D = \frac{1}{4}\left(1 - \eta^2\right) G_{33}''^3 \tag{27}$$

$$Q = \frac{1}{4}\left(3 + \eta^2\right) G_{33}''^2 \tag{28}$$

Equations 26,27,28 yields

$$0 \leq D \leq \frac{1}{4} G_{33}''^3 \tag{29}$$

$$\frac{3}{4} G_{33}''^2 \leq Q \leq G_{33}''^2 \tag{30}$$

Although there would appear to be only 2 independent quantities needed to construct $\mathbf{G}''$ in this system, there are indeed 5, since 3 Euler angles are necessary to specify the rotation relative to a known space-fixed system (usually the detector system). More specifically, the transformation matrix $\mathbf{A}''$ between the principal axis and space-fixed system is formed by

$$\mathbf{A}'' = (\hat{e_1}\ \hat{e_2}\ \hat{e_3}) \tag{31}$$

where $\hat{e_1}, \hat{e_2}, \hat{e_3}$ are the normalized eigenvectors of $\mathbf{G}$.

Both D and Q require all 5 independent components of $\mathbf{G}$ and both are rotationally invariant. Q, having only quadratic as opposed to cubic terms, should lend itself to easier analysis when attempting to determine the source characteristics from the field. Q can more closely approximate the largest principal axis component of $\mathbf{G}$ because $Q^{1/2}$ has a smaller range of values than $D^{1/3}$, for a given value of G_{33}''.[7] All these points suggest that Q should be preferred to D when attempting to analyse gradient data. This indeed turns out to be the case when the properties of D and Q are compared for the specific case of a static magnetic dipole source.

[7] Note that $0 \leq D^{\frac{1}{3}} \leq 0.63 G_{33}''$ and $0.866 G_{33}'' \leq Q^{\frac{1}{2}} \leq G_{33}''$.

2.7.2 Rotationally Invariant Measurements of a Dipole Source

Now lets examine the magnetic field of a static magnetic dipole. In practice, the magnetic fields associated with ferrous bodies frequently behave as though they were due to a static magnetic dipole situated at the geometric center of the body. Our aim is to try to relate the invariant measurable field quantities to the source characteristics (position, dipole moment) so that the latter can be deduced from a series of field or gradient measurements. We employ two coordinate systems; a space-fixed one denote by capital letters and a system fixed to the dipole, denoted by small letters, which we call the "body-fixed" system. The dipole is located at position $\vec{X_0}^T = (X_{01}, X_{02}, X_{03})$ in the space-fixed system and at $(0,0,0)$ in the body-fixed system. The well known expression for the dipole field $\vec{b}$ at position $\vec{r}^T = (x_1, x_2, x_3)$ in the body-fixed system due to a static dipole moment $\vec{m}^T = (m_1, m_2, m_3)$ is given by

$$\vec{b} = \frac{\mu_0}{4\pi} r^{-3} \left(-\vec{m} + \frac{3}{r^2} \left[\vec{r}^T \vec{m} \right] \vec{r} \right) \tag{32}$$

where $\mu_0 = 4\pi \times 10^{-7}$ H/m is the permeability of free space and

$$r^2 = \vec{r}^T \vec{r}$$

In the body-fixed system, the jk element of the field gradient tensor is given by

$$g_{jk} = \frac{\partial b_j}{\partial x_k}$$

Substitution of Equation 32 in the above equation yields

$$g_{jk} = \frac{3\mu_0}{4\pi} r^{-5} \left(x_j m_k + x_k m_j + \left[\delta_{jk} - \frac{5 x_j x_k}{r^2} \right] \left[\sum_{i=1}^{3} x_i m_i \right] \right) \tag{33}$$

where δ_{jk} is the Kronecker delta, or in tensor notation,

$$\mathbf{g} = \frac{3\mu_0}{4\pi} r^{-5} \left(\vec{r}\vec{m}^T + \vec{m}\vec{r}^T + \left[\vec{r}^T \vec{m} \right] \left[\mathbf{I} - 5 r^{-2} \vec{r}\vec{r}^T \right] \right) \tag{34}$$

Note that Equation 33 has built into it the fact that the gradient tensor is symmetric and traceless.

The space-fixed and body-fixed coordinate systems are connected by a rotation matrix, $\mathbf{A}$, such that

$$\vec{m} = \mathbf{A}\vec{M} \tag{35}$$

The same transformation applies to all other vectors as well. One can also define $\vec{B}$ and $\mathbf{G}$ in the space-fixed system.

$$\vec{B} = \frac{\mu_0}{4\pi} R^{-3} \left(-\vec{M} + \frac{3}{R^2} \left[\vec{R}^T \vec{M} \right] \vec{R} \right) \tag{36}$$

$$G_{jk} = \frac{3\mu_0}{4\pi} R^{-5} \left(R_j M_k + R_k M_j + \left[\delta_{jk} - \frac{5 R_j R_k}{R^2} \right] \left[\sum_{i=1}^{3} R_i M_i \right] \right) \tag{37}$$

where $\vec{R}^T = \left(\vec{X} - \vec{X_0} \right)^T$ and $R^2 = \vec{R}^T \vec{R}$. [8]

Now we wish to evaluate some rotationally invariant measurable quantities. The square of the field can in principle be obtained from a 3-axis total field magnetometer.

$$b^2 = \vec{b}^T \vec{b} = \left(\frac{\mu_0}{4\pi} \right)^2 r^{-6} \left(\vec{m}^T \vec{m} + 3 \left[\vec{m}^T \vec{r} \right]^2 r^{-2} \right) \tag{38}$$

To evaluate D and Q it is easiest to choose a body-fixed frame in which $m_1 = m_2 = 0$ and $m_3 = m$. D and Q are then evaluated using Equations 21, 22 and 33. The result is expressed in an explicitly invariant form.

$$D = -\left(\frac{3\mu_0}{4\pi} \right)^3 r^{-15} \left(\vec{m}^T \vec{r} \right) \left(\left[\vec{m}^T \vec{r} \right]^2 + \left[\vec{m}^T \vec{m} \right] \left[\vec{r}^T \vec{r} \right] \right) \tag{39}$$

[8] Can you use the equations for $\vec{b}$, $\vec{B}$, $\mathbf{g}$ and $\mathbf{G}$ to show that $\vec{b} = \mathbf{A}\vec{B}$ and $\mathbf{g} = \mathbf{AGA}^T$?

$$Q = \left(\frac{3\mu_0}{4\pi}\right)^2 r^{-10}\left(2\left[\vec{m}^T\vec{r}\right]^2 + \left[\vec{m}^T\vec{m}\right]\left[\vec{r}^T\vec{r}\right]\right) \tag{40}$$

Now assume a coordinate system in which $m_2 = 0$ and in which the x_3 axis is parallel with the X_3 axis. Further assume that the x_2 axis makes an angle α with the X_2 axis (Fig. 2.13). Field measurements are made in the $x_3 = z$ plane orthogonal to the x_3 axis. This is a geometry common to many magnetic source detection problems such as the detection of buried artillery shells and mines, submarines, etc. The measurement plane in most cases would be horizontal and the x_3 axis would be vertical. The rotation matrix becomes

$$\mathbf{A} = \begin{pmatrix} \cos\alpha & \sin\alpha & 0 \\ -\sin\alpha & \cos\alpha & 0 \\ 0 & 0 & 1 \end{pmatrix} \tag{41}$$

As an example of the analysis of an invariant quantity we will examine Q. A number of properties of Q in the measurement plane can be examined, such as zeros, full width at half maximum (FWHM), maxima, minima, etc. We first study the position and value of the extrema. Extrema of Q in the measurement plane occur for

$$\frac{\partial Q}{\partial x_j} = 0 \quad \text{for} \quad j = 1,2 \quad \text{simultaneously} \tag{42}$$

In the present coordinate system Q (Equation 40) can be rewritten

$$Q = a_0 \frac{\left(a_1 x_1^2 + a_2 x_2^2 + a_3 x_3^3 + a_4 x_1 x_3\right)}{\left(x_1^2 + x_2^2 + x_3^2\right)^5} \tag{43}$$

where

$$a_0 = \left(\frac{3\mu_0}{4\pi}\right)^2 \;;\; a_1 = 3m_1^2 + m_3^2$$

$$a_2 = m_1^2 + m_3^2 \;;\; a_3 = m_1^2 + 3m_3^2 \;;\; a_4 = 4m_1 m_3 \tag{44}$$

Substitution of Equation 43 into 42 and extensive manipulation shows that extrema with respect to x_1, x_2 occur in the $x_3 = z$ plane for

$$x_{1max} = \frac{z}{3m_1^2 + m_3^2}\left[\left(\frac{m_1 m_3}{8} f_1 + f_2\right)^{1/3} + \left(\frac{m_1 m_3}{8} f_1 - f_2\right)^{1/3} - \frac{3}{2} m_1 m_3\right] \tag{45}$$

$$x_{2max} = 0 \tag{46}$$

where

$$f_1 = 27m_1^4 + 51m_1^2 m_3^2 + 23m_3^4 \tag{47}$$

$$f_2 = \left[c_0 m_1^{12} + c_1 m_1^{10} m_3^2 + c_2 m_1^8 m_3^4 + c_3 m_1^6 m_3^6 + c_4 m_1^4 m_3^8 + c_5 m_1^2 m_3^{10} + c_6 m_3^{12}\right]^{1/2} \tag{48}$$

and

$$c_0 = \frac{1}{8} \;;\; c_1 = \left(\frac{1836}{1728} + \frac{729}{64}\right) \;;\; c_2 = \left(\frac{2754}{64} + \frac{6714}{1728}\right)$$

$$c_3 = \left(\frac{3843}{64} + \frac{13481}{1728}\right) \;;\; c_4 = \left(\frac{2346}{64} + \frac{15666}{1728}\right)$$

$$c_5 = \left(\frac{529}{64} + \frac{9996}{1728}\right) \;;\; c_6 = \frac{2744}{1728} \tag{49}$$

Substitution of x_{1max}, x_{2max} into the equation for Q (43) yields a maximum value of Q of

$$Q_{max} = z^{-8} a_0 \left(a_3 + \frac{a_5}{a_1}\left[a_4 + a_5\right]\right)\left(1 + \left[\frac{a_5}{a_1}\right]^2\right)^5 \tag{50}$$

where a_5 is the quantity in [ ] brackets in Equation 45. The subscript "*max*" has been used above to denote extrema points since it can be straightforwardly shown that $Q > 0$.

Inspection of Equation 45 reveals that there is only a single maximum and that its position is on the axis defined by the projection of the horizontal component of the dipole moment, displaced from the origin by an amount that is a fraction of z (Fig.2.14). The fraction is a function of m_1/m_3 and varies from 0 at $m_1 = 0$ to a maximum $\approx 0.15z$ at $m_1 \approx 2.5m_3$ and back to 0 at $m_3 = 0$. Thus the maximum is directly above the dipole to within $< 15\%$. This is illustrated in Figs. 2.15-2.17 where maps of the value of Q in a plane 1m above a dipole ($z = 1$m plane) are shown. The Figures correspond to different dipole orientations. Fig. 2.15 corresponds to a dipole with $m_1 = 0$, $m_3 = 1\text{A}\cdot\text{m}^2$; Fig. 2.16 to a dipole with $m_1 = 1$, $m_3 = 0\text{A}\cdot\text{m}^2$ and Fig. 2.17 to a dipole with $m_1 = 2$, $m_3 = 1\text{A}\cdot\text{m}^2$. For comparison, Figs.2.18-2.20 respectively show the maps of b_3 for the same dipole orientations and geometry. Note that the map for Q is appreciably more narrow than that for b_3, i.e, the field strength is concentrated nearer to the position directly over the dipole. Furthermore, note that there is a single maximum for Q which is almost directly over the dipole whereas there are maxima and minima for b_3 which can be far removed from the position in the plane immediately above the dipole. It appears that using Q to localize the position of the dipole in the measurement plane would require much less signal processing than b_3, provided moderate accuracy is required.

To determine other pertinent quantities such as the moment components and the depth is not so simple. Since the extremum solution provides 3 independent pieces of information (why?), at least three more are required to solve for the 3 position components and 3 moment components of the dipole. Additional useful information could include the FWHM or FWQM (full width at quarter maximum). The position for the half maximum points is found by substituting $Q_{max}/2$ (Equation 50) in Equation 43 and solving. Unfortunately solutions must be obtained using a root extractor algorithm to obtain values of x_1, x_2. The solution possesses radial symmetry about $\vec{x} = (0,0,0)$ only when $m_1 = 0$.[9] For other dipole orientations the locus of the half maximum is not circular but something like a distorted ellipse which is *not* centered about $x_1 = x_2 = 0$ in the plane (Fig.2.21). The ratio of major and minor axes[10] (a/b) of the locus is a function of m_1/m_3 (Fig.2.22) and can be used to determine the latter ratio. The length of the axes are a function of z and can be used to estimate the depth by employing a calibration curve similar to Fig.2.22. Knowing m_1/m_3 and z allows us to determine a more accurate estimate of the position of $x_1 = 0$ from Fig.2.14. Lastly, the magnitude of $\vec{m}$ can be obtained by substituting the measured value of Q_{max}, the estimated values of m_1/m_3, z, x_{1max}, and using $x_{2max} = 0$ in Equation 43.

A similar analysis may also be applied to the determinant D of the gradient tensor.

An analysis has been applied to the 3-axis component of $\vec{b}$ and has led to a successful nonrecursive algorithm for estimating the position and dipole moment of a static magnetic dipole to within a few percent [31]. The method is much less complicated than the above method for analysing Q, since the only measured quantities required are the field values and positions of the maximum and minimum in the measurement plane. An added advantage is that b_3 will be much larger than the field differences required to measure the gradient and so a less sensitive sensor is required. It should be pointed out that although b_3 is not in itself a rotationally invariant quantity, in low to mid-latitudes it is reasonably approximated by $(b_t - b_0)$ and hence can be measured by a total field magnetometer whose readings are insensitive to sensor orientation.

A comparison of some of the properties of Q and b_3 in the measurement plane is provided in Table 2.3.

There are also nonrecursive tracking algorithms based on gradient measurements. These require an eight element sensor array to measure the five independent components of the gradient plus at least one field component [29].

2.8 The Magnetic Field of Permeable Objects

The problem in magnetostatic quasi-remote sensing is to determine the nature of a magnetically permeable object from its anomaly field. In order to be able to do this, it is first necessary to understand how to

[9] For this special case, the locus of points whose values are half the maximum is circular with a radius $\approx 0.40094z$.

[10] The locus is not an ellipse but we can still define the "major axis" to be the symmetry axis and the "minor axis" to be the axis of largest length orthogonal to the major axis in the plane.

calculate the field, given the magnetic characteristics of the source. A complete discussion is beyond the scope of these lectures, although good accounts are found in [5], [8].

In magnetostatics, the basic assumption is that there is no time rate of change of charge density ρ anywhere in space. Thus the equation of continuity giving the current density $\vec{J}$ becomes,

$$\nabla \cdot \vec{J} = 0 \tag{51}$$

In addition,

$$\nabla \times \vec{H} = \vec{J} \tag{52}$$

We always have

$$\nabla \cdot \vec{B} = 0 \tag{53}$$

A solution of Equations 52 and 53 that satisifies the boundary conditions is guaranteed to be unique. Suppose we have 2 regions; region 1 with $\vec{B_1}$, $\vec{H_1}$ and permeability μ_1 and region 2 with $\vec{B_2}$, $\vec{H_2}$, μ_2. Let $\hat{n}$ be the unit vector directed from region 1 to 2 on the surface connecting the two regions. If $\vec{K}$ is the idealized surface current density, then the boundary condition equations are

$$\vec{B_1} \cdot \hat{n} = \vec{B_2} \cdot \hat{n} \tag{54}$$

$$\hat{n} \times \left(\vec{H_2} - \vec{H_1}\right) = \vec{K} \tag{55}$$

There are several methods of solving boundary-value problems in magnetostatics. They are broadly classed as follows:

1. **Generally applicable method - vector potential:** One can always express $\vec{B}$ in terms of a vector potential.

   $$\vec{B} = \nabla \times \vec{A} \tag{56}$$

   We need a constitutive relationship

   $$\vec{B} = \vec{B}\left(\vec{H}\right) \tag{57}$$

   but unless it is a very simple one, the problem is intractable. The most common choice is,

   $$\vec{B} = \mu \vec{H} \tag{58}$$

   Substitution in Equation 52 and choosing the Coulomb gauge $\left(\nabla \cdot \vec{A} = 0\right)$ gives

   $$\nabla^2 \vec{A} = \mu \vec{J} \tag{59}$$

   This can then be solved subject to the boundary conditions.

2. **Method for $\vec{J} = 0$ - scalar potential:** In this case

   $$\vec{H} = -\nabla \phi_m \tag{60}$$

   where ϕ_m is the scalar potential. Again we need a constitutive relationship and the problem is intractable unless Equation 57 is simple. If Equation 58 is valid then

   $$\nabla^2 \phi_m = 0 \tag{61}$$

   and we then apply boundary conditions.

3. **Hard ferromagnets:** In this case $\vec{M}$ is given and $\vec{J} = 0$. It can be shown that

   $$\phi_m\left(\vec{x}\right) = -\frac{1}{4\pi}\int_{V'} \frac{\nabla' \cdot \vec{M}\left(\vec{x'}\right)}{\left|\vec{x} - \vec{x'}\right|} d^3x' + \frac{1}{4\pi}\oint_{S'} \frac{\vec{M}\left(\vec{x'}\right)}{\left|\vec{x} - \vec{x'}\right|} \cdot d\vec{s'} \tag{62}$$

where the field coordinates are unprimed and the source coordinates are primed. It is assumed that $\vec{M}$ is finite within a volume V' bounded by surface S'. [11]

Alternatively, if we choose to use the vector potential $\vec{A}$, we have[12]

$$\vec{A}(\vec{x}) = \frac{1}{4\pi}\int_{V'} \frac{\nabla' \times \vec{M}\left(\vec{x'}\right)}{\left|\vec{x} - \vec{x'}\right|} d^3x' + \frac{1}{4\pi}\oint_{S'} \frac{\vec{M}\left(\vec{x'}\right)}{\left|\vec{x} - \vec{x'}\right|} \times d\vec{s'} \tag{63}$$

Note that for all three methods the problem becomes extremely complicated unless:

1. a simple $\vec{B}\left(\vec{H}\right)$ relationship exists or
2. a simple distribution of $\vec{M}$ exists and
3. the geometry is very simple.

Only a few special cases have analytic closed form solutions. Among these are the uniformly magnetized sphere, the homogeneous ellipsoid (which includes the sphere as a special case) in a uniform external field and the infinite length homogeneous cylinder in a uniform external field.

Before we study a specific boundary value problem, a few words should be said about demagnetization, a phenomenon which is commmon to virtually all magnetostatic problems. Simply put, the induced magnetization of a permeable body is not given by the product of the external magnetic field and the volume susceptibility, but is reduced by a factor. It is simple to show how this arises.

Suppose a body with volume susceptibility χ is placed in a magnetic field of intensity $\vec{H}_0$. Inside the body there will be a magnetic field $\vec{H}_1$ while outside there will be a field $\vec{H} = \vec{H}_0 + \vec{H}_s$ where $\vec{H}_s$ is the secondary field due to the magnetization $\vec{M}$ of the body. When one solves the boundary value problem, one often finds a relationship of the form

$$\vec{H}_1 = \vec{H}_0 - d\vec{M} \tag{64}$$

where d is a scalar. However,

$$\vec{M} = \chi \vec{H}_1 \tag{65}$$

so that

$$\vec{H}_1 = \vec{H}_0/(1 + d\chi) \tag{66}$$

Thus the apparent susceptibility, that is, the quantity which when multiplied by the external field gives the magnetization is

$$\chi_a = \frac{\chi}{1 + d\chi} \tag{67}$$

The term $d\chi$ represents the reduction of the field inside the body due to its magnetization.

The factor d is called the "demagnetization factor" and ranges from 0 for needle-like objects magnetized along their long axes to 1 for a flate plate magnetized transversely. As an example, a uniformly magnetized sphere has $d = 1/3$. Thus demagnetization reduces the magnetic moment of a body by the ratio $1/(1 + d\chi)$ $(0 \leq d \leq 1)$ and is a function of the orientation of the body with respect to the ambient magnetic field. Obviously, if χ is small, demagnetization is negligable. This is typically so for diamagnetic and paramagnetic materials. Demagnetization may be of considerable importance for ferromagnetic and ferrimagnetic materials.

With these general considerations in mind, we turn our attention to the homogeneous spheroid in a uniform external magnetic field. Although this has been solved exactly [8], we shall approach the problem differently by performing a multipole expansion analysis. This will allow us to demonstrate the nature of the various significant multipole components of the field. In addition, the method is applicable to objects whose shapes are more complex and which do not have closed form solutions.[13]

[11] Note that $-\nabla' \cdot \vec{M} = \rho_m$ where ρ_m is the effective magnetic volume charge density and $\vec{M} \cdot \hat{n}' = \sigma_m$ where $\hat{n}$ is the unit vector parallel to the surface element $d\vec{s}'$ and σ_m is the effective magnetic surface charge density.

[12] $\vec{M} \times \hat{n}'$ is the effective magnetic surface current.

[13] The field inside a susceptible volume is only uniform if the interior properties are homogeneous and isotropic and the boundary surface is second order, such as is the case for an ellipsoid. It is convenient when analysing commonly encountered shapes such as sheets and prisms to assume a uniform internal field. The assumption will fail near the volume boundary but is usually a reasonable approximation through the body as a whole.

2.9 Example of Magnetic Modelling - Multipole Expansion Method

Assume a uniformly permeable spheroid in a uniform parallel magnetostatic field.[14] Assume a cartesian coordinate system defined by orthogonal unit vectors $\left(\hat{x}_1', \hat{x}_2', \hat{x}_3'\right)$ with origin at the geometric center of the spheroid. The symmetry axis is the $\hat{x}_3'$ axis (Fig.2.23). It can be shown (see [8],p.257) that the induced field inside the spheroid is also uniform and parallel. Inside the spheroid we have

$$\vec{M}_1' = \mu_0^{-1}\vec{B}_1 - \vec{H}_1 \tag{68}$$

where $\vec{M}'$ is the magnetization, $\vec{B}$ is the magnetic flux density, $\vec{H}$ is the magnetic field and the subscript "1" denotes interior quantities. If the spheroid is uniform and isotropic with relative permeability μ_r, then

$$\begin{aligned}\vec{B}_1 &= \mu_r\mu_0\vec{H}_1 \\ \vec{M}_1' &= (\mu_r - 1)\vec{H}_1\end{aligned} \tag{69}$$

Thus $\vec{M}_1'$ is uniform and parallel too. In the following, we drop the subscript "1" from $\vec{M}_1'$ since we will be referring to magnetization explicitly only inside the spheroid. Now the scalar potential of a source with magnetization $\vec{M}'$ is given by[6] [15]

$$\phi_m(r) = \frac{1}{4\pi}\int_{V'} \vec{M}'\cdot\nabla'\left(\frac{1}{r''}\right)dv' \tag{70}$$

By expansion of the gradient we have,

$$\phi_m(r) = \frac{1}{4\pi}\left(\int_{S'}\frac{1}{r''}\vec{M}'\cdot d\vec{s}' - \int_{V'}\frac{1}{r''}\nabla'\cdot\vec{M}'dv'\right) \tag{71}$$

But $\nabla'\cdot\vec{M}' = 0$ so

$$\phi_m(r) = \frac{1}{4\pi}\int_{S'}\frac{1}{r''}\vec{M}'\cdot d\vec{s}' \tag{72}$$

Now we carry out a standard multipole expansion about the origin.[16]

$$\begin{aligned}\phi_m(r) = \frac{1}{4\pi}\left[\frac{1}{r''}\right]_{r''=r}\int_{S'}\vec{M}'\cdot d\vec{s}' + \frac{1}{4\pi}\left[\frac{\partial}{\partial x_\alpha'}\left(\frac{1}{r''}\right)\right]_{r''=r}\int_{S'}x_\alpha'\vec{M}'\cdot d\vec{s}' + \\ \frac{1}{4\pi}\left[\frac{\partial^2}{\partial x_\alpha'\partial x_\beta'}\left(\frac{1}{r''}\right)\right]_{r''=r}\frac{1}{2!}\int_{S'}x_\alpha'x_\beta'\vec{M}'\cdot d\vec{s}' + \\ \frac{1}{4\pi}\left[\frac{\partial^3}{\partial x_\alpha'\partial x_\beta'\partial x_\gamma'}\left(\frac{1}{r''}\right)\right]_{r''=r}\frac{1}{3!}\int_{S'}x_\alpha'x_\beta'x_\gamma'\vec{M}'\cdot d\vec{s}' + \cdots\end{aligned} \tag{73}$$

Recall that the scalar potential of a 2^n-pole with 2^n-pole moment $m^{(n)}_{\alpha\beta\ldots}$ is given by [6]

$$\phi^{(2^n)} = \frac{m^{(n)}_{\alpha\beta\ldots}}{4\pi n!}\frac{\partial^n}{\partial x_\alpha'\partial x_\beta'\ldots}\left(\frac{1}{r''}\right) \tag{74}$$

Thus comparing Equations 73 and 74 the first four moments of the source distribution are, in component notation,

$$m^{(0)} = \int_{S'}\vec{M}'\cdot d\vec{s}'$$

[14] It is assumed that the ellipsoid has no permanent magnetization.

[15] Prime supercript denotes source coordinates, unprimed denotes field coordinates, double prime denote mixed. Source volume is V' and bounding surface is S'. It is implied that $\vec{r}$ is not inside the body. Why?

[16] Summation convention is used in Equations 73 and 74, i.e, when indices are repeated in the same term, summation over these indices is implied. For example, $m_{\alpha\beta\beta} = \sum_\beta m_{\alpha\beta\beta}$.

$$m_\alpha^{(1)} = \int_{S'} x'_\alpha \vec{M}' \cdot d\vec{s}'$$

$$m_{\alpha\beta}^{(2)} = \int_{S'} x'_\alpha x'_\beta \vec{M}' \cdot d\vec{s}'$$

$$m_{\alpha\beta\gamma}^{(3)} = \int_{S'} x'_\alpha x'_\beta x'_\gamma \vec{M}' \cdot d\vec{s}' \tag{75}$$

where $m^{(0)}$ is the scalar monopole moment, $m_\alpha^{(1)}$ is the vector dipole moment, $m_{\alpha\beta}^{(2)}$ is the quadrupole moment (a rank 2 tensor) and $m_{\alpha\beta\gamma}^{(3)}$ is the octupole moment (a rank 3 tensor).

As an example of how the integrals are evaluated, we calculate $m^{(0)}$.

$$m^{(0)} = \int_{S'} \vec{M}' \cdot d\vec{s}' =$$

$$\int_{S'} M'_1 \hat{x}'_1 \cdot d\vec{s}' + \int_{S'} M'_2 \hat{x}'_2 \cdot d\vec{s}' + \int_{S'} M'_3 \hat{x}'_3 \cdot d\vec{s}' =$$

$$M'_1 \int_{S'} \hat{x}'_1 \cdot d\vec{s}' + M'_2 \int_{S'} \hat{x}'_2 \cdot d\vec{s}' + M'_3 \int_{S'} \hat{x}'_3 \cdot d\vec{s}' =$$

$$M'_1 \int_{V'} \left(\nabla' \cdot \hat{x}'_1\right) dv' + M'_2 \int_{V'} \left(\nabla' \cdot \hat{x}'_2\right) dv' + M'_3 \int_{V'} \left(\nabla' \cdot \hat{x}'_3\right) dv' = 0 \tag{76}$$

The second last line follows from the uniformity of $\vec{M}'$ and the last line follows from the divergence theorem.[17]

In a manner analogous to Equation 76, we can show that the α component of the magnetic dipole moment $\vec{m}^{(1)}$ is[18] [19]

$$m_\alpha^{(1)} = M'_\alpha V' \qquad \alpha = 1, 2, 3 \tag{77}$$

Similarly, the quadrupole moment tensor $\mathbf{m^{(2)}}$ can be shown to be identically zero. This *does* require the assumption of uniform parallel $\vec{M}'$ as well as the assumptions of symmetry about the $\hat{x}'_3$ axis and mirror symmetry about the plane defined by $x'_3 = 0$ (fore-aft symmetry). Thus

$$m_{\alpha\beta}^{(2)} = 0 \tag{78}$$

The assumptions leading to the last equation also imply that all even order moments are identically zero, i.e, for n an integer,

$$\mathbf{m^{(2n)}} = 0 \tag{79}$$

The next higher order contribution to ϕ_m is due to the octupole moment tensor $\mathbf{m^{(3)}}$. The method to calculate the moment components is tedious but similar to the method used to calculate the previous three moments. Although there are 27 possible elements for $m_{\alpha\beta\gamma}^{(3)}$, examination of Equation 75 reveals that there are only 10 independent elements. The assumption of $\hat{x}_3$-axis symmetry further reduces the number of independent nonzero elements to 6. These are:

$$m_{111}^{(3)} = 3m_{221}^{(3)} = 3M'_1 I_{11}$$

$$m_{222}^{(3)} = 3m_{112}^{(3)} = 3M'_2 I_{11}$$

$$m_{333}^{(3)} = 3M'_3 I_{33}$$

$$m_{113}^{(3)} = m_{223}^{(3)} = M'_3 I_{11}$$

[17] We have proved this for the case of constant $\vec{M}'$ but it is true for any $\vec{M}'$. Can you prove it?

[18] This equation is true even if $\vec{M}'$ is not constant throughout the body.

[19] $m_\alpha^{(1)}$ is independent of the choice of origin in the expansion of Equation 72 but this is not true for higher order moments. See [5] p.139.

$$m^{(3)}_{331} = M'_1 I_{33}$$
$$m^{(3)}_{332} = M'_2 I_{33} \tag{80}$$

where

$$I_{11} = \frac{1}{2}\int_{V'} \left(r'^2 - x'^2_3\right) dv' \tag{81}$$

$$I_{33} = \int_{V'} x'^2_3 dv' \tag{82}$$

$$m^{(3)}_{\alpha\alpha\beta} = m^{(3)}_{\alpha\beta\alpha} = m^{(3)}_{\beta\alpha\alpha} \tag{83}$$

and

$$m^{(3)}_{\alpha\beta\gamma} = 0 \quad \text{if} \quad \alpha \neq \beta \neq \gamma \tag{84}$$

So far the analysis has applied to any axially symmetric body with fore-aft symmetry. Now assume that the body is a spheroid and that the diameter of the spheroid along the symmetry axis is $2ae$ and the diameter of the largest axis orthogonal to the symmetry axis is $2a$. It is simple to show that

$$V' = \frac{4}{3}\pi e a^3$$

$$I_{11} = \frac{4\pi}{15} e a^5$$

$$I_{33} = \frac{4\pi}{15} e^3 a^5 \tag{85}$$

We still need to know the value of M'_1, M'_2, M'_3. Assume that the external magnetic field (usually the earth's) in the absence of the spheroid is $\vec{b_0}^T = (b_{01}, b_{02}, b_{03})$. A solution of the boundary value problem ([8],p.207), assuming the permeability of the spheroid is $\mu_{r1}\mu_0$ and that of the surrounding medium is $\mu_{r2}\mu_0$, yields

$$M'_j = \mu_0^{-1} F_j b_{0j} \quad j = 1, 2, 3 \tag{86}$$

$$F_j = (\mu_{r1} - 1) / (1 + A_j [\mu_{r1} - \mu_{r2}] / [2\mu_{r2}]) \tag{87}$$

where

$$A_j = a^3 e \int_0^\infty \left(s + a_j^2\right)^{-1} \left(s + a^2\right)^{-1} \left(s + a^2 e^2\right)^{-1/2} ds \quad j = 1, 2, 3 \tag{88}$$

with $a_1 = a_2 = a$ and $a_3 = ae$. Integration of the previous equation and simplification yields

$$A_1 = A_2 = e\left(e + E\right)\left(e^2 - 1\right)^{-1} \tag{89}$$

$$A_3 = -2e\left(e^{-1} + E\right)\left(e^2 - 1\right)^{-1} \tag{90}$$

where

$$E = \ln\left(e - \left[e^2 - 1\right]^{\frac{1}{2}}\right)\left(e^2 - 1\right)^{-\frac{1}{2}} \tag{91}$$

for $e > 1$ (prolate spheroid),

$$E = \left(\arctan\left[e\left\{1 - e^2\right\}^{-\frac{1}{2}}\right] - \pi/2\right)\left(1 - e^2\right)^{-\frac{1}{2}} \tag{92}$$

for $e < 1$ (oblate spheroid), or

$$A_1 = A_2 = A_3 = \frac{2}{3} \tag{93}$$

for $e = 1$ (sphere).

Note that each function F_j is just the demagnetization factor for the boundary value problem corresponding to an ambient magnetic field $b_{0j}\hat{x}'_j$. The functions F_j are graphed in Figs.2.24-2.26.

We now wish to calculate the magnetostatic field at point $\vec{r}$ from the origin, due to the field induced in the spheroid. We assume that the measurement point is in free space. If we keep terms up to and including the octupole term Equations 73 and 74 imply

$$\phi_m \approx \phi^{(2)} + \phi^{(8)} \tag{94}$$

or in terms of the magnetic field,

$$\mu_0^{-1}\vec{b} = -\nabla\phi_m \approx -\nabla\phi^{(2)} - \nabla\phi^{(8)}$$

$$\approx \mu_0^{-1}\left(\vec{b^{(2)}} + \vec{b^{(8)}}\right) \tag{95}$$

Following extensive manipulation of Equations 73,94,95, we have in component notation using summation convention,

$$b_\alpha^{(2)} = \frac{\mu_0}{4\pi} r^{-3}\left(-m_\alpha^{(1)} + 3r^{-2}\left[x_\beta m_\beta^{(1)}\right] x_\alpha\right) \tag{96}$$

and

$$b_\alpha^{(8)} = \frac{\mu_0}{8\pi} r^{-5}\left(3m_{\alpha\beta\beta}^{(3)} - 15r^{-2}\left[x_\alpha x_\beta m_{\beta\gamma\gamma}^{(3)} + x_\beta x_\gamma m_{\alpha\beta\gamma}^{(3)}\right] + 35r^{-4}x_\alpha x_\beta x_\gamma x_\delta m_{\beta\gamma\delta}^{(3)}\right) \tag{97}$$

All field quantities have been derived in a body-fixed coordinate system which the observer does not *a priori* know. We now introduce a space-fixed coordinate system with arbitrary origin, whose vectors are indicated by upper case letters. This is the system to which measurements are referenced. It is assumed that the spheroid center is located at $\vec{R_0}^T = (X_{01}, X_{02}, X_{03})$.

The body-fixed and space-fixed coordinate systems are connected by a set of Euler angles (ϕ, θ, ψ). The angle θ is the angle between the spheroid symmetry axis and the vertical and ϕ is the angle between the projection of the symmetry axis on the horizontal plane and the space-fixed 1-axis. Because of the axial symmetry of the spheroid, we can choose $\psi = 0$. The Euler rotation tensor [9] is then given by[20]

$$\mathbf{A} = \begin{pmatrix} \cos\theta\cos\phi & \cos\theta\sin\phi & -\sin\theta \\ -\sin\phi & \cos\phi & 0 \\ \sin\theta\cos\phi & \sin\theta\sin\phi & \cos\theta \end{pmatrix}. \tag{98}$$

The body-fixed and space-fixed vectors are related by

$$\vec{b_0} = \mathbf{A}\vec{B_0}$$

$$\vec{m^{(1)}} = \mathbf{A}\vec{M^{(1)}}$$

$$\vec{b} = \mathbf{A}\vec{B}$$

$$\vec{b^{(2)}} = \mathbf{A}\vec{B^{(2)}}$$

$$\vec{b^{(8)}} = \mathbf{A}\vec{B^{(8)}} \tag{99}$$

where

$$\vec{B_0}^T = (B_{01}, B_{02}, B_{03}) =$$

$$(B_0\sin\theta_0\cos\phi_0, B_0\sin\theta_0\sin\phi_0, B_0\cos\theta_0) \tag{100}$$

where θ_0 is the polar angle and ϕ_0 is the azimuthal angle of $\vec{B_0}$ in the space-fixed cartesian system.

Examination of Equations 77 through 98 will reveal that given the size and shape of the spheroid (a, e), the magnetic material properties of the spheroid and the surrounding medium (μ_{r1}, μ_{r2}), the location of the geometric center of the spheroid (X_{01}, X_{02}, X_{03}) and the orientation of the spheroid's symmetry axis with respect to the space fixed system (θ, ϕ), we can calculate the magnetic field $\left(\vec{B}\right)$ due to the presence of the spheroid that a sensor would measure at a point in space.

An example of the success of such a model is illustrated in Figs. 2.27 and 2.28. The first Figure shows the measured signature (solid line) and theoretical prediction (dotted) for a 0.08m radius mild steel sphere

[20] Note that $\mathbf{A}^T\mathbf{A} = \mathbf{I}$ where $\mathbf{I}$ is the 3×3 identity tensor.

whose center lies directly under the sensor path at closest approach.[21] The depth[22] was measured to be 0.73m. Deviation of the model from theory has been shown to be due to remnant magnetization.[23] The second Figure shows the measured signature of a 105mm howitzer shell (solid line) and the theoretical signature of a spheroid of similar size and shape (dotted line) to illustrate that the model is applicable to realistic situations involving axially symmetric objects too. Depth was measured as 0.96m, the shell symmetry axis was tilted 47° from vertical and its projection in the horizontal plane was 43° from magnetic north. Spheroid parameters of $a = 0.06$m and $e = 3.5$ gave the best fit to the data. Measured values for the shell were estimated to be $a \approx 0.05$m, $e \approx 3.5$.[24] Remarkably, even though the model is only an approximation, the good agreement was maintained as the shell was rotated and placed at different depths without having to change the model parameters. The slight difference between the two curves of Fig.2.28 is likely due deviations of the shell shape from that of the model as well as remnant magnetization.

This brings up a very important point about magnetostatic modelling. Remnant magnetization can be very difficult to model since its strength and direction are often unknown for an individual object. Generally it is ignored and this turns out to be satisfactory for many applications in which the object has not had a "colourful" magnetic history. This assumption is not generally true for geomagnetic applications. In some cases, such as the measurement of magnetite in miner's lungs, the material can be subjected to a known large magnetic field prior to measurement, thus assuring that remnant magnetization dominates induced magnetization. The orientation of a particle with respect to the premagnetizing field must be known if the anomaly field of the particle is to be modelled successfully.[25]

Although analytical models such as the multipole expansion method provide insight into how the fields behave, they are of limited use in many practical situations involving permeable objects. This is particularly so when one has to account for hysteresis curves of B versus H in a material, the effects of remnant magnetization or object boundaries that cannot be expressed simply. In such cases numerical solutions of the field equations are necessary. One may solve either differential or integral equations, depending on the problem at hand, by numerical techniques such as finite difference and finite element and a number of standard methods are in widespread use. Discussion of such numerical techniques are beyond the scope of these lectures, but [19] is a good reference article.

2.10 Inverse Magnetostatic Problems

2.10.1 Introduction

The actual problem with which we are faced in magnetostatic remote sensing is the inverse of that in the last section. The problem may be posed as follows: "Given a set of magnetic field or field gradient measurements referenced to a space-fixed system, determine the position, size, shape and material properties of the object." Problems in which field measurements are used to infer properties of the source of the field are called "inverse problems".

To study the properties of an inverse problem, we shall use the the uniform spheroid as an example. We assume that the accuracy of measurements is such that moments of higher order than octupole may be neglected. Note that the problem is greatly simplified compared to the case of a body of arbitrary shape. For the spheroid there are 9 unknown parameters; 2 size/shape parameters (a, e), 2 magnetic material properties (μ_{r1}, μ_{r2}), 2 angles which determine the orientation of the symmetry axis (θ, ϕ), and the 3 position coordinates of the spheroid center (X_{01}, X_{02}, X_{03}). For a body of arbitrary shape, there are 22 independent parameters; 3 components of $\vec{m}^{(1)}$, 6 independent components of $\mathbf{m}^{(2)}$, 10 independent components of $\mathbf{m}^{(3)}$ and the 3 position components of the center of the object.[26] Nevertheless, even the

[21] Sensor travelled S to N in straight line in the horizontal plane. Experimental set up is shown in Fig.2.11.

[22] Distance between center of the sensor's active volume and the geometric center of the object at the point of closest approach of the sensor.

[23] How would you go about showing this?

[24] We also have $\mu_{r1} = 100$, $\mu_{r2} = 1$, $\theta_0 = 17^{\circ}$, $\phi_0 = 180^{\circ}$. The steel portion of the artillery shell is by no means a spheroid. It is axially symmetric but it is hollow and has an angular shape, somewhat like a cross between a truncated spheroid and a cylinder. The estimates of a and e for the shell are thus only approximate quantities based on measuring the overall length and width of the shell.

[25] Typically the particles are modelled as spheres or randomly oriented spheroids.

[26] Where is the information concerning the size,shape, magnetic properties and orientation of the body contained?

uniform spheroid inverse problem turns out to be quite difficult to solve.

In practical situations, the spheroid problem can be further simplified. For ambient field values typical of those on the earth's surface, we usually have $300 \leq \mu_{r1} \leq 1000$. Typical rocks have values of μ_{r2} between 1.0 and 1.1.[27] For this range of μ_{r1} and μ_{r2}, Figs.2.24-2.26 reveal that the F_j functions which determine the components of the magnetization of the spheroid are insensitive to μ_{r1} and μ_{r2}. Thus μ_{r1} may be fixed at say, 500 and $\mu_{r2} = 1$ without much error. There are now only 7 unknown parameters;$a, e, \theta, \phi, X_{01}, X_{02}, X_{03}$.

It is immediately obvious that information is necessary from multipoles of order higher than dipole if the problem is to be solved uniquely. The space- fixed components of $\vec{B^{(2)}}$ are a function of 6 parameters; the three components of $\vec{X_0}$ and the three components of $\vec{M^{(1)}}$. Thus there is a built in degeneracy that keeps us from uniquely determining the 7 spheroid parameters from $\vec{B^{(2)}}$.[28] Note that for the special case of a sphere, there are only four parameters and dipole field information is sufficient to solve the problem. Indeed it can be shown that the homogeneous sphere in a uniform external magnetic field has a pure dipole anomaly field. This means that if only dipole field measurements are available, we cannot distinguish between a compact orientable body of arbitrary shape and a sphere. We will later see that in spite of this apparent deficiency, dipole measurements can still be used to identify spheroids.

There are two general techniques that may be used to estimate the spheroid parameters from measurements of $\vec{B}$. The two are "model fitting" and "pattern recognition". Although our problem is quite specialized, these methods are generally applicable to all magnetostatic inverse problems.[29]

2.10.2 Solution by Model Fitting

Model fitting involves devising a mathematical model to describe the secondary magnetic field as a function of source parameters and then performing maximum likelihood estimation (MLE) to determine the parameter values that best fit the measurements. Most geometries do not have simple analytical models and are thus not ideally suited to this method. It is possible to use a numerical model in the MLE procedure in place of an analytic field equation, but this makes the method very computationally intensive.

For the spheroid, we do have an analytical equation. Unfortunately, in this case as in most, the field equation is nonlinear in the source parameters which means that a nonlinear estimation technique must be used. Such techniques are recursive and usually require substantial computer time if there are many data points and/or parameters. Also, the initial values of the parameters must be guessed and a technique which is insensitive to the initial guesses is necessary. If the uncertainties in the data are Gaussianly distributed, least squares fitting is an MLE method and a particularly good algorithm to use is Marquardt's method [30]. The technique is reasonably fast and produces accurate estimates of parameters if the model is correct[30] Its main strengths are that its performance (i.e, speed, accuracy of estimates, etc.) is very insensitive to the initial parameter guesses and it is reasonably robust. All fitting methods tend to be more prone to oscillations, instabilities, and nonconvergence as the number of parameters increases. This may be partly corrected by increasing the number of data points but this only helps if the points are "well distributed" and then only up to a certain number (typically $\sim$ a few hundred). Also, the more data points that are employed, the longer the time required for convergence of the algorithm. In spite of all these pitfalls, spheroid parameters have been successfully estimated using the "dipole+octupole" model. For typical laboratory measurements (position errors $\sim$ 0.01m, field errors $\sim$ 1.0nT), parameters have been estimated to an accuracy of a few percent [30]. Unfortunately, convergence problems and the formation of false solution sets due to local minima in χ^2 space also occur occasionally and must be circumvented by heuristic checks in the computer code.

[27] Magnetite is an exception with $2 \leq \mu_{r2} \leq 14$ approximately.

[28] $\vec{B^{(2)}}$ can be measured by measuring $\vec{B}$ at distances far enough from the object so that $\vec{B^{(3)}} \approx 0$ but near enough so that $\vec{B}$ can still be measured with sufficient accuracy.

[29] Specific examples may be found in [4].

[30] There are other algorithms that are faster and more accurate but not both together. These attributes tend to oppose one another so that Marquardt's algorithm is a good compromise.

2.10.3 Solution by Pattern Recognition

Pattern recognition involves comparing characteristics of a set of magnetic data from an unknown object with that from a known object to determine if the two objects are the same. A full discussion of pattern recognition is beyond the scope of these lectures, but a number of good introductory texts are available. An excerpt from one of them (Tou and Gonzalez [13]) is included with the notes to provide some introductory terminology. Geophysics routinely makes use of "characteristic curves" to determine whether the source of a magnetic anomaly is a dyke, plate, dipole doublet or some other simple body. The chief problem is that generally magnetic profiles[31] for a single object change with the choice of sensor path and object depth and orientation. Thus huge amounts of data must must be stored even if the number of possible objects is small. Clearly some form of data reduction or compression (called "feature extraction") is essential to make pattern recognition feasible for magnetic identification. One plan is to oversample each profile, then perform a Fast Fourier Transform and discard higher frequency information to form the feature vector for the profile [32]. For certain geometries, heuristic extrapolation or interpolation techniques[33] can be employed to minimize the number of different depths at which profiles must be obtained. In spite of these and other methods of data compression, profile matching methods usually involve huge libraries of characteristic curves or feature vectors.

2.10.4 Pattern Recognition for Compact Axially Symmetric Objects

In a number of realistic situations the sensor-to-object distance is sufficiently large that multipole fields of order higher than a dipole may be neglected. As previously mentioned, this means that an orientable compact object of arbitrary shape cannot be uniquely identified by measurements of the field. In practice, however, the number of possible object shapes and sizes for a particular problem is usually finite and small. Uniqueness will then be ensured if the fields associated with only those objects are uniquely different. Under these conditions, location and identity of a compact object can be reliably determined using an algorithm that is fast and requires only a small amount of storage for the feature vectors of an object. We will present the method for an axially symmetric object using a spheroid as an example. The method can be generalized to an arbitrary compact body but it is a tedious and not particularly illuminating exercise.

The first step is to determine the location and dipole moment components of the object relative to a space-fixed coordinate system. This may be done by any one of a number of published algorithms using field [30], [31] or gradient [29] information or by a method such as that outlined for Q in Section 2.7.2. In performing the measurements, care must be taken to ensure that the sensor is far enough from the object that higher order multipole fields are negligable.

The space-fixed components of the dipole moment induced in a homogeneous permeable axially symmetric compact object by a uniform magnetostatic external field will vary with the orientation of the object. Since two angles define the orientation, the locus of all possible dipole moments for such an object is actually a two dimensional surface in a three dimensional space. This can readily be seen for the spheroid problem of Section 2.9. Using Equations 77 and 86, the magnetic moment induced in the spheroid due the ambient magnetic field can be rewritten

$$\vec{m} = \mu_0^{-1} V \mathbf{F} \vec{b_0} \tag{101}$$

where

$$\mathbf{F} = \begin{pmatrix} F_1 & 0 & 0 \\ 0 & F_1 & 0 \\ 0 & 0 & F_3 \end{pmatrix} \tag{102}$$

and $V \equiv V'$. By substituting Equations 98 and 99 in 101 and following extensive simplification, we find that the space-fixed magnetic dipole moment vector can be expressed explicitly in terms of only space-fixed quantities:

[31] A profile is a set of field measurements taken along a one dimensional curve, usually a straight line, in a plane above the object.

[32] This relies on the fact that for most magnetostatic problems, the profiles are slowly varying spatial functions.

[33] usually based on scaling the spatial extent of the profile as a function of depth

$$\vec{M} \equiv \vec{M^{(1)}} = \begin{pmatrix} M_1 \\ M_2 \\ M_3 \end{pmatrix} =$$

$$\mu_0^{-1} V \begin{pmatrix} \{F_1 + [F_3 - F_1]\sin^2\theta\cos^2\phi\}B_{01} + \{[F_3 - F_1]\cos\theta\sin\theta\cos\phi\}B_{03} \\ \{[F_3 - F_1]\sin^2\theta\cos\phi\sin\phi\}B_{01} + \{[F_3 - F_1]\cos\theta\sin\theta\sin\phi\}B_{03} \\ \{[F_3 - F_1]\cos\theta\sin\theta\cos\phi\}B_{01} + \{F_1 + [F_3 - F_1]\cos^2\theta\}B_{03} \end{pmatrix}. \quad (103)$$

Examination of Equation 103 reveals that for a given ambient magnetic field and surrounding medium, $\vec{M}$ is a function of the spheroid shape, size and material (a, e, μ_{r1}) and two continuous orientation parameters (θ, ϕ). Also, because of symmetry, unique values of $\vec{M}$ occur only for $\theta = \phi = 0$, $0 < \theta < \pi/2$ when $0 \leq \phi < 2\pi$ and $\theta = \pi/2$ when $0 \leq \phi < \pi$. Two magnetic dipole moment surfaces corresponding to two spheroids of different shape and size are shown in Fig.2.29.

Our plan is to use the dipole moment vector as the feature vector to classify the object. Because the feature vectors form a surface or manifold in the feature space ($\vec{M}$ space) we must find a classifier that can determine to what surface a test vector belongs. The plan is to find a 2-D analogue to the Nearest Mean Vector classifier, which determines the distance from a test vector to a point.

A number of restrictions and assumptions will be imposed, but these are all applicable to the problem at hand. We will consider a prototype which is a manifold of M dimensions and a function of M independent parameters. The feature space is of dimension $N > M$. It is assumed that the manifold is well-behaved, ie., has no singularities or discontinuities on the portions under consideration. The manifold is assumed to be finite in extent, but may be open or closed. It is assumed that a given set of values of the M independent parameters maps into no more than one point on the manifold. However, one point may correspond to several values of a particular independent parameter. (The manifold is said to be "degenerate" in that parameter at that point). It is convenient to use Dirac bra-ket notation applied to real vectors. Thus, the row vector $(x_1, x_2 ..., x_n)$ is written as $\langle x|$. The column vector with the same elements is denoted by $|x\rangle$ and the scalar product of $\langle x|$ and $|y\rangle$ is written $\langle x|\, y\rangle$.

We will specifically be considering a pattern class whose prototype consists of an $M = 2$ dimensional manifold in an $N = 3$ dimensional feature space. The prototype is a function of two continuous parameters, θ and ϕ. This is illustrated in Figure 2.30.

The prototype for class i and given θ, ϕ is a point defined by the head of a vector denoted $|m_i(\theta, \phi)\rangle$. The prototype is approximated by a finite number of "unit cells". For an $M = 2$ dimensional manifold, the unit cells are truncated hyperplanes, or hypertriangles (triangles for $N = 3$ as in Figure 2.30), which connect sampled points $|m_{i,j,k}\rangle$ on the hyperplane. The subscripts j, k indicate that the prototype feature vector is evaluated at discrete values of the parameters $\theta = \theta_j$ and $\phi = \phi_k$. Where on the manifold to choose the $|m_{i,j,k}\rangle$ in order to optimally approximate the manifold is dependent on its structure and will not be addressed further. Consider the region of the manifold for which $\theta_j \leq \theta \leq \theta_{j+1}$ and $\phi_k \leq \phi \leq \phi_{k+1}$. This region of the manifold may be approximated by two hypertriangles. One hypertriangle passes through $|m_{i,j,k}\rangle$, $|m_{i,j+1,k}\rangle$, $|m_{i,j,k+1}\rangle$ and is bounded by

$$|u_{i,j,k}\rangle = |m_{i,j,k+1}\rangle - |m_{i,j,k}\rangle$$

$$|v_{i,j,k}\rangle = |m_{i,j+1,k}\rangle - |m_{i,j,k}\rangle \quad (104)$$

and $|u_{i,j,k}\rangle - |v_{i,j,k}\rangle$.
The other hypertriangle passes through $|m_{i,j+1,k}\rangle$, $|m_{i,j+1,k+1}\rangle$, $|m_{i,j,k+1}\rangle$ and is bounded by

$$|u'_{i,j,k}\rangle = |m_{i,j+1,k}\rangle - |m_{i,j+1,k+1}\rangle$$

$$|v'_{i,j,k}\rangle = |m_{i,j,k+1}\rangle - |m_{i,j+1,k+1}\rangle \quad (105)$$

and $|v'_{i,j,k}\rangle - |u'_{i,j,k}\rangle$.

By allowing j, k to span the values corresponding to the upper and lower limits of θ_j and ϕ_k respectively, the entire prototype manifold for class i may be approximated. In what follows the subscripts i, j, k will be dropped where it is unambiguous to do so.

To find the distance to the hypertriangle bounded by the vectors $|u\rangle, |v\rangle$, $|u\rangle - |v\rangle$ we first form an orthonormal basis. The orthonormal basis $|\alpha\rangle, |\beta\rangle$ is constructed using the Gram-Schmidt method [15]. It is assumed that $|u\rangle$ and $|v\rangle$ are not colinear. The basis vectors are

$$|\alpha\rangle = |u\rangle \,/\, \langle u|\, u\rangle^{\frac{1}{2}} \tag{106}$$

$$|\beta\rangle = \left(|v\rangle - \frac{\langle u|\, v\rangle}{\langle u|\, u\rangle}\,|u\rangle\right) / \left(\langle v\,|v\rangle - \frac{\langle u|\, v\rangle^2}{\langle u|\, u\rangle}\right)^{\frac{1}{2}}. \tag{107}$$

Let $|x\rangle$ be a test vector and define

$$|y_{i,j,k}\rangle = |x\rangle - |m_{i,j,k}\rangle\,. \tag{108}$$

If we further define $\left|y^{(s)}_{i,j,k}\right\rangle$ to be the projection of $|y_{i,j,k}\rangle$ onto the subspace spanned by the basis and $|d_{i,j,k}\rangle$ to be the vector which is normal to the subspace and which passes through $|x\rangle$, then

$$|d\rangle = |y\rangle - \left|y^{(s)}\right\rangle \tag{109}$$

and

$$\left|y^{(s)}\right\rangle = \langle y|\, \alpha\rangle\,|\alpha\rangle + \langle y|\, \beta\rangle\,|\beta\rangle =$$

$$\frac{\langle y|\, u\rangle}{\langle u|\, u\rangle}\,|u\rangle + \frac{\left(\langle y|\, v\rangle - \langle y|\, u\rangle\,\langle u|\, v\rangle\,/\,\langle u|\, u\rangle\right)}{\left(\langle v|\, v\rangle - \langle u|\, v\rangle^2\,/\,\langle u|\, u\rangle\right)}\left(|v\rangle - \frac{\langle u|\, v\rangle}{\langle u|\, u\rangle}\,|u\rangle\right). \tag{110}$$

After substantial simplification, we find

$$\left|y^{(s)}\right\rangle = p\,|u\rangle + q\,|v\rangle \tag{111}$$

where

$$q = \frac{\langle y|\, v\rangle\,\langle u|\, u\rangle - \langle y|\, u\rangle\,\langle u|\, v\rangle}{\langle v|\, v\rangle\,\langle u|\, u\rangle - \langle u|\, v\rangle^2} \tag{112}$$

and

$$p = \frac{\langle y|\, u\rangle - q\,\langle u|\, v\rangle}{\langle u|\, u\rangle}. \tag{113}$$

Note that the denominator in Equation 112 is zero iff. $|u\rangle$ and $|v\rangle$ are colinear.

If $|x\rangle$ is a sample from the class i corresponding to the region of the prototype manifold bounded by $|u\rangle, |v\rangle, |u\rangle - |v\rangle$, then estimates, $\hat{\theta}$ and $\hat{\phi}$, of the continuous parameters associated with $|x\rangle$ may be obtained from

$$\hat{\theta} = \theta_j + q_{i,j,k}\,(\theta_{j+1} - \theta_j) \tag{114}$$

$$\hat{\phi} = \phi_k + p_{i,j,k}\,(\phi_{k+1} - \phi_k)\,. \tag{115}$$

The minimum distance, $d_{i,j,k}$, from the test vector to the hypertriangle is approximated by

$$d_{i,j,k} = \langle d_{i,j,k}|\, d_{i,j,k}\rangle^{\frac{1}{2}}\,. \tag{116}$$

The previous equations calculate the minimum distance to the infinite hyperplane passing through the hypertriangle. The region of the manifold under consideration has been assumed to be approximated by the hyperplane only within the boundaries of the unit cell (hypertriangle). Thus, the previous distance equations are only valid if $|y^{(s)}\rangle$ lies within the boundaries of the hypertriangle. It can be easily shown that this is true provided $p \geq 0$, $q \geq 0$ and $0 \leq p+q \leq 1$. If any of these conditions are not satisfied, then $d_{i,j,k}$ is replaced by the minimum distance from the test point to the vectors which bound the hypertriangle, using the method described above for approximating the minimum distance to a one dimensional manifold. For speed of implementation, q is calculated first and based on its value, the appropriate calculation of $d_{i,j,k}$ is carried out.

By changing all quantities to primed quantities, Equations 106 to 116 may also be used to find the minimum distance to the hypertriangle bounded by the vectors $|u'\rangle, |v'\rangle, |v'\rangle - |u'\rangle$ provided Equations 108, 114 and 115 are changed to

$$|y_{i,j,k}\rangle = |x\rangle - |m_{i,j+1,k+1}\rangle \tag{117}$$

$$\hat{\theta} = \theta_{j+1} + q'_{i,j,k}\,(\theta_j - \theta_{j+1}) \tag{118}$$

$$\hat{\phi} = \phi_{k+1} + p'_{i,j,k}\,(\phi_k - \phi_{k+1})\,. \tag{119}$$

The minimum distance, d_i, from the test vector to the manifold is then approximated by

$$d_i = \min_{j,k} \left\{ d_{i,j,k}, d'_{i,j,k} \right\}. \tag{120}$$

The test vector is assigned to the class i for which d_i is a minimum.

The prototype manifold for certain values of one of the continuous parameters, say θ_l, may be independent of the other continuous parameter. In this case, the manifold between θ_l, θ_{l+1}, ϕ_k and ϕ_{k+1} may be approximated by a single primed hypertriangle instead of both a primed and an unprimed hypertriangle.

As an example of the abilities of the classification method, noise-free magnetic moments of six different spheroids (Table 2.4) were generated at 15° increments of the orientation angles θ, ϕ to produce a design set. Test sets, consisting of magnetic moment feature vectors generated at 5° increments were generated with different % noise levels added to them. Table 2.5 shows the probability of misclassification for the classifier just described (Continuous Parameter Classifier). The continuous parameter classifier theory and comparison with other classifiers is discussed more fully in [32].

3 Electrostatic Methods

3.1 Introduction

Of all the electromagnetic properties, the conductivity (σ) has the widest range of variation. Whereas under normal conditions the magnetic permeability (μ) varies from $\sim \mu_0$ to $1000\mu_0$ and the permittivity (ϵ) varies from $\sim \epsilon_0$ to $80\epsilon_0$, σ can span 20 or so decades (see Fig.3.1, Table 3.1).

Two effects complicate the electrostatic process in addition to simple ohmic conduction. First, potentials can develop in the medium. These are caused by

1. a difference in chemical potentials of minerals at the interface between two minerals or
2. gradients in solute concentrations in interstitial water or
3. fluid motion in porous materials.

These are steady state effects which are generally referred to as "spontaneous polarization". Second, charge may accumulate at the interface between certain minerals due to the flow of current from an external source. This is called "induced polarization". The difference between the two is that the former may involve current flow in the absence of external voltage.

The "d.c. resistivity" or "electrical impedance" method is the simplest electromagnetic measurement method there is, at least in principle. Electrodes are inserted in the body to be measured. A potential across them establishes a current field in the body and the finite conductivity of the body produces an electric potential which is measured at the body surface by two electrodes.

In geophysics, the body is the earth and the field is perturbed by the presence of subsurface zones of conductivity which differ from the otherwise presumed homogeneous conductivity of the volume. There are two types of exploration. Vertical exploration involves detecting layered structures and is generally done by making measurements as the electrode array gradually increases in horizontal spacing about a fixed point. Horizontal exploration is used to look for horizontal anomalies such as ore bodies and involves moving an array of electrodes of fixed spacing horizontally along the ground.

Electrical impedance methods are used in medicine to measure certain global or bulk cardiac parameters and intrathoracic fluid volumes and some attempts have been made at imaging soft tissue and bones. Such measurements are possible because of the large conductivity contrasts in the body.[34]

There are many types of exploration array systems and we shall only mention a few. For vertical exploration, the most popular is the Wenner array (Fig.3.2). The voltage for a given input current is measured and the array is expanded about the center so that deeper layers have more effect on the potentials. We shall return to this. For horizontal exploration, the current electrodes are often fixed at large distances and the potential contours are mapped, i.e.,(Fig.3.3)

There are some problems associated with taking resistivity measurements. One is contact potential, the potential between electrodes in the absence of source current. It is due to electrochemical emfs on electrode surfaces or material interfaces in the host body. One solution is to measure potentials with the current in first one direction and then another. This may be done using low frequency AC current and measuring only the AC component of the voltage, but the frequency must be low enough so that potentials induced by the magnetic field are negligable. Usually frequencies less than 1KHz are alright but they should be < 1Hz to ensure no induced polarization effects. Alternatively, one can use exotic electrodes such as Ag-AgCl to suppress contact potential.

Another problem, surprisingly, is the high sensitivity of the methods. Conductivities span a wide range and these directly affect the measured potentials. Thus a perfect conductor and one an order of magnitude greater than the "background" conductivity are virtually indistinguishable. This makes it very difficult to accurately measure conductivity values when high conductivity contrasts exist. Electromagnetic induction gets around this since the effect of including the magnetic interaction is to make the response nonlinear in σ.

3.2 A Note On Ohm's Law

Fundamental to d.c. resistivity methods is Ohm's Law:

$$\vec{J} = \sigma \vec{E} \tag{121}$$

where $\vec{J}$ is the current density, σ is the scalar conductivity and $\vec{E}$ is the electric field.

Note that Ohm's law is linear. This is fortunate since otherwise most problems would be intractable. It is an empirical relationship, however, and a number of materials do not obey the law for high current densities. For most experiments this is not a problem, since $|J| < 1\text{A/m}^2$ except near the electrodes. Still, one should be aware of the limitations of the approximation and approach each problem cautiously.

Equation 121 is actually the scalar form of Ohm's Law and is true only for an isotropic medium. In general, $\overline{\overline{\sigma}}$ is a rank-2 tensor and

$$\vec{J} = \overline{\overline{\sigma}} \vec{E} \tag{122}$$

To show that anisotropy can be significant, consider three simple dual conductivity models with conductivities $\sigma_1 \gg \sigma_2$ (Fig.3.4):

Model (a) is a set of orthogonal rods of conductivity, σ_1, imbedded in medium of conductivity, σ_2. In (b) the rods are replaced by parallel sheets and in (c) by random spheres. For all models the volume

[34] The contrasts are primarily due to differences in salinity between fluids internal to and surrounding organs.

fraction, p, of material 1 is much less than 2. These models simulate minerals of low conductivity with interstitial water or semi-metallic inclusions. The effective conductivities are found to be:

$$\text{(a)} \quad \sigma_x = \sigma_y = \sigma_z = \frac{p\sigma_1}{3} + (1-p)\sigma_2 \tag{123}$$

$$\text{(b)} \quad \sigma_x = \sigma_y = p\sigma_1 + (1-p)\sigma_2$$

$$\sigma_z = \sigma_1\sigma_2 / \left[p\sigma_2 + (1-p)\,\sigma_1\right] \tag{124}$$

$$\text{(c)} \quad \sigma_x = \sigma_y = \sigma_z \approx \left(\frac{2\sigma_2 + \sigma_1 + 2p\left[\sigma_1 - \sigma_2\right]}{2\sigma_2 + \sigma_1 - p\left[\sigma_1 - \sigma_2\right]}\right)\sigma_2 \tag{125}$$

To illustrate the variation, we compare the results of the three models in Table 3.2. It is assumed that the volume fraction $p = 0.2$ and $\sigma_1 = 10\sigma_2$ or $100\sigma_2$.

We note from this that even in isotropic media, measured conductivity is strongly dependent on geometry. Also, "platy" structures are highly aeolotropic (anisotropic). Aeolotropy is very difficult to analyse and generally we must make the isotropic assumption if a mathematical model is desired.

3.3 Rock Conductivity

Assuming that electrostatic measurements can be made and the inverse problem solved to determine the conductivities of the body being measured, one must attempt to determine the material's identity from its conductivity. When imaging the human body, for example, this may not be too difficult since bone has quite a different conductivity than muscle or fat. Much of remote sensing is related to geoexploration and the picture for rock/mineral conductivity is considerably more confusing.

All minerals, except the semi-metallics, are insulators with $10^{-17} < \sigma < 10^{-12}$ S/m. Impurities, such as electron donors/acceptors and other crystal defects, increase this by a few orders of magnitude. In the field, however, rock conductivities are $\sim 10^{-8}$ to 10^{-1} S/m (Table 3.1). This glaring discrepancy is accounted for by the fact that rock conductivities have little to do with mineral composition but rather are related to permeability/porosity of rock to fluids and the conductivity of the interstitial fluid. Much work has been done and many models have been developed to determine such properties from measured conductivities but it is beyond the scope of this course. There are, however, general trends of conductivities with rock type and these are presented graphically in Fig.3.5. Not shown in Fig.3.5 are the metallic minerals. These include free metals ($\sigma \sim 10^{+6}$–10^{+7}S/m) and sulfide ores ($\sigma \sim 10^{+2}$–10^{+4}S/m). Structural conductors, i.e., those with faults or fracture zones that capture large quantities of water are also excluded.

3.4 Theory

3.4.1 General

The basic idea of resistive measurements is to employ an array of electrodes connected to the body of interest in a (hopefully) appropriate geometry (Fig.3.6). The quantity of interest is $Z = V/I$ which is called the "transfer impedance". For d.c. or near d.c. frequencies, the quantity becomes $Z = R$, the "transfer resistance". We will see that for most geometries that can be simply analysed,

$$R = F\rho_a \tag{126}$$

where ρ_a is the "apparent resistivity" of the body and F is a geometry-dependant quantity which has units of inverse length. We wish to interpret the apparent resistivity in terms of the structure of the body being measured. This is **seldom** straightforward.

We will assume in the following discussions that the medium is isotropic and thus conductivity is a scalar quantity. Then Ohm's law is given by Equation 121. Furthermore, we assume that the electric field is conservative, which is equivalent to assuming that we are in the very low frequency regime. Thus

$$\nabla \times \vec{E} = 0 \tag{127}$$

$$\vec{E} = -\nabla\psi \tag{128}$$

where ψ is the scalar electric potential Except at current injection sites, the time rate of change of charge is zero and hence the equation of continuity becomes

$$\nabla \cdot \vec{J} = 0 \tag{129}$$

Substituting Equation 128 in 129 yields

$$\nabla \cdot (\sigma \nabla \psi) = 0 \tag{130}$$

which may be written

$$\nabla^2 \psi + \frac{1}{\sigma} (\nabla \psi) \cdot (\nabla \sigma) = 0 \tag{131}$$

The basic Equation 130 or 131 together with the appropriate boundary conditions uniquely specify the problem and guarantee a unique solution. Assume two regions, 1 and 2, and an interface surface between them whose unit normal at a point is $\hat{n}$. If the displacement variable along the normal direction is denoted n, then the boundary conditions are

$$\psi_1 = \psi_2 \quad \text{Dirichlet b.c.} \tag{132}$$

$$\sigma_1 \nabla \psi_1 = \sigma_2 \nabla \psi_2 \quad \text{Neumann b.c.} \tag{133}$$

Note however, [5] (pp.40-45), that a solution to the Poisson Equation 130 with ψ and $\partial\psi/\partial n$ specified *arbitrarily* on a *closed* boundary (the so-called Cauchy boundary conditions) does not exist! This is because only a single boundary condition (Neumann or Dirichlet) is necessary at each point of the bounding surface to define a unique solution to the Poisson equation. We shall use this as a method of solving the inverse problem later.

As with magnetostatics, a wide variety of models have been developed, although almost paradoxically there are only a handful of general geometries which yield closed form solutions. We shall solve a simple model as an example of the methods to use. Although the example is not a compact object geometry, it does illustrate typical solution methods. The object of the problem, once again, is to deduce underlying anomaly properties by resistance measurements on the surface of the body. The first step is to have the mathematical model and the second is to solve the inverse problem.

A case of importance in geophysics is one in which σ is a function only of z. Cylindrical coordinates (r, ϕ, z) are then a good choice due to azimuthal symmetry and 131 becomes

$$\frac{\partial^2 \psi}{\partial r^2} + \frac{1}{r}\frac{\partial \psi}{\partial r} + \frac{\partial^2 \psi}{\partial z^2} + \frac{1}{\sigma}\frac{\partial \psi}{\partial z}\frac{\partial \sigma}{\partial z} = 0 \tag{134}$$

This equation is solved by the standard method of separation of variables.

$$\psi(r, z) = \hat{R}(r) Z(z) \tag{135}$$

where

$$\frac{d^2 \hat{R}}{dr^2} + \frac{1}{r}\frac{d\hat{R}}{dr} + \lambda^2 \hat{R} = 0 \tag{136}$$

and

$$\frac{d^2 Z}{dz^2} + \frac{1}{\sigma}\frac{d\sigma}{dz}\frac{dZ}{dz} - \lambda^2 Z = 0 \tag{137}$$

with λ being, so far, an arbitrary separation constant. A general solution of Equation 134 can then be written

$$\psi(r, z) = \int_0^\infty F(\lambda) \hat{R}(\lambda, r) Z(\lambda, z) d\lambda \tag{138}$$

where λ is obviously positive definite and $F(\lambda)$ is chosen to fit the boundary conditions.

3.4.2 Example of Electrostatic Modelling

Consider now a two layer earth model in which the current is injected into the top layer at the origin of the coordinate system. The conductivity is constant in each layer (Fig.3.7). First let's examine the field in the vicinity of the current electrode. Assume the electrode to be a small hemisphere of radius b (Fig.3.8).[35] The radial current density is given by[36]

$$J_r = \frac{I}{2\pi R^2} \tag{139}$$

where a total current I is injected at the electrode and

$$R^2 = z^2 + r^2 \tag{140}$$

The corresponding radial electric field is

$$E_r = \rho_1 J_r \tag{141}$$

where

$$\rho_1 = \sigma_1^{-1} \tag{142}$$

near the electrode. Thus the primary potential (due to the current electrode) is

$$\psi^P = \frac{I\rho_1}{2\pi R} \tag{143}$$

From Bessel function theory (i.e. [10]),

$$\frac{1}{R} = \int_0^\infty J_0(\lambda r)\, e^{-\lambda z} d\lambda \quad \text{for} \quad z > 0 \tag{144}$$

J_0 is the Bessel function of the first type of order 0. Now, solutions of Equation 136 are either $J_0(\lambda r)$ or $Y_0(\lambda r)$, the latter being the Bessel function of the second type. But $Y_0(\lambda r)$ is singular at $r = 0$ and must be excluded. Solutions of Equation 137 for constant σ are of the form $\exp(\pm\lambda z)$. Thus, the resultant potential in the upper layer is

$$\begin{aligned} \psi_1 &= \psi^P + \psi_1^S \\ &= \psi^P + \int_0^\infty \left[\hat{A}(\lambda)e^{-\lambda z} + \hat{B}(\lambda)e^{+\lambda z}\right] J_0(\lambda r) d\lambda \end{aligned} \tag{145}$$

for $0 < z < h$. Equations 144 and 145 can be combined to yield

$$\psi_1 = \frac{I\rho_1}{2\pi} \int_0^\infty \left\{[1 + A(\lambda)]\, e^{-\lambda z} + B(\lambda)e^{+\lambda z}\right\} J_0(\lambda r) d\lambda \tag{146}$$

In the lower layer, since $z \to \infty$, the potential has the form

$$\psi_2 = \frac{I\rho_1}{2\pi} \int_0^\infty C(\lambda)e^{-\lambda z} J_0(\lambda r) d\lambda \tag{147}$$

To find the dimensionless constants A, B, C, we must apply boundary conditions. These are

$$\begin{aligned} \frac{\partial \psi_1^S}{\partial z} &= 0 \quad \text{at} \quad z = 0 \\ \psi_1 &= \psi_2 \quad \text{at} \quad z = h \\ \sigma_1 \frac{\partial \psi_1}{\partial z} &= \sigma_2 \frac{\partial \psi_2}{\partial z} \quad \text{at} \quad z = h \end{aligned} \tag{148}$$

[35] It is assumed implicitly that the second electrode is at infinity.

[36] Boundary conditions are imposed implicitly in this equation since the 2π factor ensures that all current must flow into the $z > 0$ region.

Applying these to Equations 146 and 147, we obtain

$$A - B = 0$$

$$(1 + A)\, e^{-\lambda h} + Be^{+\lambda h} = Ce^{-\lambda h}$$

$$\sigma_1 \left[(1 + A)\, e^{-\lambda h} - Be^{+\lambda h}\right] = \sigma_2 Ce^{-\lambda h} \tag{149}$$

These yield

$$A = B = e^{-2\lambda h} K / \left(1 - Ke^{-2\lambda h}\right) \tag{150}$$

where

$$K = (\rho_2 - \rho_1) / (\rho_2 + \rho_1) \tag{151}$$

Thus, the solution for the potential in the upper layer is Equation 146, with A, B given by Equations 150, 151. Most often, measurements of potential are made on the earth's surface ($z = 0$). Then

$$\psi(r, 0) = \frac{I\rho_1}{2\pi r} G(r, K) \tag{152}$$

where

$$G(r, K) = 1 + 2Kr \int_0^\infty \frac{e^{-2\lambda h}}{1 - Ke^{-2\lambda h}} J_0(\lambda r)\, d\lambda \tag{153}$$

The limiting cases are:

$$G(r, K) \to 1 \quad \text{as} \quad h/r \to \infty$$

$$G(r, K) \to \frac{\rho_2}{\rho_1} \quad \text{as} \quad h/r \to 0 \tag{154}$$

As an interesting (?) aside, by expanding the denominator of Equation 153 in a power series in $K \exp(-2\lambda h)$, it is easy to show that

$$G(r, K) = 1 + 2Kr \sum_{n=0}^{\infty} K^n I_n \tag{155}$$

where

$$I_n = \int_0^\infty e^{-\lambda(n+1)2h} J_0(\lambda r)\, d\lambda = \frac{1}{\left(r^2 + \{[n+1]\,2h\}^2\right)^{1/2}} \tag{156}$$

The secondary potential is thus seen as being due to an infinite series of image sources at positions $(0, 0, [n + 1]2h)$ and strength $2IK^{n+1}$.

3.4.3 Four Electrode Array

The one electrode configuration is not very practical and so we consider a more general geometry (Fig.3.9). Two current electrodes, a source of $+I$ amperes and a sink of $-I$ amperes are located on the $z = 0$ plane. The voltage difference between points P_1 and P_2, also on the $z = 0$ plane, is measured. Without loss of generality, we can place the source electrode at the origin and the sink on the x axis. By superposition, the potential ψ_1 at P_1 is

$$\psi(x_1, y_1) = \frac{I\rho_1}{2\pi} \left[\frac{G(r_{11}, K)}{r_{11}} - \frac{G(r_{21}, K)}{r_{21}}\right] \tag{157}$$

where

$$r_{11}^2 = x_1^2 + y_1^2$$

$$r_{21}^2 = (x_1 - x_0)^2 + y_1^2 \tag{158}$$

The potential at P_2 is similarly

$$\psi(x_2, y_2) = \frac{I\rho_1}{2\pi} \left[\frac{G(r_{12}, K)}{r_{12}} - \frac{G(r_{22}, K)}{r_{22}}\right] \tag{159}$$

where

$$r_{12}^2 = x_2^2 + y_2^2$$
$$r_{22}^2 = (x_2 - x_0)^2 + y_2^2 \tag{160}$$

The voltage between the electrodes, $V = \psi_1 - \psi_2$, is

$$V = \frac{I\rho_1}{2\pi}\left[\frac{G(r_{11},K)}{r_{11}} - \frac{G(r_{21},K)}{r_{21}} - \frac{G(r_{12},K)}{r_{12}} + \frac{G(r_{22},K)}{r_{22}}\right] \tag{161}$$

Now for homogeneous ground ($\rho_2 = \rho_1$ or $h \to \infty$), $G = 1$ at all positions. We define the "apparent resistivity", ρ_a, as that resistivity which, for a homogeneous earth, would yield the same voltage difference as for the inhomogeneous model. Clearly,

$$\frac{\rho_a}{\rho_1} = \frac{\frac{G(r_{11},K)}{r_{11}} - \frac{G(r_{21},K)}{r_{21}} - \frac{G(r_{12},K)}{r_{12}} + \frac{G(r_{22},K)}{r_{22}}}{\frac{1}{r_{11}} - \frac{1}{r_{21}} - \frac{1}{r_{12}} + \frac{1}{r_{22}}} \tag{162}$$

For the Wenner array (Fig. 3.2), $r_{11} = r_{22} = a$, and $r_{12} = r_{21} = 2a$, and

$$\frac{\rho_a}{\rho_1} = 2G(a,K) - G(2a,K) \tag{163}$$

This function is shown in Fig.3.10. We see that $\rho_a > \rho_1$ for $\rho_2 > \rho_1$ and $\rho_a < \rho_1$ for $\rho_2 < \rho_1$. Also, as the upper layer thickness becomes much greater than the electrode spacing, $\rho_a \to \rho_1$, as is expected.

3.5 The Inverse Problem

Curves of the type just shown are routinely used to provide a rough interpretation of resistivity data in electrical depth sounding applications, provided that the underlying structures are simple. Vertical models are available for the 3-layer case, 2-layers with horizontal/vertical anisotropy and $\rho \propto \exp(-\alpha z)$. Horizontal models are available for the vertical dyke and vertical wedge. Other models are available for the homogeneous spherical inclusion, several cylindrical geometry models, and spheroidal inclusions.

In geophysics, the inverse problem is usually solved merely by choosing the most appropriate geometric model and attempting to interpret the effective resistivity based on curves such as Fig.3.10. If the model is wrong, this fails badly and often there is no indication that it failed. Often, there is no appropriate model, although one may require insight from other remote sensing measurements to ascertain that the model is unsuitable.

Because of the limited choice of models, considerable work has gone into solving the inverse problem by numerical methods which can handle general geometries. Many of these are "impedance tomography" techniques, which assume that the current in the body of interest follows ray-like paths. This allows powerful, well-established techniques, such as back-projection, Radon transform, etc., which are used in conventional X-ray, gamma, PET or NMR tomography to be applied to the problem.[37] There are a number of problems with methods requiring the assumption of ray-like current paths. First, the methods require the measurement of voltages at active current electrodes. This necessarily introduces the effects of contact and spreading resistance which degrades the measurements. This is a major concern, since measurements have to be accurate to produce fine detail in the tomographic image. Second, the experimental techniques necessary to constrain the problem to the ray-like path assumption are complicated, usually involving complex guarded electrodes. Third, current paths are highly dependent on the object of interest, in particular its conductivity distribution, even when guard electrodes are used, and often the ray assumption is not justified. Since it is the conductivity distribution we seek, one cannot know *a priori* whether the ray assumption is appropriate. A more in-depth discussion of the problems associated with conventional tomographic techniques is found in [52]. In spite of all this, a number of researchers have had some success obtaining impedance tomography images. Henderson and Webster [47] have obtained isoadmittance contours of the chest using an array of guarded electrodes.[38] Other medical

[37] One does not necessarily have to assume straight-line paths for some of the more sophisticated tomography algorithms. For example, some researchers have assumed curved current flux tubes.

[38] The guarding was intended to force a long narrow measurement volume centered on each electrode.

applications and methods are discussed in [51], geophysical applications may be found in [48] and ground water pollution monitoring is discussed in [56].

An alternative approach is to inject current at one or more sites, measure the surface potential distribution and numerically solve the field equations. The inverse problem associated with a single excitation[39] does not generally have a unique solution. By this, we mean that different internal conductivity distributions can give rise to the same surface potential.[40] If a number of excitations are used and the potential distribution measured for each excitation, the indeterminancy can be reduced. Each excitation is akin to a different view in conventional tomography and hence it might seem intuitive that if a sufficient number of independent excitations are used, the conductivity distribution might be estimated with reasonable certainty. Since knowledge of the conductivity distribution is effectively an image of the conductivity, we will call the method "conductivity imaging".[41] The development closely follows that given by Wexler *et al.* ([54], [55]).

The geometry is shown in Fig.3.11. An array of electrodes is placed on the surface of the body to be measured. Current J_{in} is injected at one electrode and extracted at another. Potential measurements $\{\phi_1, \phi_2, \ldots \phi_n\}$ are made at the other electrodes. These are referenced to the potential, ϕ_{REF}, at an arbitrary but fixed electrode. The latter process constitutes one excitation. Note that potential measurements are not made at current sites. The electrode array shown is merely illustrative. The actual one used may not be square and may consist of more or less electrodes, depending upon the actual experiment.

The resulting surface voltage distribution is measured for several sets of excitations and stored for later processing. The measurements may be taken using an automated digitally controlled data acquisition system. The general method we will employ is to guess at the conductivity distribution and use it to calculate a potential distribution throughout the volume and in particular at the surface.[42] The guess is unlikely to agree with the true subsurface conductivity distribution and so the calculated and measured surface voltages will disagree. An algorithm which will iteratively refine the conductivity is needed. This will then be repeatedly applied until the measured and calculated surface voltages are in what is considered to be acceptable agreement.

The equations governing the problem may be easily derived. If we assume that the local conductivity is denoted κ and the frequency is low enough so that the electric field $\vec{E}$ may be expressed in terms of a scalar electric potential ψ,

$$\vec{E} = -\nabla\psi \tag{164}$$

Then by the equation of continuity

$$\nabla \cdot \vec{J} = -\frac{\partial \rho}{\partial t} = -f \tag{165}$$

where $\vec{J}$ is the current density and f is the impressed current source distribution within the volume of interest. These two equations with Ohm's Law yields the Poisson equation for continuous inhomogeneous media[43]

$$\nabla \cdot \kappa \nabla \psi = -f \tag{166}$$

For ease of computation, the region of interest (Fig.3.11) is assumed to be bounded by the measurement surface and five orthogonal plane faces. If the measurement surface were a horizontal plane, these six faces would form a cube. The volume of interest is divided into a finite element grid. In the simplest scheme, potentials are computed for each excitation at the node points (mesh intersections) and the conductivity is then estimated within the intervening regions. The conductivity distribution in the region of interest is initially assumed to be uniform and the iterative procedure to improve the conductivity estimates is then applied. The procedure is outlined below:

[39] The injection of a fixed current at a specific site and withdrawal from another specific site constitutes an excitation.

[40] This was seen in the 2-layer earth model (see Fig.3.10). Also, consider the simple example of an array of electrodes on the earth s surface, all at the same potential. This implies that a conductor is immediately beneath the measurement surface but does not say whether the conductor is a thin sheet or extends to large depths.

[41] This can lead to some confusion since the method is also referred to in the literature as impedance tomography. In this section "impedance tomography" will be reserved for those techniques assuming ray-like currents.

[42] A numerical method such as the finite element method is employed.

[43] Equation 166 is strictly true only for zero frequency. For slightly higher frequencies, it is valid if the conductivity is treated as a complex quantity (see next section). For still higher frequencies, the Helmholtz equation must be used.

1. **Calculation of potential and current density with Neumann boundary conditions -** Given the generally inhomogeneous conductivity distribution from the previous iteration, the potential distribution ψ is computed by solving the Poisson Equation 166. The potential distribution is in turn used to calculate the current density distribution $\vec{J}$ (A/m^2). This latter quantity is what we actually seek.

   In solving for the potential, the inhomogeneous Neumann boundary conditions are used, namely

$$\kappa(s)\left(\frac{\partial\psi_1}{\partial n}\bigg|_s\right) = h(s) \tag{167}$$

   where s denotes a point on the surface bounding the volume of interest, subscript "1" denotes a quantity derived from the first step of the iteration, n is the displacement in the direction normal to the surface and $h(s)$ (A/m^2) is the current density entering or leaving the medium over the element of bounding surface at that point. The quantities $h(s)$ are derived from the measured currents at the electrodes.[44] Where no current is impressed, $h(s) = 0$. This is true for all points on the bounding surface other than the current input and output electrodes. The justification for this on the measurement surface is that the conductivity of air is approximately 0. For the other faces, it is implicitly assumed that the bounded volume is sufficiently large that negligable current crosses those faces.

   The boundary conditions, assumed conductivity distribution and Poisson equation are then used to calculate the potential distribution throughout the volume, using one point on the measurement surface as a reference. This is normally done by a finite element method which computes the field by dividing the region into numerically manageable intervals called "finite elements". The method calculates the potential at the node points, using one of a number of field calculation methods (i.e., [53]). In simple versions, the nodes are vertices of the cube elements, but more sophisticated versions allow for nodes to be at other points. After the potentials are found at the node points, located at mesh intersections, the potentials at other points may be obtained by interpolation.

   Next we find the electric field throughout the volume from Equation 164 and then the current density distribution from

$$\vec{J}_1 = \kappa\vec{E}_1 \tag{168}$$

   Step 1 is repeated for all other excitations and the resulting fields are stored. [45]

2. **Calculation of potential with Dirichlet boundary conditions -** Next the interior potentials are calculated again by an independent method, namely by the use of the Dirichlet boundary conditions,

$$\psi_2(s) = g(s) \tag{169}$$

   on the measurement surface. (Here the subscript "2" denotes quantities derived from the second step of the iteration, and $g(s)$ are the potentials measured at the bounding surface, namely the measured ϕ_i at the potential electrodes.) In addition, the boundary conditions must include the Neumann condition at the current electrodes since measured potentials are not available at these sites.[46] Boundary condition at the reference electrode is, of course, $g(s) = 0$ and the Neumann condition $h(s) = 0$ is necessary on the other five faces. The quantity we wish to derive from this step is ψ_2.

3. **Calculation of conductivity -** As was stated in Section 3.4.1, the Poisson equation yields a unique solution ψ for specified κ, when a single boundary condition (Neumann or Dirichlet) is specified at each boundary point. In fact, the solution ψ can be used to derive the other boundary condition at

[44] The integral of $h(s)$ over the electrode surface yields the total current I. Electrodes can be modelled as hemispheres or points, the latter often being convenient.

[45] The current distribution will initially be approximate because the conductivity and hence the potentials are. However, reasonable current flow-line patterns are obtained even for very approximate κ. This is because the current is constrained to enter the measurement surface through one electrode, then spreads widely through the volume and must converge toward the other current electrode.

[46] Voltages measured at the current injection electrodes are prone to error due to contact-potential problems (see Section 3.1).

each point. What this means then, is that if the actual conductivity distribution κ is known, Ohm's Law states that $\vec{J_1} = \kappa \nabla \psi_2$. But the boundary conditions are based on measurements, subject to error, and κ is an estimate and thus the two different sets of boundary conditions will not yield the same internal fields.

We can, however, adjust κ to ensure that the two sets of boundary conditions are as compatible as possible in some sense, by minimizing a quantity related to some average over all points and excitations of $\left|\vec{J_1} + \kappa \nabla \psi_2\right|$. If we seek to optimize the solution in a least squares sense, we should minimize

$$R = \sum_{x} \int \int \int_V \left(\vec{J_1} + \kappa \nabla \psi_2\right) \cdot \left(\vec{J_1} + \kappa \nabla \psi_2\right) dv \tag{170}$$

where R is the squared residual sum, V is the region of interest and X denotes the excitations used. Because we have employed a finite element scheme, the integral over V is really a sum of integrals over the element volumes V_j, i.e.,

$$\begin{aligned} R &= \sum_{x} \sum_{j} \int \int \int_{V_j} \left(\vec{J_1} + \kappa_j \nabla \psi_2\right) \cdot \left(\vec{J_1} + \kappa_j \nabla \psi_2\right) dv \\ &= \sum_{x} \sum_{j} \int \int \int_{V_j} \left(\vec{J_1} \cdot \vec{J_1} + 2\kappa_j \vec{J_1} \cdot \nabla \psi_2 + \kappa_j^2 \nabla \psi_2 \cdot \nabla \psi_2\right) dv \end{aligned} \tag{171}$$

where κ_j is the conductivity distribution within element j.

The size of the elements may be chosen so that κ_j is constant within each element and then we minimize the residual by demanding

$$\frac{\partial R}{\partial \kappa_i} = \sum_{x} \int \int \int_{V_i} \left(2\vec{J_1} \cdot \nabla \psi_2 + 2\kappa_i \nabla \psi_2 \cdot \nabla \psi_2\right) dv = 0 \tag{172}$$

where $\vec{J_1}$ and ψ_2 are fixed at the previously estimated values. We can rearrange the last equation to give an estimate of the optimum conductivity distribution for the iteration,

$$\kappa_i = -\frac{\sum_x \int \int \int_{V_i} \vec{J_1} \cdot \nabla \psi_2 dv}{\sum_x \int \int \int_{V_i} \nabla \psi_2 \cdot \nabla \psi_2 dv} \tag{173}$$

This last equation is then applied over all elements in the volume to obtain the revised estimate of the conductivity distribution.[47]

4. **Recursive improvement** - Steps 1, 2 and 3 constitute an iteration. The next iteration begins again by solving the Neumann boundary value problem for all excitations using the new conductivity distribution estimate. The computed potentials at the boundary are compared with the measured ones. If the differences exceed some *a priori* thresholds or if insufficient iterations have been performed[48], the iteration continues with the solution of the Dirichlet boundary value problem. Otherwise the resulting image (2D or 3D depending on the problem) of the conductivity distribution is processed by one of a number of standard techniques and is output.

   As a simple but somewhat contrived, example of the three dimensional case, a cube with four layers of finite elements is shown in Fig.3.12 ([54]). Layers two and three contain a square object whose conductivity is five times the host medium. Simulated "measurements" have been made at the top surface only. Clearly the estimation improves with iteration count. Initially a conductivity artifact appears at the surface but it later disappears. Note that a large number of iterations are needed and even then the image is quite crude. Objects of a more general shape also tend to be crudely imaged. Furthermore, computer time is excessive, being of the order of an hour on a large mainframe computer. Work is underway to solve both the accuracy and speed problems.

[47] Note that no matrix operations are necessary.

[48] The minimum necessary number of iterations is a heuristic parameter which is derived after considerable user experience on a particular problem.

3.6 Induced Polarization (IP)

Assume now that rather than d.c., we are operating at a very low frequency, ω. Again, as for electrostatics, we assume that magnetic effects can be neglected. Frequently we find that σ is a function of ω and is a complex quantity, i.e. the current is out of phase with the voltage. Thus,[49]

$$\sigma'(i\omega) = \sigma(i\omega) + i\omega\epsilon(i\omega) \tag{174}$$

with σ, ϵ real and

$$\vec{J}(i\omega) = \sigma'(i\omega)\,\vec{E}(i\omega) \tag{175}$$

Components of $\vec{J}$ and $\vec{E}$ are phasors and thus, for example, the real physical quantity $e_x(t)$ (subscript x denotes the x component) is related to the complex phasor by

$$e_x(t) = \Re\left\{E_x(i\omega)e^{i\omega t}\right\} = |E_x|\cos(\omega t + \phi_{E_x}) \tag{176}$$

and

$$\begin{aligned} |J_x| &= |\sigma|\,|E_x| \\ \phi_{J_x} &= \phi_\sigma + \phi_{E_x} \end{aligned} \tag{177}$$

where ϕ_{J_x} is the phase of $\vec{J}_x$, ϕ_σ is the phase of σ and ϕ_{E_x} is the phase of $\vec{E}_x$.

Problems in IP are usually solved by assuming a model for $\rho = (\sigma')^{-1}$ and then solving a particular boundary value problem as for d.c. conductivity methods.[50]

A simple model for ρ is the N-pole model

$$\rho(s) = \sum_{n=0}^{N} A_n \frac{1}{\alpha_n + s} \tag{178}$$

with α_n, A_n real and s being the Laplace variable. Another model commonly found in the literature is

$$\rho(s) = \sum_{n=0}^{N} \frac{1}{G_n + sC_n} + \rho_\infty \tag{179}$$

with G_n, C_n, ρ_∞ all real. This allows $|\rho|$ to be nonzero as $s \to \infty$. The Cole-Cole model is also very popular:

$$\rho(s) = \rho_0\left\{1 - m_0\left(1 - \left[1 + (i\omega\tau)^k\right]^{-1}\right)\right\} \tag{180}$$

where ρ_0, m_0, τ are real constants and K is an empirically adjusted noninteger.

All these are phenomenological models which in some manner describe the electrical properties of the material being probed. The cause of IP is not known in detail.

Intuitively, however, if the impedance is complex and decreases with frequency, it must be related to capacitive effects in the medium (recall that displacement current, although small, has not been neglected). These capacitive effects are due to electrochemical and other electromagnetic properties of the medium. To illustrate this we use a simple model:

Assume a single sphere, resistivity ρ_1, radius a, in a uniform medium of resistivity ρ and assume there exists a (complex) interface impedance η_m (ohm-m^2). Primary field E_0 is uniform and along the polar axis of a spherical coordinate system (r, θ, ϕ) centered on the sphere (Fig.3.13). It is assumed that ω is small and Laplace's equation holds. The analysis is routine. Suitable potentials are:

$$\psi_1 = A_0 r\cos\theta \quad \text{for} \quad 0 < r \le a \tag{181}$$

$$\psi = -E_0 r\cos\theta + Ar^{-2}\cos\theta \quad \text{for} \quad r \ge a \tag{182}$$

[49] This is really the same as lumping the small effect of displacement current into an "effective conductivity".

[50] This is possible since the frequency is assumed sufficiently low so that the Poisson/Laplace equations apply.

where A_0, A are constants. Boundary conditions at $r = a$ are:

$$\frac{1}{\rho}\frac{\partial \psi}{\partial r} = \frac{1}{\rho_1}\frac{\partial \psi_1}{\partial r} \tag{183}$$

$$\psi_1 = \psi - \frac{\eta_m}{\rho}\frac{\partial \psi}{\partial r} \tag{184}$$

Equation 183 derives from J_r being continuous while 184 is due to the voltage drop across $r = a$ being $\eta_m J_r$. Solving Equations 181 to 184 yields

$$\psi = -E_0 r \cos\theta + a^3 \chi E_0 r^{-2} \cos\theta \tag{185}$$

where

$$\chi = \frac{1-\delta}{1+2\delta} \tag{186}$$

and

$$\delta = \frac{\rho_1}{\rho} + \frac{\eta_m}{\rho a} \tag{187}$$

Now assume N such particles (polar axes aligned) in a spherical region of radius r_0 (Fig.3.14) and if interactions between particles are ignored then at point P we have

$$\psi = -E_0 r \cos\theta + \sum_i^N \frac{E_0 a^3 \chi}{r_i^2} \cos\theta_i$$

Typically, $r_0 \ll r$, $r_i \approx r$ and $\theta_i \approx \theta$. Then

$$\psi \approx -E_0 r \cos\theta + N a^3 \chi E_0 r^{-2} \cos\theta \tag{188}$$

But if we assume the spherical region is a continuum with effective resistivity ρ_e, then

$$\psi \approx -E_0 r \cos\theta + \frac{r_0^3}{r^2}\frac{\rho - \rho_e}{\rho + 2\rho_e} E_0 \cos\theta \tag{189}$$

Equating 188 and 189 yields the important result:[51]

$$\frac{\rho}{\rho_e} = \frac{1-\nu\chi}{1+2\nu\chi} \tag{190}$$

where $\nu = N a^3 / r_0^3$ is the volume fraction of particles.

If we assume $\rho_1/\rho \ll 1$ and $\nu \ll 1$ (i.e., many small highly conducting particles in an electrolyte) and if

$$\delta = \frac{1}{2\,(i\omega\tau)^k} \tag{191}$$

then we obtain the Cole-Cole equation 180.

Equation 191 implies that the interface impedance is capacitive in nature. The Cole-Cole model has been widely used since it fits a large body of accumulated data quite well.

Finally, it should be noted that IP measurements are commonly made in the time domain. In such cases it is assumed that the time dependent impressed current, $j_x(t)$, is known (we restrict ourselves to the x direction) and we wish to predict $e_x(t)$ given a resistivity model. As an example, if we assume a model for $\rho(s)$ as in Equation 178[52] and if we assume a step function impressed current,

$$j_x(t) = J_0 u(t) \tag{192}$$

then

$$J_x(s) = J_0/s \tag{193}$$

[51] This is analogous to the Clausius-Mosotti equation in dielectric theory.

[52] We use capital letters to denote Laplace variables.

$$e_z(t) = L^{-1}\left[\rho(s)J_z(s)\right] = J_0 \sum_{n=0}^{N} A_n L^{-1}\left[\frac{1}{s(s+\alpha_n)}\right] \tag{194}$$

which becomes

$$e_z(t) = J_0 \sum_{n=0}^{N} \frac{A_n}{\alpha_n}\left[1 - e^{-\alpha_n t}\right] u(t) \tag{195}$$

Letting $e_{0z} = e_z(\infty)$, we can plot $A_z(t) = e_z(t)/e_{0z}$ (normalized step frequency response) versus t. This is shown in Fig.3.15.

In practice, it is often convenient to use a continuous on-off current waveform such as Fig.3.16. The analysis is similar to above. The waveform is a sum of shifted step functions and one usually analyzes the "steady-state transient response". The output then looks like that of Fig.3.17.

Time domain induced polarization has an advantage over the frequency domain in that many frequencies are excited by one measurement, in principle providing more information. Unfortunately, the analysis is much more complicated for the time domain.

4 Electromagnetic Induction

4.1 Introduction

The method of electromagnetic induction is widely used for detecting conductive objects in geophysics, nondestructive testing, detection of mines and artillery shells, archeological exploration and treasure hunting. A conductive object is exposed to a time-varying magnetic field (usually in the Hz to KHz range) produced by a current-carrying primary coil. The resulting eddy currents induced in the object produce a secondary time-varying magnetic field which is detected by another (or occasionally the same) coil.

The receive coil can, of course, detect variations in the geomagnetic field and it is important that the signal due to the geomagnetic field be substantially less than that due to the object of interest. The geomagnetic spectrum is shown in Fig.4.1. Calculation of the geomagnetic "noise" is dependent upon the receiver design, but we can obtain a rough estimate. If we assume a receive coil of radius r, a geomagnetic flux density at ω Hz of B_ω^n, then the induced emf $|V_\omega^n|$ at frequency ω is given by

$$|V_\omega^n| = \left|\pi r^2 \omega S_\omega^n \overline{B_1^n}\right| \tag{196}$$

where the bar denotes an average value and

$$S_\omega^n = \overline{B_\omega^n}/\overline{B_1^n} \tag{197}$$

Assuming $r = 0.2$m, $\overline{B_1^n} = 1 \times 10^{-9}$T,[53] $\omega = 2\pi \times 10^3$Hz, $S_\omega^n = 1/30$ (from Fig.4.1), we obtain

$$|V_{1000}^n| \approx 2.6 \times 10^{-8} \text{ Volts at } 1 \text{ KHz}$$

Sensitive instrumentation can and routinely does measure such small voltages in the course of fundamental studies of the geomagnetic field. Note that noise voltage is proportional to the receiver coil cross sectional area. Geometries associated with mines and artillery shells typically use coils with radii of less than 1 meter and detected signals are of the order of 1×10^{-3}Volts or greater so geomagnetic noise does not pose a problem. In nondestructive testing the signal of interest is generally much larger still, owing to the small coils (radii are in the mm to cm range) and close-coupled geometry of coils and object, and geomagnetic noise is even less of a problem. In geoexploration, on the other hand, received signals are usually very weak which necessitates large receive coils. Geomagnetic noise must then be contended with and occasionally can even prohibit exploration. In any case, coherent averaging can increase the S/N by substantial amounts since the geomagnetic signal is essentially stochastic.

The origin of the geomagnetic spectrum is beyond the scope of this course and the student is referred to [60] for further details. We only note that the effect of geomagnetic noise generally tends to decrease with increasing frequency. This is because $|V_\omega^n|$ is proportional to ω and the spectral density decreases faster than ω^{-1} with the exception of the gyromagnetic resonance region.

[53] To be strictly correct, the measurement band must be specified in order to determine the noise at a particular frequency. However, this value is roughly correct for typical magnetometer bandwidths.

4.2 Principles of Detection

4.2.1 General Principles

There are basically only two types of electromagnetic induction detectors - continuous wave (CW) and transient detectors.

Continuous wave detectors generally employ a single frequency sinusoidal transmitter waveform. They may then be further subdivided into frequency shift detectors and mutual inductance detectors. Frequency shift detectors usually employ a resonant oscillator circuit with a coil acting as the inductive element. In isolation, the oscillator operates at a fixed frequency determined in part by the inductor. If the coil is now brought near a conducting or magnetic body, the effective inductance changes and hence the frequency changes. A variety of techniques are employed to detect the frequency shift. One of the most straightforward is to mix a local oscillator signal at the fundamental frequency with the shifted frequency and then measure the beat frequency with a counter.

Mutual inductance detectors rely instead on two or more coils in close proximity. The coils are oriented such that ideally the mutual inductance between them is zero. One coil (the transmitter or primary) is excited by a single frequency sinusoidal signal. In the absence of an object, the signal coupled into the other coil(s) (receiver or secondary) is zero.With a conductive or magnetic object present, the mutual coupling between the coils changes and a signal is induced in the receiver coil(s).[54]

Transient detectors also use a transmitter coil and one or more receive coils. Current in the transmitter coil is switched off and on rapidly. Transient currents are induced in the receive coil(s) even in the absence of a target object. To eliminate this mutual coupling signal, some systems use two coaxial receive coils which are equidistant from the transmitter coil. The coils are wound in opposition and fed to a difference amplifier which accordingly produces a null output. A target placed near one receive coil will induce a bigger signal in that coil than the other and hence a signal will appear at the amplifier output. The problem with this method is that the signal induced by the primary coil in the secondary coils is up to 10^6 times that induced by the object. Thus extremely accurate coil matching and alignment (balancing) is necessary if the object is to be detected.

An alternative transient approach is to use a pulsed transmit current and to only measure the voltage in the receive coil during the quiescent period between pulses. Provided the transients due to primary/secondary mutual coupling decay faster than those due to the target, the method will work without the need for critical coil balancing. This method is often referred to as "pulse induction". The chief drawback of pulse induction over the balanced 3 coil arrangement is that pulse induction must have a duty cycle less than 100 % whereas this is not a constraint for the latter method. The lack of a need for critical coil balancing for pulse induction more than makes up for this disadvantage.

As one might expect, the continuous wave and transient methods are connected via the Laplace Transform. We shall discuss this point later. Continuous wave detectors generally require less power for a given sensitivity than do transient detectors. On the other hand, CW detectors yield less information about the object since they operate at a single frequency, rather than exciting with a broad spectrum as do transient detectors. Furthermore, mutual inductance-type detectors require very critical coil alignment too, which may detract from the robustness.

Many detectors, as mentioned previously, use a transmit coil and one or more receive coils. The choice of geometries is almost limitless, although they fall into a few general categories. The basic idea is to have a mutual inductance that is zero in the absence of a target and that is measurable with the object present. This is not always very simple to do. To understand better how to achieve this goal, we must first digress to discuss the field of a coil and mutual inductance in more detail.

4.2.2 Field of a Coil

Assume a loop carrying current I situated in the $x-y$ plane (Fig.4.3). We wish to calculate the vector potential at a point P, which because of axial symmetry may be chosen without loss of generality at

[54] Other variants use a circuit which very near oscillation. The small change in mutual inductance induces oscillation. This has the advantage of low power consumption.

$\phi = 0$.[55] The vector potential is given by:[56]

$$\vec{A}(\vec{x}) = \frac{\mu}{4\pi}\int_{V'}\frac{\vec{J}\left(\vec{x'}\right)}{\left|\vec{x}-\vec{x'}\right|}d^3\vec{x'} \tag{198}$$

The current density has only a ϕ component and is given by

$$\vec{J} = -J_\phi \sin\phi'\hat{x} + J_\phi \cos\phi'\hat{y} = J_\phi\hat{\phi} \tag{199}$$

[57]with

$$J_\phi = I\sin\theta'\delta(\cos\theta')\frac{\delta(r'-a)}{a} \tag{200}$$

Since we are observing at $\phi = 0$, the x component of the current density will yield no contribution on integration. Also, since $\vec{J}$ has only a ϕ component, so does $\vec{A}$, i.e, $\vec{A} = A_\phi\hat{\phi}$. Thus

$$A_\phi(r,\theta) = \frac{\mu I}{4\pi a}\int r'^2 dr' d\Omega' \frac{\sin\theta'\cos\phi'\delta(\cos\theta')\delta(r'-a)}{\left|\vec{x}-\vec{x'}\right|} \tag{201}$$

Now $1/\left|\vec{x}-\vec{x'}\right|$ can be expanded as a sum of spherical harmonics, $Y_{lm}(\theta,\phi)$.

$$\frac{1}{\left|\vec{x}-\vec{x'}\right|} = 4\pi\sum_{l=0}^{\infty}\sum_{m=-l}^{+l}\frac{1}{2l+1}\frac{r_<^l}{r_>^l}Y_{lm}^*(\theta',\phi')Y_{lm}(\theta,\phi) \tag{202}$$

where $r_<$ ($r_>$) is the smaller (larger) of a and r. Substitution of Equation 202 into 201 and application of the properties of spherical harmonics yields

$$A_\phi(r,\theta) = -\frac{\mu}{4}Ia\sum_{n=0}^{\infty}\frac{(-1)^n(2n-1)!!}{2^n(n+1)!}\frac{r_<^{2n+1}}{r_>^{2n+2}}P_{2n+1}^1(\cos\theta) \tag{203}$$

[58]where $P_l^m(\cos\theta)$ is the associated Legendre function and

$$(2n-1)!! = (2n-1)\cdot(2n-3)\cdots 5\cdot 3\cdot 1$$

Using $\vec{B} = \nabla\times\vec{A}$ (see Section 4.3) we find that

$$B_r = \frac{\mu Ia}{2r}\sum_{n=0}^{\infty}\frac{(-1)^n(2n+1)!!}{2^n n!}\frac{r_<^{2n+1}}{r_>^{2n+2}}P_{2n+1}(\cos\theta) \tag{204}$$

where $P_n(\cos\theta)$ is a Legendre Polynomial and

$$B_\theta = \frac{\mu Ia^2}{4}\sum_{n=0}^{\infty}\frac{(-1)^n(2n+1)!!}{2^n(n+1)!}\left(\frac{2n+2}{2n+1}\right)\frac{1}{a^3}\left(\frac{r}{a}\right)^{2n}P_{2n+1}^1(\cos\theta) \tag{205}$$

$$B_\theta = -\frac{\mu Ia^2}{4}\sum_{n=0}^{\infty}\frac{(-1)^n(2n+1)!!}{2^n(n+1)!}\frac{1}{r^3}\left(\frac{a}{r}\right)^{2n}P_{2n+1}^1(\cos\theta) \tag{206}$$

where the first equation for B_θ is for $r < a$ and the second is for $r > a$. There are two important cases.

For $r \gg a$ only the $n = 0$ term is significant.

$$B_r = \frac{\mu Ia^2}{2}\frac{\cos\theta}{r^3}$$

[55] Again, primed coordinates are source coordinates, unprimed are field coordinates.
[56] This will be derived in Section 4.3.
[57] Why have we bothered to resolve $\vec{J}$ into x and y components?
[58] Can you derive the steps from Equation 202 to 203?

$$B_\theta = \frac{\mu I a^2}{4} \frac{\sin\theta}{r^3} \tag{207}$$

These are just the field components of a dipole. Thus, sufficiently far from a loop of wire, the field is dipolar in nature.

For $r \ll a$,

$$\vec{B} = \frac{\mu I}{2a}\hat{z} \tag{208}$$

In other words, close to the coil we have a uniform field in the direction of the coil axis.

4.2.3 Mutual Inductance of Two Coils

We are now in a position to discuss the mutual inductance of two coils. We assume the transmitter and receiver are two simple loops of negligable cross-section and are situated in free space. If a sinusoidal current flowing through loop 1 (the transmitter) is denoted I_1, then the induced emf in loop 2, V_2, is

$$V_2 = -i\omega M_{12} I_1 \tag{209}$$

where ω is the angular frequency of excitation and M_{12} is the "coefficient of mutual induction" or simply the "mutual inductance". By the reciprocity theorem, we can interchange transmitter and receiver and hence

$$M_{12} = M_{21} \tag{210}$$

Referring to Fig. 4.4, the magnetic potential at point $\vec{x_2}$ of the receiver loop is given by Equation 198 in the form

$$\vec{A}(\vec{x_2}) = \frac{\mu_0 I}{4\pi} \oint_1 \frac{d\vec{l}_1}{|\vec{x_2} - \vec{x_1}|} \tag{211}$$

where subscript "1" refers to quantities measured at the transmitter and subscript "2" refers to quantities measured at the receiver. The magnetic flux intercepted by the receiver is

$$\begin{aligned} \Phi_2 &= \int_2 \vec{B}(\vec{x_2}) \cdot d\vec{s_2} \\ &= \int_2 \left[\nabla \times \vec{A}(\vec{x_2})\right] \cdot d\vec{s_2} \end{aligned} \tag{212}$$

But

$$V_2 = -i\omega\Phi_2 \tag{213}$$

which implies that

$$M_{12} = \Phi_2 / I_1 \tag{214}$$

Thus we have,

$$M_{12} = \frac{\mu_0}{4\pi} \int_2 d\vec{s_2} \cdot \left(\nabla_2 \times \oint_1 \frac{d\vec{l}_1}{|\vec{x_2} - \vec{x_1}|} \right) \tag{215}$$

This general equation can be very difficult to solve for arbitrary geometries. For the special case when the interloop distance greatly exceeds the coil diameters, the field of the transmitter at the receiver is that of a dipole. The general expression for the vector potential of a dipole is[59]

$$\vec{A}(\vec{x}) = \frac{\mu_0}{4\pi} \vec{m} \times \nabla' \frac{1}{\left|\vec{x} - \vec{x'}\right|} \tag{216}$$

For a transmitter loop of radius a_1, with unit vector $\hat{n_1}$ normal to the plane of the loop and current I_1 flowing, we get

$$\vec{A}(\vec{x_2}) = \frac{\mu_0}{4\pi} \left[I_1 \pi a_1^2 \hat{n_1}\right] \times \nabla_1 \frac{1}{|\vec{x_2} - \vec{x_1}|} \tag{217}$$

[59] Dipole moment is $\vec{m}$, source coordinates are primed, field coordinates are unprimed.

Using Equations 212 and 214 and realizing that $\vec{A}(\vec{x_2})$ is approximately constant over the area of the receiver loop, we find[60]

$$M_{12} = \frac{\mu_0 \pi}{4} a_1^2 a_2^2 \hat{n_2} \cdot \nabla_2 \times \left(\hat{n_1} \times \nabla_1 \frac{1}{|\vec{x_2} - \vec{x_1}|} \right) \tag{218}$$

Three special cases arise. For all three, the distance between loop centers is l and $l \gg a_1, a_2$.

1. **Coaxial loops (Fig.4.5a):** We have $\hat{n_1} \cdot \hat{n_2} = 1$ and

$$M_{12} = \mu_0 \pi \frac{a_1^2 a_2^2}{2l^3} \tag{219}$$

2. **Coplanar loops (Fig.4.5b):** We have $\hat{n_1} \cdot \hat{n_2} = 1$ and

$$M_{12} = -\mu_0 \pi \frac{a_1^2 a_2^2}{4l^3} \tag{220}$$

3. **Axes of two loops intersect at right angles (Fig.4.5c):** We have $\hat{n_1} \cdot \hat{n_2} = 0$ and

$$M_{12} = 0 \tag{221}$$

Even when the loop separation is not many times the coil diameters, these general trends hold. The mutual inductance of the coaxial geometry is greater in magnitude and opposite in sign to that of the coplanar geometry and the mutual inductance of the orthogonal axes geometry is substantially smaller in magnitude than the other two. For this reason, cases 1 and 2 are often called "maximum coupled" while case 3 is called "minimum coupled".

According to Equation 209, any change in the voltage induced in the receiver coil due to the presence of an anomaly, could be interpreted as a change in the mutual inductance of the transmitter/receiver system, i.e.,

$$\frac{\triangle V_2}{V_2} = \frac{\triangle M_{12}}{M_{12}} \tag{222}$$

This ratio is called the "electromagnetic anomaly" (measured in ppm) and it should be remarked that the quantity $\triangle M_{12}$ is generally complex since V_2 in the presence of the anomaly is generally out of phase with V_2 in the absence of any anomaly.

Such small changes in mutual inductance would stand out best for a system with a small mutual inductance to begin with. This suggests a minimum coupled system. This is, of course, only true in air. If one wishes to detect an anomaly (object) buried in a conducting medium, it is necessary to determine the mutual inductance due to the presence of the medium. This involves detailed electromagnetic analysis, as we shall see in the next section, and is very dependent on geometry. As an example, if the medium is assumed to be an infinite flat sheet, the mutual inductance can be determined for a variety of coil configurations. These are shown in Figs.4.6a to 4.6e.

Clearly for a viable system, we want a geometry that maximizes the change in inductance for the object of interest while minimizing that due to the host medium. Thus for example, the configuration of Fig.4.6a might be preferred to detect a small object buried just under the surface, whereas that of Fig.4.6e would be preferred to detect the conductive sheet itself. The choice of optimum geometry is often very difficult to make and in many cases, it is unclear which of several geometries is optimum, if indeed any are.

4.2.4 Detection Techniques

We have been considering up to now only inductively coupled systems. However, limited applicability has been found for conductive input-inductive output and inductive input-conductive output systems which are essentially a hybrid of electromagnetic induction and resistivity methods. These methods are rather obscure and we will say no more about them.

[60] $\hat{n_2}$, a_2 are the unit normal and radius of the receiver loop.

Techniques of interest in most applications involve measuring both the amplitude and phase of the receiver signal relative to the transmitter (for single frequencies). As we shall see, the receiver signal generally is not in phase with the transmitter signal and thus the maximum amount of information is derived from such a measurement. Transient measurements also derive maximum information since effectively they measure phase and amplitude over a wide range of frequencies.

In geophysical applications, there are two additional, lesser-used techniques. Dip-angle or tilt-angle techniques measure the orientation of the total (primary plus secondary) field by finding the orientation of the receiver coil at which the receive signal is a minimum.[61] Also, one can make intensity measurements without phase measurements. This is sometimes done by using a very large loop of wire or a very long straight wire ohmically coupled to the ground at both ends (length $\sim$ kilometers) as a transmitter. A receiver coil can then survey a large area, travelling up to 1/4 to 1/2 the length of the wire from the source without need of an attached transmitter. Analysis for this method is difficult compared to a dipole source due to the presence of conduction currents in the ground. For further descriptions of such techniques, the reader is referred to [4].

Finally, we must say a word about magnetotelluric methods. In the previously described techniques, the source fields have been provided by artificial means. It is possible to use the geoelectromagnetic spectrum as a source, however, since we have seen that it is measurable at low frequencies. The method involves measuring the geoelectric field in one horizontal direction, (x), and the geomagnetic field in a horizontal direction perpendicular to the first (y) at the air-ground interface. For a uniform earth and plane wave incidence it can be shown that[62]

$$Z^2(\omega) = \left[\frac{E_x(\omega)}{H_y(\omega)}\right]^2_{z=0} = \frac{\mu\omega}{\sigma} \tag{223}$$

provided

$$\frac{\omega}{\mu c^2}\frac{\sin^2\theta}{\left(\sigma^2+\epsilon^2\omega^2\right)^{1/2}} \ll 1 \tag{224}$$

where θ is the angle of incidence of the geoelectromagnetic plane wave and μ, σ, ϵ are the electromagnetic parameters of the earth. Under these assumptions the surface impedance $Z(\omega)$ is independent of θ, which is highly desirable from the point of view of measurements. Recalling our electrostatics discussions, we recognize that Equation 223 can be arranged to yield a formula for resistivity, $\rho = 1/\sigma$,

$$\rho = \frac{1}{\mu\omega}\left[\frac{E_x(\omega)}{H_y(\omega)}\right]^2 \tag{225}$$

and we see that if the earth is horizontally stratified, we can deduce information about it by measuring the effective resistivity given by Equation 225. As for conductivity measurements, analysis can be very difficult and results difficult to interpret depending on the complexity of the underlying strata. Models have been developed for different plane wave polarizations, various types of stratification and for a current sheet source at ionospheric altitudes. The main use of magnetotelluric measurements is for depth-sounding, since most models assume that horizontal field variations are small.

4.3 Quasi-static Electromagnetic Theory

We start off as usual with the basic Maxwell's equations,

$$\nabla \times \vec{E} = -\frac{\partial \vec{B}}{\partial t} \tag{226}$$

$$\nabla \cdot \vec{D} = \rho \tag{227}$$

[61] The minimum is a null for free space. In the presence of a conductor, the primary and secondary fields are out of phase and hence we get an elliptically polarized total field which cannot be represented by a simple vector. We get a minimum when the major axis of the polarisation ellipse is contained within the plane of the receiver loop.

[62] It is assumed that an incident plane wave has a magnetic component in the y direction and travels in the $x-z$ plane. The earth/air interface is in the $x-y$ plane at $z=0$. See [2] Chapter VI for details.

$$\nabla \times \vec{H} = \vec{J} + \frac{\partial \vec{D}}{\partial t} \tag{228}$$

$$\nabla \cdot \vec{B} = 0 \tag{229}$$

and we assume linear isotropic media such that

$$\vec{B} = \mu \vec{H} \tag{230}$$

$$\vec{D} = \epsilon \vec{E} \tag{231}$$

$$\vec{J} = \sigma \vec{E} \tag{232}$$

Furthermore, we assume that charge does not accumulate[63] and hence $\rho = 0$. Maxwell's equations become

$$\nabla \times \vec{E} = -\mu \frac{\partial \vec{H}}{\partial t} \tag{233}$$

$$\nabla \cdot \vec{E} = 0 \tag{234}$$

$$\nabla \times \vec{H} = \sigma \vec{E} + \epsilon \frac{\partial \vec{E}}{\partial t} + \left[\vec{J}_0\right] \tag{235}$$

$$\nabla \cdot \vec{H} = 0 \tag{236}$$

The current density, $\vec{J}_0$, in square brackets in Equation 235 is added when there is an impressed current, that is, a current source independent of the electromagnetic field. Equations 233 and 235 can be combined to yield

$$\nabla^2 \vec{E} - \sigma\mu \frac{\partial \vec{E}}{\partial t} - \epsilon\mu \frac{\partial^2 \vec{E}}{\partial t^2} = 0 \tag{237}$$

$$\nabla^2 \vec{H} - \sigma\mu \frac{\partial \vec{H}}{\partial t} - \epsilon\mu \frac{\partial^2 \vec{H}}{\partial t^2} = 0 \tag{238}$$

Clearly, $\vec{E}$ and $\vec{H}$ propagate as dispersive waves. If we assume time harmonic solutions for $\vec{E}$ and $\vec{H}$, (i.e. $\vec{H}(\vec{r},t) = \Re\left\{\vec{H}(\vec{r},\omega)\exp(i\omega t)\right\}$) then Equations 237 and 238 become

$$\nabla^2 \vec{E} - i\sigma\mu\omega \vec{E} + \epsilon\mu\omega^2 \vec{E} = 0 \tag{239}$$

$$\nabla^2 \vec{H} - i\sigma\mu\omega \vec{H} + \epsilon\mu\omega^2 \vec{H} = 0 \tag{240}$$

It is cumbersome to deal with two quantities which satisfy Equations 237 and 238 and which must also satisfy 234 and 236. It would be convenient if $\vec{E}$ and $\vec{H}$ could be replaced by a single potential. There are numerous potentials from which to choose, and generally we choose the one which most simplifies a particular problem. For the present, we whall choose the vector potential, $\vec{A}$, given by

$$\vec{B} = \nabla \times \vec{A} \tag{241}$$

which satisfies Equation 229. Also by substituting 241 into 226 we get

$$\vec{E} = -\frac{\partial \vec{A}}{\partial t} - \nabla\phi \tag{242}$$

where ϕ is the scalar potential associated with $\vec{A}$. Since we will be restricting ourselves to source-free problems, it is wise to choose the Coulomb gauge.

$$\nabla \cdot \vec{A} = 0 \tag{243}$$

[63] For a finite conductivity, charge density reaches its steady-state value in a time $t \approx \epsilon/\sigma$.

Substituting Equation 234 into 242 and using 243 yields $\phi = 0$ and

$$\vec{E} = -\frac{\partial \vec{A}}{\partial t} \tag{244}$$

If we substitute Equations 244 and 243 into 235, we find (neglecting $\vec{J}_0$)

$$\nabla^2 \vec{A} - \sigma\mu\frac{\partial \vec{A}}{\partial t} - \epsilon\mu\frac{\partial^2 \vec{A}}{\partial t^2} = 0 \tag{245}$$

or in time harmonic form,

$$\nabla^2 \vec{A} - i\sigma\mu\omega\vec{A} + \epsilon\mu\omega^2\vec{A} = 0 \tag{246}$$

Now we must look at the relative contributions of the terms in Equation 246. In free space $\mu_0 = 4\pi \times 10^{-7}$ H/m, $\epsilon_0 \approx 8.89 \times 10^{-12}$ farads/m and $\sigma \approx 0$. Typical induction frequencies are from 1-100 KHz. Thus Equation 246 becomes

$$\nabla^2 \vec{A} = 0 \tag{247}$$

The ratio of magnitudes of the third to the second term of Equation 246 is equal to $(\epsilon/\sigma)\omega$ where $\epsilon = \epsilon_r\epsilon_0$ and ϵ_r is the relative permittivity (dielectric constant) of the material. A look at Table 3.1 shows that ϵ_r is typically between 1 and 10 with the exception of water which is 81 (rocks typically have $\epsilon_r \sim 9$, ice has $\epsilon_r \approx 4$ and ϵ_r for soils varies from 4-30 depending on water content).[64] Thus even for an extreme case when $\sigma \sim 10^{-3}$ S/m and $\epsilon_r = 9$, the ratio of the third to second term is $\sim 5.6 \times 10^{-4}$ at 1 KHz frequency. Even at 100 KHz, the ratio is only 0.056. For highly conductive rocks with $\sigma \sim 10^4$ S/m, the ratio drops to 5×10^{-11}. Note that in water ($\epsilon_r = 81, \sigma_{max} \sim 3 \times 10^{-2}$ S/m) or some very wet soils ($\epsilon_{rmax} \sim 30, \sigma_{max} \sim 10^{-2}$ S/m) the real term may be non-negligable compared to the imaginary term at the high end of the induction frequency range ($\sim$ 100 KHz). For the most part, however, we can neglect the third term in Equation 246 and write

$$\nabla^2 \vec{A} - i\sigma\mu\omega\vec{A} = 0 \tag{248}$$

or in the time domain,

$$\nabla^2 \vec{A} - \sigma\mu\frac{\partial \vec{A}}{\partial t} = 0 \tag{249}$$

The latter equation is recognized as the vector diffusion equation and thus $\vec{A}$ does not propagate as a steady wave. The neglection of the third term in equation Equation 246 is equivalent to neglecting displacement current.[65] This in turn is equivalent to saying that electric and magnetic fields are instantaneously propagated. Equation 249 can also be written as

$$\nabla^2 \vec{A} = -\mu\vec{J} \tag{250}$$

whose solution in unbounded space is given in rectangular coodinates by[66]

$$\vec{A}(\vec{x}) = \frac{\mu}{4\pi}\int_{V'} \frac{\vec{J}\left(\vec{x'}\right)}{\left|\vec{x} - \vec{x'}\right|} d^3\vec{x'} \tag{251}$$

with $\vec{J} = 0$ outside the volume V'.

[64] Dielectric constants vary slowly in the KHz to MHz region since any resonant structure occurs at much higher frequencies.

[65] This approximation is generally referred to as the "quasi-static approximation". There is some confusion in the use of this name. Sometimes the name refers to the situation when frequency is so low that $\nabla^2 \vec{A} = 0$. Also, let d be a typical source dimension, r the source to detector distance and λ the wavelength. Jackson [5] defines the "near (static) zone" as being $d \ll r \ll \lambda$ and the "quasi-static zone" as being $r \ll \lambda$. However, Wait [2] says that the "quasi-static limit" occurs in what Jackson calls the near zone.

[66] Equation 251 is not generally valid for curvilinear coordinates in the same manner that the components of $\nabla^2 \vec{A}$ have no simple meaning for other than cartesian coordinates.

Likewise, the same approximations make Equations 237 to 240 become

$$\nabla^2 \vec{E} = -\sigma\mu \frac{\partial \vec{E}}{\partial t} = 0$$

$$\nabla^2 \vec{H} = -\sigma\mu \frac{\partial \vec{H}}{\partial t} = 0 \tag{252}$$

$$\nabla^2 \vec{E} = -i\sigma\mu\omega \vec{E} = 0$$

$$\nabla^2 \vec{H} = -i\sigma\mu\omega \vec{H} = 0 \tag{253}$$

To illustrate the general nature of solutions of Equations 252 and 253, we choose a situation in which the fields vary only with x and in which $\vec{H}$ is plane polarized in the y direction. Then

$$H_y(x,t) = H_0 \exp\left[i\omega t \pm (i\sigma\mu\omega)^{1/2} x\right] \tag{254}$$

$$J_z(x,t) = \sigma E_z(x,t) = (i\sigma\mu\omega)^{1/2} H_y(x,t) \tag{255}$$

This may be written

$$H_y = H_0 \exp\left[-\left(\frac{\sigma\mu\omega}{2}\right)^{1/2} x\right] \exp\left[i\left(\omega t - \left\{\frac{\sigma\mu\omega}{2}\right\}^{1/2} x\right)\right] \tag{256}$$

$$J_z = (i\sigma\mu\omega)^{1/2} H_0 \exp\left[-\left(\frac{\sigma\mu\omega}{2}\right)^{1/2} x\right] \exp\left[i\left(\omega t - \left\{\frac{\sigma\mu\omega}{2}\right\}^{1/2} x\right)\right] \tag{257}$$

These equations represent a highly damped dispersive wave. For $\sigma\mu\omega \gg l^2$ (l is the thickness of the conductor in the x direction), the field barely penetrates the conductor and the induced current responsible for the decay of the field also is concentrated near the surface. As $\sigma\mu\omega \to \infty$ the induced current becomes a surface current. For small $\sigma\mu\omega$ the magnetic field penetrates the conductor with little attenuation as does the induced current. The magnitude of the latter, however, is vanishingly small. For intermediate values of $\sigma\mu\omega$, a moderately strong current field is induced in the conductor which appreciably alters the magnetic field. The currents are generally not in phase with the magnetic field and are concentrated near the surface of the conductor. These general trends are also found to hold true for three-dimensional fields.

The fields, besides satisfying Equations 248, 249, 252, 253, must also satisfy the appropriate boundary conditions at the interface between different media. These may be found in any standard text (i.e. [5], p.17) and are

$$\hat{n} \times \left(\vec{E}_1 - \vec{E}_2\right) = 0 \tag{258}$$

$$\hat{n} \cdot \left(\sigma_1 \vec{E}_1 - \sigma_2 \vec{E}_2\right) = 0 \tag{259}$$

$$\hat{n} \times \left(\vec{H}_1 - \vec{H}_2\right) = \vec{K} \tag{260}$$

$$\hat{n} \cdot \left(\mu_1 \vec{H}_1 - \mu_2 \vec{H}_2\right) = 0 \tag{261}$$

$\hat{n}$ is the normal to the interface between medium 1 and 2. $\vec{K}$ is a surface current which can flow if either σ_1 or σ_2 is infinite. Note that $\vec{K}$ must be parallel to the interface surface at all points.

4.4 Electromagnetic Induction Modelling

As with magnetostatics and electrostatics, it is desirable to be able to calculate the response of an electomagnetic induction system to conducting bodies of arbitrary shapes. Unfortunately, the number of models which yield tractable solutions are small. For instance, for a dipole source such solutions can be found only for the sphere, the thin horizontal sheet, infinitely conductive half-plane, and the horizontally layered half-space. We will first choose one of these, the sphere, to illustrate the methodology. Afterwards, we will discuss methods which can solve arbitrary geometries with the use of a computer.

4.4.1 Simple Circuit Model

Before we begin, however, it is instructive to investigate an overly simplistic model. This model, although not very useful for analysing realistic situations, demonstrates most of the aspects of electromagnetic induction without obscuring results in the mathematics of electromagnetic theory. The geometry is shown in Fig. 4.7. The method follows Grant and West [4].

The electromagnetic induction system is assumed to consist of fixed separation transmit and receive circuits. The transmitter current is time-harmonic and both in-phase and quadrature receiver components are measured. The target is an isolated conductive circuit with lumped resistance, R, and inductance, L. If we label the transmitter circuit, "0", the target circuit,"1", and the receiver circuit, "2", then the mutual inductance between any two circuits i, j is denoted M_{ij} for $i, j = 0, 1, 2$. It should be noted that the difficult aspect from a field theory point of view is to calculate the M_{ij}.

Assume that the current in the transmit loop is $I_0 e^{i\omega t}$. Then the emf induced in the receiver by the primary field is

$$V_2^{(p)} = -i\omega M_{02} I_0 e^{i\omega t} \tag{262}$$

and the emf induced in the target circuit is

$$V_1 = -i\omega M_{01} I_0 e^{i\omega t} \tag{263}$$

The inductance of the loop generates a back emf and this plus V_1 plus the resistive drop must equal zero. Thus

$$V_1 + V_1' = V_1 - R I_1 e^{i\omega t} - i\omega L I_1 e^{i\omega t} = 0 \tag{264}$$

Some rearrangment yields the current in the target

$$I_1 e^{i\omega t} = -\frac{M_{01}}{L}\left[\frac{i\omega L\,(R - i\omega L)}{R^2 + \omega^2 L^2}\right] I_0 e^{i\omega t} \tag{265}$$

The emf induced in the receiver loop due to the secondary magnetic field generated by the current in the target loop is

$$V_2^{(s)} = -i\omega M_{12} I_1 e^{i\omega t} \tag{266}$$

We define the "response" as the ratio of secondary to primary voltages in the receiver loop. Using Equations 262, 265 and 266 and simplifying we get

$$G(\omega) = \frac{V_2^{(s)}(\omega)}{V_2^{(p)}(\omega)} = \beta\left[\frac{\alpha^2 + i\alpha}{1 + \alpha^2}\right] \tag{267}$$

where

$$\alpha = \omega L / R \tag{268}$$

and

$$\beta = -\frac{M_{01} M_{12}}{M_{02} L} \tag{269}$$

Studying Equation 267 further, we see that the coefficient β depends only on the relative size and positions of the circuits while the term in square brackets is a complex quantity which is a function of frequency and the electromagnetic properties of the target.

We call β the coupling coefficient. It can alternatively be expressed as

$$\beta = -\frac{k_{01} k_{12}}{k_{02}} \tag{270}$$

where

$$M_{ij} = k_{ij}\,(L_i L_j)^{1/2} \qquad j = 0, 1, 2 \tag{271}$$

and $|k_{ij}| \leq 1$. We see that each k_{ij} is the coupling coefficient for the corresponding circuit ij. Thus the coupling coefficient β measures the ratio of flux coupled into the receiver via the target to that which

directly couples to the receiver. Its value changes only with the position of the system. The complex function

$$F(\alpha) = \frac{\alpha^2 + i\alpha}{1 + \alpha^2} = X(\alpha) + iY(\alpha) \tag{272}$$

is called the "response function" and α is the "response parameter". Since inductance is related to loop diameter, the only loop parameters which affect the response function are resistance and size. The response function is shown in Fig. 4.8.

Note the limits of $F(\alpha)$. As $\alpha \to \infty$, $X(\alpha) \to 1$ and $Y(\alpha) \to 0$. This is referred to as the "inductive limit" and the response is given by

$$G_L = \beta \tag{273}$$

As $\alpha \to 0$, $F(\alpha) \to i\alpha$. This is the "resistive limit" and the response is

$$G_R = i\beta\alpha \tag{274}$$

Thus for low response parameter values, the response is small in amplitude and is in quadrature with the primary field. The amplitude increases, initially linearly, until the inductive limit is reached. The phase goes from 90^O at the resistive limit to 0^O at the inductive limit. The reasons for these qualitative trends are fairly simple to explain. When α is small, little current is induced in the target loop and the secondary field is much smaller everywhere than the primary. Since these two fields do not strongly interact, we can treat each induction process independently.[67] The secondary emf is shifted 180^O due to two induction processes whereas the primary emf is only shifted 90^O due to one. Thus the response for small $\omega L/R$ is small and in quadrature with the primary emf. As α increases, the secondary field induces an emf in the target loop which becomes comparable to that induced by the primary magnetic field. As Fig. 4.9 shows, the phase of the current in the target loop and thus the phase of the secondary field must shift so that the net induced emf balances the resistive loss. At the inductive limit, the emfs induced in the target loop by the primary and secondary fields become equal (see Equation 264). Thus the primary and secondary fields must be in phase but opposite in sign.

The inductive limit corresponds to $R \to 0$ or infinite conductivity. For a perfectly conductive object, the magnetic field cannot penetrate the surface of the medium. This happens because a secondary magnetic field is generated, equal and opposite to the primary field such that the total field is zero inside the object. In this simple circuit model, this occurs when the primary magnetic flux equals the secondary flux,[68] making the total flux through the circuit zero even though the total field at any point is not necessarily zero.

Next we investigate the coupling coefficient β further. The typical magnitude of the response of a horizontal loop system passing over a buried conductor is shown in Fig. 4.10. To illustrate that our simple model predicts such a response, we calculate β using flux diagrams, Fig 4.11 and 4.12, in which the loop directions are chosen such that k_{02} is positive. It is assumed that the transmitter/receiver separation is fixed so that k_{02} is constant. From Fig. 4.11 we see that when the loops straddle the target, β (see Equation 270) is negative and from Fig. 4.12, when the loops are to one side of the target, β is positive. When one loop is directly over the target, $\beta = 0$. Thus the response should look like Fig. 4.10 with each zero crossing corresponding to a position where one loop is directly over the target. The magnitude of β is larger for the negative portion of the response since the coupling is stronger when the loops straddle the target as opposed to being on one side of it. Also, the response is symmetrical about the target position, due to the fact that the coupling coefficient is independent of which loop carries current.

Finally, if we express the response, $G(\omega)$ (given by Equation 267), in the Laplace domain and obtain the inverse Laplace transform of $G(s)/s$, we obtain

$$g'(t) = L^{-1}\{G(s)/s\} = \frac{\beta}{\tau} e^{-t/\tau} \quad (t > 0) \tag{275}$$

where $\tau = L/R$. This is the response due to a unit step current and it is a single damped real exponential with time constant equal to that of the target loop.

[67] Put another way, the back emf in the target loop can be ignored.

[68] At the inductive limit $V_1' = -i\omega L I_1 e^{i\omega t}$. Substitution of this and Equation 263 in 264 yields $LI_1 + M_{01} I_0 = 0$.

The response characteristics of the simple circuit model are similar to the response characteristics of a number of more realistic models. The general shape of the response function is similar to Fig. 4.8, although the equations governing $F(\alpha)$ are more complicated than Equation 272. Generally there are an infinite number of poles in the response function rather than one and this manifests itself in a time response which is an infinite sum of damped exponentials rather than a single exponential. The coupling coefficient is, as mentioned, geometry dependent and must be examined separately for each particular model. However, for the horizontal geometry mentioned previously and a vertical conductor, the profile (response as a function of position) behaves in a manner similar to Fig. 4.10.

4.4.2 Response of a Sphere in the Field of a Coil

When we are dealing with a finite body, the complete electromagnetic theory is necessary. We will treat the case of a homogeneous sphere in the field of a loop as an example of such an analysis. The analysis has the advantage of being a realistic geometry for detection of nearby small objects while reducing in the limit to the commonly used uniform primary field or dipole source approximations.

We assume a spherical polar coordinate system (r, θ, ϕ) with origin at the sphere centre and will consider geometries with axial symmetry. The vector potential $\vec{A}$ is a solution of Equation 249 (Section 4.3) and with the assumption of axial symmetry must be of the form

$$\vec{A} = A(r, \theta)\hat{\phi} \tag{276}$$

where A is a scalar and $\hat{\phi}$ is the unit vector in the ϕ direction. We recall that the Laplacian operator acting on a vector can only be evaluated component by component in a cartesian coordinate system. Thus we write

$$\vec{A} = -A \sin\phi \hat{x} + A \cos\phi \hat{y} \tag{277}$$

where $\hat{x}, \hat{y}$ are the appropriate unit vectors. Operating on each cartesian component with ∇^2 and combining them yields, after some manipulation,

$$\nabla^2 \vec{A} = \left(\nabla^2 A - \frac{A}{r^2 \sin^2\theta}\right)\hat{\phi} \tag{278}$$

Equation 249 thus becomes a scalar linear 2nd order partial differential equation.

$$\nabla^2 A - \frac{A}{r^2 \sin^2\theta} - \sigma\mu\frac{\partial A}{\partial t} = 0 \tag{279}$$

As usual we solve this equation by separation of variables and assume time harmonic solutions. Thus

$$A(r, \theta, t) = R(r)\Theta(\theta)e^{i\omega t} \tag{280}$$

Substitution in Equation 279 leads to

$$(1 - u^2)\frac{d^2\Theta}{du^2} - 2u\frac{d\Theta}{du} - \left\{\frac{1}{1 - u^2} - n(n+1)\right\}\Theta = 0 \tag{281}$$

$$\frac{d^2R}{dr^2} + \frac{2}{r}\frac{dR}{dr} - \left\{k^2 + \frac{n(n+1)}{r^2}\right\}R = 0 \tag{282}$$

where $u = \cos\theta$, $k^2 = i\sigma\mu\omega$ and n is a separation constant.

Equation 281 is an associated Legendre equation with real solutions $P_n^1(u)$, $Q_n^1(u)$. Equation 282 is a modified Bessel equation with two solutions $r^{-1/2}I_{n+\frac{1}{2}}(kr)$ and $r^{-1/2}I_{-n-\frac{1}{2}}(kr)$ $(k \neq 0)$. If $k = 0$ (nonconductive region) Equation 282 reduces to

$$\frac{d}{dr}\left(r^2\frac{dR}{dr}\right) - n(n+1)R = 0 \tag{283}$$

and has the general solution $Cr^n + Dr^{-(n+1)}$ with C and D being constants. The general solutions of Equation 279 are then

$$A(r,\theta,t) = r^{-1/2}\left[CI_{n+\frac{1}{2}}(kr) + DI_{-n-\frac{1}{2}}(kr)\right]\left[EP_n^1(\cos\theta) + FQ_n^1(\cos\theta)\right] \tag{284}$$

for $k \neq 0$ and

$$A(r,\theta,t) = \left[Cr^n + Dr^{-(n+1)}\right]\left[EP_n^1(\cos\theta) + FQ_n^1(\cos\theta)\right] \tag{285}$$

for $k = 0$. We can now turn to the problem of the sphere in the field of a loop. The geometry is shown in Fig. 4.13.

The sphere of radius a, permeability μ, conductivity σ is placed in a nonconducting nonmagnetic medium at the centre of the spherical coordinate system (r,θ,ϕ). A circular loop of wire, radius R_T, is situated at (r_0,θ_0) and carries current $Ie^{i\omega t}$. It is coaxial with a sensing loop of radius R_S, situated at (r_S,θ_S). Both axes pass through the sphere centre.

The vector potential of the loop is calculated in the same manner as was done in Section 4.2.2. In the present case, however, the current density is given by

$$J_\phi = I\sin\theta'\delta(\cos\theta' - \cos\theta_0)\frac{\delta(r'-r_0)}{r_0} \tag{286}$$

Using the same analysis as before we find that the vector potential, $\vec{A}$, due to the primary loop current is:[69]

$$\vec{A}^{(p)} = \frac{\mu_0 I}{2}\left[\sum_{n=1}^{\infty}\frac{\sin\theta_0}{n(n+1)}\left(\frac{r}{r_0}\right)^n P_n^1(\cos\theta)\,P_n^1(\cos\theta_0)\right]\hat{\phi} \quad (r < r_0) \tag{287}$$

Inside the sphere the vector potential is from Equation 284 [70]

$$\vec{A}^{(i)} = r^{-1/2}\left[\sum_{n=1}^{\infty}A_n P_n^1(\cos\theta)\,I_{n+\frac{1}{2}}(kr)\right]\hat{\phi} \quad (r \leq a) \tag{288}$$

The secondary or anomalous potential due to the presence of the sphere is from Equation 285[71]

$$\vec{A}^{(s)} = \left[\sum_{n=1}^{\infty}E_n P_n^1(\cos\theta)\,r^{-(n+1)}\right]\hat{\phi} \quad (r \geq a) \tag{289}$$

The constants A_n, E_n are determined from the boundary conditions (Equations 258 - 261) of which Equations 258 and 260 may for the present problem be rewritten,

$$A^{(i)} = A^{(p)} + A^{(s)} \tag{290}$$

$$\frac{1}{\mu}\frac{\partial A^{(i)}}{\partial r} = \frac{1}{\mu_0}\left(\frac{\partial A^{(p)}}{\partial r} + \frac{\partial A^{(s)}}{\partial r}\right) \tag{291}$$

Substitution and simplification yield the anomalous or secondary potential due to the sphere

$$\vec{A}^{(s)} = \left\{\mu_0 I\sin\theta_0\sum_{n=1}^{\infty}\left[\frac{a^{2n+1}}{2n(n+1)r_0^n r^{n+1}}\chi_n(ka)P_n^1(\cos\theta)\,P_n^1(\cos\theta_0)\right]\right\}\hat{\phi} \tag{292}$$

where

$$\chi_n(ka) = \frac{[(n+1)\mu_r + n]\,I_{n+\frac{1}{2}}(ka) - kaI_{n-\frac{1}{2}}(ka)}{n(\mu_r - 1)\,I_{n+\frac{1}{2}}(ka) + kaI_{n-\frac{1}{2}}(ka)} \tag{293}$$

and as usual

$$\mu = \mu_r\mu_0$$
$$\mu_0 = 4\pi\times 10^{-7}\ \text{H/m} \tag{294}$$

Special Cases of Equation 292 :

[69] Time dependence is implicitly assumed to be $e^{i\omega t}$ and has been dropped in the following analysis.

[70] Note that Q_n^1 and $I_{-n-\frac{1}{2}}$ have been omitted since the former is singular for $\cos\theta = 1$ and the latter is singular for $r = 0$.

[71] Note that the r^n form of the solution has been dropped since it is singular at $r = \infty$.

1. **Dipole source** - If $d \gg R_T$ the field of the loop should become dipolar. By expanding $P_n^1(\cos\theta_0)$ as a power series in $(1-\cos\theta_0)$, it is easy to show that,

$$\vec{A}^{(s)}_{dipole} = \left[\frac{\mu_0 m_T}{4\pi}\sum_{n=1}^{\infty}\frac{r a^{2n+1}}{(r_0 r)^{n+2}}\chi_n(ka)P_n^1(\cos\theta)\right]\hat{\phi} \tag{295}$$

where

$$m_T = \pi R_T^2 I \tag{296}$$

is the dipole moment of the transmit loop.

2. **Homogeneous Primary Field** - If only the $n=1$ term dominates,[72] Equation 292) becomes

$$\vec{A}^{(s)}_{homog} = -\frac{\mu_0}{4\pi r^2}\sin\theta\, 2\pi a^3 H_0 \times$$

$$\left\{\frac{[\mu_0(1+k^2a^2)+2\mu]\sinh(ka) - (2\mu+\mu_0)\,ka\cosh(ka)}{[\mu_0(1+k^2a^2)-\mu]\sinh(ka) + (\mu-\mu_0)\,ka\cosh(ka)}\right\}\hat{\phi} \tag{297}$$

where

$$H_0 = \frac{I}{2}\frac{R_T^2}{r_0^3} \tag{298}$$

Note that the potential is that due to a dipole

$$\vec{m} = -2\pi a^3 H_0 (X + iY)\,\hat{z} \tag{299}$$

where $X+iY$ is the quantity in $\{\}$ in Equation 297.

It is instructive to examine the resistive and inductive limits for the case of the homogeneous primary field. By using series expansions for cosh, sinh, it can be shown that as $|ka| \to 0$,

$$m_R = \left[4\pi a^3\left(\frac{\mu-\mu_0}{\mu+2\mu_0}\right) - 2\pi a^3\left(\frac{i\sigma\mu_0\omega a^2}{15}\right)\left(\frac{3\mu}{\mu+2\mu_0}\right)\right]H_0 \tag{300}$$

which when $\mu = \mu_0$ reduces to

$$m_R|_{\mu_r=1} = -2\pi a^3\left(\frac{i\sigma\mu_0\omega a^2}{15}\right)H_0 \tag{301}$$

The first term of Equation 300 is due to the induced magnetization of the sphere and the second term is due to the induced eddy currents.

If $|ka| \to \infty$ then we get

$$m_L = -2\pi a^3 H_0 \tag{302}$$

Both Equations 300 and 302 can be obtained by means which do not involve boundary value methods. This provides some insight into the physical processes involved and is also very useful since often there is no closed form solution for many problems.

To obtain Equation 300 we assume initially $\mu_r = 1$. In the resistive limit, only the primary field contributes to the induction process. We divide the sphere into annular rings of radius $r\sin\theta$ and cross-sectional area $rd\theta dr$. The emf induced in each ring is

$$V = -i\omega\mu_0\pi r^2\sin^2\theta H_0 \tag{303}$$

We equate this to the resistive drop in the ring and get

$$d^2 I = -\frac{1}{2}i\sigma\mu_0\omega r^2\sin\theta dr d\theta H_0 \tag{304}$$

[72] This implies that $a \ll \left(R_T^2+d^2\right)^{1/2}$ or $a \ll \left(R_S^2+d^2\right)^{1/2}$.

The contribution to the dipole moment is

$$d^2 m_R = \pi (r \sin\theta)^2 \, d^2 I \tag{305}$$

Integrating Equation 305 we get 301, which is, of course, 300 with $\mu_r = 1$. To get 300 for $\mu_r \neq 1$ we replace $\mu_0 H_0$ with the actual flux density inside the sphere and then add a term to account for induced magnetization. Recall (Section 2.8) that if $\vec{M}$ is the magnetization of a sphere, $\vec{H_0}$ the external field and $\vec{H_i}$ the internal field, then

$$\vec{H_i} = \vec{H_0} - 1/3\vec{M} \tag{306}$$

But

$$\vec{M} = \frac{\mu - \mu_0}{\mu_0} \vec{H_i} \tag{307}$$

and so

$$\vec{B_i} = \mu \vec{H_i} = \left(\frac{3\mu_0}{\mu + 2\mu_0} \right) \mu \vec{H_0} \tag{308}$$

The dipole moment due to magnetization is

$$\vec{m} = \frac{4}{3} \pi a^3 \vec{M} \tag{309}$$

If we add Equation 309 to 301 and replace $\mu_0 H_0$ by $\vec{B_i}$ of Equation 308, we get the general resistive limit Equation 300 for any μ.

The inductive limit is obtained by finding the effective magnetization that makes the flux density vanish everywhere inside the sphere. We have

$$0 = \vec{B_i} = \mu_0 \left(\vec{H_i} + \vec{M_L} \right) = \mu_0 \left(\vec{H_0} + \frac{2}{3} \vec{M_L} \right) \tag{310}$$

or

$$\vec{M_L} = -\frac{3}{2} \vec{H_0} \tag{311}$$

Substituting $\vec{M_L}$ for $\vec{M}$ in Equation 309 yields 302.

Now let us examine the secondary potential of the sphere in the field of a loop (Equation 292) in more detail. First we note that it is the voltage induced in the receive loop that we measure rather than the vector potential. This is given by

$$V^{(s)} = i\omega \Phi^{(s)} = i\omega \oint \vec{A}^{(s)} \cdot \vec{dl} = 2\pi i \omega R_S \left(A_\phi^{(s)} \Big|_{\substack{r=R_S \\ \theta=\theta_S}} \right) \tag{312}$$

where the circular integral is performed around the receiver loop. In terms of distances rather than angles this becomes,

$$V^{(s)} = 2\pi i \mu_0 I \omega \frac{R_S R_T}{(d_T^2 + R_T^2)^{\frac{1}{2}}} \times$$

$$\sum_{n=1}^{\infty} \frac{a^{2n+1}}{2n(n+1)} \frac{P_n^1 \left(d_T / \left[d_T^2 + R_T^2 \right]^{\frac{1}{2}} \right) P_n^1 \left(d_S / \left[d_S^2 + R_S^2 \right]^{\frac{1}{2}} \right)}{(d_T^2 + R_T^2)^{\frac{n}{2}} (d_S^2 + R_S^2)^{\frac{n+1}{2}}} (X_n + iY_n) \tag{313}$$

where d_T is d for the transmit loop (see Fig. 4.13), d_S is d for the receive loop,

$$\chi_n(ka) = X_n(ka) + iY_n(ka)$$

and X_n, Y_n are real functions.

As in the simple loop target example, the expression $X_n(\omega) + iY_n(\omega)$ contains all the frequency dependence while the remainder of Equation 313 contains the geometry factors. The present response is far more complicated than that for the simple case because we now have a complicated sum of products of geometry and frequency dependent terms. The response parameter is now $\sigma\mu\omega a^2$ rather than $\omega L/R$.

Examining Equation 313 we see that the higher order terms decrease more rapidly with d than the lower order terms[73]. Thus if the sphere is far from the loop compared to its size (or much smaller than the loop diameter), the secondary voltage is that due to a sphere in a uniform field. In this case we recall that the secondary field is that of a simple magnetic dipole. As the loop approaches the sphere, higher order terms become significant and the secondary field of the sphere receives contributions from higher order multipoles.

The four lowest order multipole response functions are shown in Fig. 4.14. Note that the higher multipoles reach the inductive limit at higher values of $\sigma\mu\omega a^2$. This implies that the higher multipoles are more difficult to excite.

The time domain response may obtained in the same manner as for the loop target (Section 4.4.1). For a unit step primary current we find for $t > 0$,[74]

$$V^{(s)}(t) = \frac{2\pi R_T R_S I}{\sigma} \sum_{n=1}^{\infty} W_n\left(a, d_T, d_S, R_T, R_S\right) \sum_{m=1}^{\infty} A_{nm}\left(\mu_r\right) \exp\left[-\left(\frac{\delta_{nm}^2}{\mu\sigma a^2}\right) t\right] \tag{314}$$

where δ_{nm} are positive, real solutions of

$$n\left(\mu_r - 1\right) j_n\left(\delta_{nm}\right) + \delta_{nm} j_{n-1}\left(\delta_{nm}\right) = 0 \tag{315}$$

j_n are the spherical Bessel functions,

$$W_n = \frac{(2n+1)a^{2n-1} P_n^1\left(d_T / \left[d_T^2 + R_T^2\right]^{\frac{1}{2}}\right) P_n^1\left(d_S / \left[d_S^2 + R_S^2\right]^{\frac{1}{2}}\right)}{n(n+1)\left(d_T^2 + R_T^2\right)^{\frac{n+1}{2}} \left(d_S^2 + R_S^2\right)^{\frac{n+1}{2}}} \tag{316}$$

and

$$A_{nm} = \frac{\delta_{nm}^2}{n\mu_r\left(n\mu_r + 1\right) + \delta_{nm}^2 - n(n+1)} \tag{317}$$

A number of features are worth comparing with the simple loop target problem. First, Equation 314 is a sum of damped real exponentials as opposed to a single damped exponential as in Equation 275. For the simple loop target, the geometry or coupling was contained in the coefficient β, whereas for this case the geometry determines the coefficients R_T, R_S, W_n. For the simple loop target, information about the object size and shape was contained in the coefficient of time in the exponential. This is also true for the sphere in the field of a loop except that there are now an infinite number of coefficients, α_{nm},

$$\alpha_{nm} = \frac{\delta_{nm}^2}{\mu\sigma a^2} \tag{318}$$

In spite of the differences, however, we shall see that the sphere and simple loop target have time responses which appear quite similar, just as the frequency responses are similar.

It can be shown that for constant, n, the δ_{nm} increase as m increases (Table 4.1). Thus higher order terms for each multipole decay faster than the lower order. For $n = 1$, $\mu_r = 1$, we have the special case of a nonpermeable sphere in a homogeneous field, In this case

$$\left(V^{(s)}(t)\Big|_{\substack{\mu_r=1 \\ n=1}} = 3\pi I\left(\frac{a}{\sigma}\right) \frac{R_T^2 R_S^2}{\left(d_T^2 + R_T^2\right)^{\frac{3}{2}} \left(d_S^2 + R_S^2\right)^{\frac{3}{2}}} \cdot \right.$$

$$\sum_{m=1}^{\infty} \exp\left[-\left(\frac{m^2\pi^2}{\mu_0\sigma a^2}\right) t\right] \quad (t > 0) \tag{319}$$

and the initial amplitudes of all exponentials are the same (Fig. 4.15). This allows the time constants to be extracted, in principle.

For $n = 1$, $\mu_r \neq 1$, the initial amplitudes of the exponentials are initially small for $m = 1$ and increase slowly with m, asymptotically approaching the value of the nonpermeable amplitudes for large m (Fig.4.16). This makes extraction of the time constants by simple means impossible. We will return to the problem of extracting time constants later.

[73] This is easiest to see if we let $d = d_S = d_T$ i.e. the coplanar case

[74] A detailed derivation is found in[66].

4.4.3 Solution Using Impedance Boundary Conditions

One drawback to boundary value problems, such as the previous example, is that there are only a limited number of solvable geometries. Numerical methods would have a much broader range of applicability since many different geometries could be used as an input. If the object to be detected has sufficiently high conductivity so that impedance boundary conditions can be applied, then the response will depend only on surface properties of the object. It is well known that in the numerical solution of scattering problems, the surface integral equations are much simpler to handle than the volume integral equations. It can be shown ([5] p.338) that at the surface of a good but not perfect conductor, the magnetic field, $\vec{H}$, and electric field, $\vec{E}$, are related by the impedance boundary conditions

$$\vec{E} - \left(\hat{n} \cdot \vec{E}\right) \hat{n} = Z_S \left(\hat{n} \times \vec{H}\right) \tag{320}$$

where $\hat{n}$ is the unit normal to the surface and Z_S is the surface impedance of the conductor with electromagnetic parameters σ, μ, ϵ.

$$Z_S = Z_c = \left(\frac{i\omega\mu}{\sigma + i\omega\epsilon}\right)^{1/2} \tag{321}$$

where Z_c is the intrinsic impedance. This is strictly valid only if spatial variations of the fields orthogonal to the surface normal are small inside the conductor. For closed bodies this condition is true if

$$\left(\frac{\mu}{\mu_0}\frac{\sigma}{2\omega\epsilon_0}\right)^{1/2} k\rho \gg 1 \tag{322}$$

where all quantities are calculated inside the conductor, ρ is the smallest radius of curvature at the point on the surface and

$$k = \frac{2\pi}{\lambda} \tag{323}$$

is the propagation constant in free space. Equation 320 may be written as

$$\vec{M} = Z_S \left(\vec{J} \times \hat{n}\right) \tag{324}$$

where $\vec{M}$, $\vec{J}$ are the magnetic and electric surface currents which are generated.

$$\vec{M} = -\hat{n} \times \vec{E} \tag{325}$$

$$\vec{J} = \hat{n} \times \vec{H} \tag{326}$$

The general scattering geometry is shown in Fig.4.17. The incident (primary) electromagnetic fields $\vec{E}^i$, $\vec{H}^i$ induce currents on the surface, S, of an imperfectly conducting body such that the impedance boundary conditions on S are satisfied. The scattered fields at $\vec{r}$ due to the surface currents are given by ([3] pp.21-24)

$$\vec{E}^s = \frac{1}{i\omega\epsilon_0} \nabla \times \nabla \times \vec{A} - \nabla \times \vec{F} \tag{327}$$

$$\vec{H}^s = \frac{1}{i\omega\mu_0} \nabla \times \nabla \times \vec{F} + \nabla \times \vec{A} \tag{328}$$

where $\vec{A}$ and $\vec{F}$ are the magnetic and electric vector potentials or Schelkunoff potentials given by

$$\vec{A} = \int_S \vec{J}(r')\, G(r, r')\, ds \tag{329}$$

$$\vec{F} = \int_S \vec{M}(r')\, G(r, r')\, ds \tag{330}$$

where G is the free space Green's function,

$$G = \frac{1}{4\pi} \exp\left(-ik\left|\vec{r} - \vec{r}'\right|\right) / \left|\vec{r} - \vec{r}'\right| \tag{331}$$

Substitution of Equations 325,326,329, 330 into 327,328 and recognizing that $\vec{E}$, $\vec{H}$ in Equations 325,326 are the total fields given by $\vec{E}^i + \vec{E}^s$, $\vec{H}^i + \vec{H}^s$ respectively, we get two integral equations [67] :

$$\vec{J}(\vec{r}) = 2\hat{n}(\vec{r}) \times \vec{H}^i(\vec{r}) + 2\hat{n}(\vec{r}) \times \int_S \vec{J}\left(\vec{r'}\right) \times \nabla' G ds'$$

$$- 2\hat{n}(\vec{r}) \times \left[\int_S i\omega\epsilon_0 \vec{M}\left(\vec{r'}\right) G - \frac{1}{i\omega\mu_0} \nabla'_S \cdot \vec{M}\left(\vec{r'}\right) \nabla' G ds'\right] \tag{332}$$

and

$$\vec{E}^i(\vec{r}) = \frac{i\omega\mu_0}{4} \int_S \vec{J}\left(\vec{r'}\right) G ds' - \frac{1}{i\omega\epsilon_0} \int_S \nabla'_S \cdot \vec{J}\left(\vec{r'}\right) \nabla' G ds'$$

$$- \int_S \vec{M}\left(\vec{r'}\right) \times \nabla' G ds' \tag{333}$$

where ∇'_s is the tangential gradient with respect to $\vec{r'}$. The coupling between the Magnetic Field Integral Equation (332) and the Electric Field Integral Equation (333) is resolved by using the generalized impedance boundary condition,

$$\vec{M}\left(\vec{r'}\right) = \mathbf{Z_S}\left(\vec{r'}\right) \left[\vec{J}\left(\vec{r'}\right) \times \hat{n}\left(\vec{r'}\right)\right] \tag{334}$$

where now $\mathbf{Z_S}$ is a dyadic matrix (2 × 2) and $\vec{J}$ is the surface current (a 2-vector with components usually chosen along the directions of principle curvature). If we write,

$$\mathbf{Z_S}\left(\vec{r'}\right) = \begin{pmatrix} 0 & Z_1\left(\vec{r'}\right) \\ Z_2\left(\vec{r'}\right) & 0 \end{pmatrix} \tag{335}$$

then there are a number of approximations for the surface impedance. Two commonly used ones are:

1. $\mathbf{Z_S}$ constant everywhere on S (Leontowich approximation).

$$Z_1 = -Z_2 = Z_c \tag{336}$$

   This approximation is useful when Equation 322 is fully satisfied.

2. $\mathbf{Z_S}$ is curvature-dependent.

$$Z_1 = \left[1 - Q\left(\vec{r'}\right)\right] Z_c$$

$$Z_2 = \left[1 + Q\left(\vec{r'}\right)\right] Z_c$$

$$Q\left(\vec{r'}\right) = \frac{1}{4}(1 - i)\delta\left(K_u - K_v\right) \tag{337}$$

   where K_u, K_v are the principle curvatures at $\vec{r'}$ and $\hat{u}$, $\hat{v}$ are two orthonormal tangential vectors at $\vec{r'}$ for which $\hat{u} \times \hat{v} = \hat{n}$ is true. This is useful when the radius of curvature on some portions of the body approaches the electromagnetic wavelength.

Equations 332 - 334 using the appropriate approximation for $\mathbf{Z_S}$ may be solved by one of a number of numerical methods. One popular one is the Moment Method in which the integral equation is solved numerically by expanding the incident fields on the surface in a series of suitable basis functions, applying a set of testing functions and inverting the matrix of coefficients of the resulting set of simultaneous linear equations. There are a host of other numerical methods that may be used, but a full discussion is beyond the scope of this course. Further details may be found in [69].

4.5 Inverse Electromagnetic Induction Problems

The object of inverse electromagnetic induction problems is similar to that of Section 2.10 for the magnetostatic case, namely find the position (including depth), shape and size parameters of a hidden compact object of finite size.[75] As for the magnetostatic problem, we are faced with the problem of uniqueness. Although generally speaking, many sources may yield the same set of field values, often in practice the geometry is sufficiently well-known *a priori* or the sufficient information is available about the source (i.e, there are only a finite number of sizes and shapes) that the inverse problem is uniquely solvable. In any event, the success or failure of the inverse method, be it model fitting or pattern recognition, is essentially a test of uniquess.

There is, however, a notable difference between the magnetostatic and electromagnetic induction inverse problems. In the magnetostatic case, we saw that the permeability had little effect on the measured responses. For e. m. induction, the permeability can dramatically affect the response as can the conductivity.

We will restrict our discussion to the time domain, although most of the arguments related to localization apply to the frequency domain as well. Furthermore, we shall consider the detection of a buried sphere using a set of horizontal coils as in Fig.4.13. The time domain response is given by Equation 314, which is a sum of damped real exponentials. Compact bodies generally give such a response and so the following arguments will also be generally applicable to compact objects other than spheres.

Localization of the sphere in a horizontal plane is not as difficult as for localization of a magnetostatic dipole in a plane. The RMS secondary voltage induced in the receive coil as it moves over the object in a horizontal plane can be thought of as a spatial signature of the object. This signature is generally much narrower than the magnetostatic signature for the same geometry. This is because e.m. induction is an active detection method whose signal decreases very roughly as $\sim r^{-6}$, whereas magnetostatic detection is a passive method with a signal fall-off $\sim r^{-3}$. Furthermore, in e.m. induction, the primary field is vertical and hence the magnetic moment induced in the sphere is vertical. The effect of this is that the secondary voltage is a maximum when the sphere center is situated on the coil axis; i.e. when the sphere is directly under the coils. For non-spherical objects, the maximum secondary voltage still tends to occur when the object is under the coils, although the geometric center will not generally lie exactly on the coil axis. Typically, it is possible to localize an object in the horizontal plane to within one radius of the receive coil.

Depth determination is slightly more complicated. If we consider the geometry of Fig.4.13 and assume that the object is small enough w.r.t. the coils or far enough from them such that only the $n = 1$ term of Equation 314 contributes,[76] then we find that the ratio of voltages induced in 2 coplanar, coaxial receive coils of radius R_1 and R_2 at $t = t_i$ is

$$r_s = \frac{V_1(t_i)}{V_2(t_i)} = \frac{R_1^2\left(d^2 + R_2^2\right)^{3/2}}{R_2^2\left(d^2 + R_1^2\right)^{3/2}} \tag{338}$$

which assumes the same number of turns for each coil. We see that in this simple case, the voltage ratio is a function only of the depth, d, of the object and not of the object parameters (μ, σ, a). Inversion of Equation 338 by some method allows us a means of determining depth. It turns out that the assumption of a spherical object and uniform field are not that restrictive. Good results are obtained from the method even when the sphere depth is only 0.5 times the radius of the larger coil.[77] Situations, in which the object has dimensions similar to the coil diameter and its distance from the coil plane is less than a coil diameter, are typical of ordnance and archaeological artifact detection. The response for such geometries would be expected to have a relatively high contribution of higher order multipole fields. However, the good depth estimates that are obtained show that the contribution is small. In addition, good results are obtained for metallic spheroids with sizes similar to the spheres, independent of object orientation. Nor must the object's geometrical center lie on the coil axis. Good results are usually obtained for spheres if the object center is displaced horizontally from the coil axis by up to a fraction (typically $\sim 1/2$) of a coil

[75] Since we are dealing with compact objects, we exclude from this discussion geophysical problems related to detection of semi-infinite media such as layered half-spaces or vertical dykes. These are most often analysed by a modelling approach.

[76] i.e. the primary field is uniform

[77] This assumes $R_1 = 2R_2$, $0.3R_2 \leq a \leq 0.8R_2$.

radius. If the center is off-axis, the depth, d, determined from Equation 338 approximates $\left(d_0^2 + x^2\right)^{1/2}$ where d_0 is the true vertical depth and x is the horizontal displacement of the object center from the axis. A more detailed discussion of this method is found in [74]. Experiments must still be done to verify if the method is applicable to objects other than spheroids, for similar geometries.

Assuming we now know the location of the object, we are left with the problem of identification, namely determining size, shape and material properties (μ, σ). As for magnetostatic detection, there are two general methods: model fitting and pattern classification.

Model fitting includes least squares fitting and Prony's method [78]. Of course, model fitting relies strongly on there being an applicable model and this is what often limits its use. For a sphere, the secondary voltage can be fitted to the function

$$V'(t) = \sum_{n=1}^{\infty} W_n(a) \sum_{m=1}^{\infty} A_{nm} \exp\left\{-\left(\frac{K_{nm}}{\sigma a^2}\right) t\right\} \tag{339}$$

by a nonlinear method with a, σ being the free parameters. Of course A_{nm}, K_{nm} are functions of μ but for nonpermeable objects they are one set of constants and for $\mu_r \sim 100$ or greater, they are another set of constants.[78] For nonpermeable objects only a few terms are usually needed in the summation but for permeable objects, hundreds of terms are needed to approximate $V^{(s)}$ accurately. There are also the standard problems of nonconvergence and need for initial parameter estimates which all nonlinear fitting methods have in common. Most importantly, of course, the model applies only to a sphere.

However, it is found that compact conductive objects generally produce a secondary voltage of the form

$$V'(t) = \sum_{n=1}^{\infty} A_n e^{-\alpha_n t} \tag{340}$$

and thus a nonlinear fit of the secondary voltage using a truncated series like that of Equation 340 ($n = 1, 2, \ldots N$) would yield coefficients $\hat{A}_n$, $\hat{\alpha_n}$ which would presumably be functions of the size, shape, σ, μ (and unfortunately the orientation, as well) of the object. The problem in such an approach turns out to be the fact that real damped exponentials are highly correlated functions. Thus the estimates $\hat{A}_n$, $\hat{\alpha_n}$ are strongly dependant on the number of terms (N) used in the model.

Another technique that has been used with some degree of success in underwater acoustics and electromagnetics is Prony's method. In those applications, the waveforms involved are a sum of damped complex exponentials. Prony's method is basically a nonlinear fitting procedure where the nonlinearity of the system is concentrated in a single polynomial and thus most of the above comments about nonlinear fitting apply. One advantage, however, is that an initial guess of the parameters is not required. As with regular nonlinear fitting, the number of exponentials in the model has a very strong effect on the parameter extimates obtained. A further disadvantage is that the estimation procedure is sensitive to the sampling interval chosen and very sensitive to the S/N ratio.

One might be tempted to try a simpler approach which is often used in nuclear physics. The tail of the waveform is fitted to a single exponential, with the assumption being made that the faster decaying terms are negligable at sufficiently great times. The smallest time constant, $\hat{\alpha_1}$, is obtained and the estimated term $\hat{A}_1 e^{-\hat{\alpha_1} t}$ is subtracted from the waveform to obtain a reduced waveform. The tail of the reduced waveform is fitted to a single exponential and the process is repeated. This method might, in fact, work reasonably well for nonpermeable spheres in which only a single exponential is significant for large times (Fig. 4.15). For permeable spheres, several exponentials contribute at any time (Fig. 4.16) and the method will fail.[79] In general, objects of arbitrary shape do not have waveforms like Fig. 4.15.

Even if fitting the waveforms to a sum of damped real exponentials did yield accurate coefficients, relating those coefficients to the properties of the target object would be a formidable task without *a priori* knowledge of the object's shape classification (i.e. spheroid, cylinder, hollow, solid, etc.). Indeed, even this knowledge would allow an analytical solution for the object's parameters in only the few cases such as the sphere or spheroid for which analytical models exist.

[78] In all the previous modelling, it has been assumed that μ_r is constant, although μ is obviously governed by some hysteresis curve. However, in the earth's field μ_r is typically between 100 and 1000 for ferrous objects and hence the effect is as though μ_r were constant (see Table 4.1).

[79] Because of the correlated nature of real exponentials, one can always fit the tail to a single exponential. However, the estimated coefficient could not be simply related to μ, σ, a.

If the number of objects under consideration is finite, we may consider pattern recognition. A method which has been successfully used to classify metallic spheroids [79] will be described as an example. As previously stated, once we have localized the object, the coil axes are approximately over its geometric center. Referring to Fig. 4.13, where now the spherical object is replaced by an arbitrary object with axial symmetry, it is obvious that the response will be independent of the azimuthal angle of the symmetry axis of the object.

Feature vectors are obtained from the electromagnetic induction response by one of a variety of schemes. This usually consists of first normalizing the time response relative to a fixed time after the falling edge of the transmitter pulse; segmenting the normalized response and fitting each of the finite number of segments to a simple function such as a straight line, single exponential or a constant. The segments do not have to be equal time intervals but may be adjusted for constant energy (area). There are advantages and disadvantages for each feature type which are beyond the scope of this course (see [79] for a discussion). A simple, but quite successful choice [79] has been the mean response for each segment with equal time intervals. A feature vector for a response then consists of the sequence of fit parameters for all segments.

We can use a continuous parameter classifier very similar to that of Section 2.10, except that now the manifold is a function of only one continuous parameter θ, the polar angle of the object's symmetry axis. Hence, the class prototype for an object is a one dimensional manifold (i.e., a curve) in an N dimensional feature space.[80] An example is shown in Fig.4.18 for an $N = 2$ dimensional feature space.

The approach is to approximate the curve by a sequence of line segments which connect points on the curve. This reduces the problem to finding the minimum distance from the test vector to a sequence of line segments.

The prototype for class i and given θ is a point defined by the head of a vector denoted $|m_i(\theta)\rangle$. The prototype is approximated by a finite number of line segments joining points $|m_{i,j}\rangle$ where the subscript j indicates that the prototype feature vector is evaluated at the discrete value of the parameter $\theta = \theta_j$. We define a unit vector $|\alpha_{i,j}\rangle$ along the line segment joining $|m_{i,j}\rangle$ and $|m_{i,j+1}\rangle$,

$$|\alpha_{i,j}\rangle = |u_{i,j}\rangle \,/\, \langle u_{i,j}|\, u_{i,j}\rangle^{\frac{1}{2}} \tag{341}$$

where

$$|u_{i,j}\rangle = |m_{i,j+1}\rangle - |m_{i,j}\rangle\,. \tag{342}$$

Let $|x\rangle$ be a test vector and define

$$|y_{i,j}\rangle = |x\rangle - |m_{i,j}\rangle\,. \tag{343}$$

If we define $\left|y_{i,j}^{(s)}\right\rangle$ to be the projection of $|y_{i,j}\rangle$ onto the line segment, and $|d_{i,j}\rangle$ to be the vector which is normal to the line segment and which passes through $|x\rangle$, then

$$|d_{i,j}\rangle = |y_{i,j}\rangle - \left|y_{i,j}^{(s)}\right\rangle \tag{344}$$

$$\left|y_{i,j}^{(s)}\right\rangle = \langle y_{i,j}|\, \alpha_{i,j}\rangle\, |\alpha_{i,j}\rangle = q_{i,j}\, |u_{i,j}\rangle \tag{345}$$

where

$$q_{i,j} = \frac{\langle y_{i,j}|\, u_{i,j}\rangle}{\langle u_{i,j}|\, u_{i,j}\rangle}. \tag{346}$$

If $|x\rangle$ is a sample from the class i corresponding to the region of the prototype curve for which $\theta_j \le \theta \le \theta_{j+1}$, then an estimate, $\hat{\theta}$, of the continuous parameter associated with $|x\rangle$ may be obtained from

$$\hat{\theta} = \theta_j + q_{i,j}\,(\theta_{j+1} - \theta_j) \tag{347}$$

[80] $N \approx 12$ is typical.

The minimum distance, $d_{i,j}$, from the test vector to the region of the curve between $|m_{i,j}\rangle$ and $|m_{i,j+1}\rangle$ is approximated by

$$d_{i,j} = \langle d_{i,j} | \, d_{i,j} \rangle^{\frac{1}{2}} \tag{348}$$

Since the line segment only approximates the manifold between the two endpoints of the line segment, the previous distance equations are really only true provided $\left| y_{i,j}^{(s)} \right\rangle$ lies between these points. Examination of Equations 345 and 346 reveals that this occurs for $0 \leq q_{i,j} \leq 1$. If this condition is not satisfied then $d_{i,j}$ is replaced by the distance from the test vector to the nearest endpoint of the segment. For speed of implementation, $q_{i,j}$ is calculated first and based on its value, the appropriate calculation of $d_{i,j}$ is carried out.
Finally, the minimum distance, d_i, from the test vector to the curve is approximated by

$$d_i = \min_j \{d_{i,j}\} . \tag{349}$$

The test vector is assigned to the class i for which d_i is a minimum.

Probability of correct classification for a restricted case (responses of a set of four steel spheroids obtained in a nonmetallic laboratory) are between 90% and 97%. One problem is that the responses vary slowly with depth and hence to improve classification success, the design set must include various depths or else a correction for depth must be applied to each response. The former would then require the use of a two dimensional continuous parameter classifier such as was used in Section 2.10. The student should consult [79] for more details.

5 Conclusion

The detection of compact objects by low frequency electromagnetics has been discussed. In particular, magnetostatic, electrostatic and electromagnetic induction techniques have been described with an emphasis on locating and identifying objects rather than merely detecting them.

Although the techniques for compact object detection are broadly related to their counterpart geoexploration methods, it must be remembered that the two problems are quite different and methods cannot be directly carried from one problem to the other. Sources and geometries are usually radically different for both problems and consequently detectors and signal processing techniques are also different. Geoexploration techniques are covered in a number of standard textbooks.

Finally, it is sometimes stated that low frequency electromagnetic detection of compact objects is a "mature science". I hope that by the time this part of the text is reached, it will be clear to the reader that there is still much fundamental research to be done before objects can be reliably located and identified.

References

LOW FREQUENCY ELECTROMAGNETIC REMOTE SENSING

GENERAL

Geo-electromagnetic Theory

[1] -, *IEEE Trans GeoSci. and Remote Sens. Special Issue on Electromagnetic Methods in Applied Geophysics GE-22*, pp.3-90, 1984.

[2] J.R.Wait, *Geo-Electromagnetism.* New York:Academic Press, 1982.

[3] -, *Mining Geophysics Volume 2 - Theory.* Tulsa Oklahoma: The Society of Exploration Geophysicists, 1967.

[4] F.Grant and G.West, *Interpretation Theory in Applied Geophysics.* New York:McGraw-Hill, 1965.

Electromagnetic Theory

[5] J.Jackson, *Classical Electrodynamics.* New York:Wiley, 1975.

[6] W.Panofsky and M.Phillips, *Classical Electricity and Magnetism.* Reading, Mass.: Addison-Wesley, 1962.

[7] W.Smythe, *Static and Dynamic Electricity Third Edition*, New York: McGraw-Hill, 1968.

[8] J.Stratton, *Electromagnetic Theory*, New York:McGraw-Hill, 1941.

Mathematical Techniques

[9] G.Arfken, *Mathematical Methods for Physicists*, New York: Academic Press, 1970.

[10] M.Abramowitz and I.Stegun, Eds., *Handbook of Mathematical Functions*, New York: Dover, 1965.

[11] O.C.Zienkiewicz, *The Finite Element Method in Engineering Science*, London: McGraw-Hill, 1971.

[12] M.Chari and P.Silvester , Eds., *Finite Elements in Electrical and Magnetic Field Problems*, New York: Wiley, 1980.

[13] J.Tou and R.Gonzalez, *Pattern Recognition Principles.* Reading, Mass.: Addison Wesley, 1974.

[14] J.W.Sammon Jr., "Interactive pattern analysis and classification", *IEEE Trans. Computers*, vol. C-19, p.594, 1970.

[15] J.R.Rice, "Experiments on Gram-Schmidt orthonormalization", *Math. Comp.*, vol.29, p.325, 1966.

Remote Sensing

[16] R.N.Colwell, Editor-in-Chief, *Manual of Remote Sensing, Second Edition, Volumes 1 and 2.* Falls Church Va.: American Society of Photogrammetry, 1983.

MAGNETOSTATIC METHODS

General Magnetism

[17] R.Bozworth, *Ferromagnetism.* New York:Van Nostrand, 1951.

[18] G.Garland, *Introduction to Geophysics.* Toronto: W.B.Saunders, 1971 (Chapters 15 - 21).

Theory

[19] J.Simkin, C.Trowbridge, "Three-dimensional nonlinear electromagnetic field computations using scalar potentials", *IEE Proc 127B*, pp.368-374, 1980.

Applications

[20] J.Scarzello and G.Usher, "A low power magnetometer for vehicle detection",*IEEE Trans Mag, MAG-13*, pp. 1101-3, 1977.

[21] G.Ioannidis, "Identification of a ship or submarine from its magnetic signature",*IEEE Trans AES, AES-13*, pp.327-329, 1977.

[22] J.McFee and Y.Das, "The detection of buried explosive objects", *C.J.Remote Sensing 6*, pp.104-121, 1980.

[23] J.E.McFee and Y.Das, "Development of an intelligent system to locate and identify ferrous objects", *Proc. IMACS International Symposium on AI, Expert Systems and Languages in Modelling and Simulation*, Institute for Cybernetics, Barcelona, Spain, p.203, Jun.4-6, 1987.

[24] D.Cohen, "Developments in ways to measure the extremely weak magnetic fields emanating from organs...", *Physics Today*, pp.35-43, August 1975.

[25] S.Breiner, *Applications Manual for Portable Magnetometers*, Sunnyvale California: GeoMetrics Ltd., 1973.

Inverse Methods

[26] T.Caffey and L.Romero, "Locating a buried dipole", *IEEE Trans Geoscience and Remote Sensing, GE-20*, pp.188-192, 1982.

[27] A.McAulay, "Computerized model demonstrating magnetic submarine localization",*IEEE Trans AES, AES-13*, pp.246-254, 1977.

[28] F.Raab, E.Blood,T.Steiner and H.Jones, "Magnetic position and orientation tracking system", *IEEE Trans AES, AES-15*, pp.709-717, 1979.

[29] W.Wynn, C.Frahm, P.Carroll, R.Clark, J. Wellhoner and M. Wynn, "Advanced superconducting gradiometer/magnetometer arrays and a novel signal processing technique", *IEEE Trans Mag, MAG-11*, pp. 701-707, 1975.

[30] J.McFee and Y.Das, "Determination of the parameters of a dipole by measurement of its magnetic field",*IEEE Trans AP, AP-29*, pp.282-287, 1981.

[31] J.McFee and Y.Das, "Fast nonrecursive method for estimating location and dipole moment components of a magnetic dipole", *IEEE Trans GeoScience and Remote Sensing, GE-24*, p.663, 1986.

[32] J.E.McFee and Y.Das, "A classifier for feature vectors whose prototypes are a function of multiple continuous parameters", *IEEE Trans. PAMI*, 1988.

Measurement Facilities

[33] J.McFee, M.Bell, B.Dempsey, R.Chesney and Y.Das, "A magnetostatic signature measurement and analysis system", *J.Phys.E., 18*, pp.54-60, 1985.

[34] A.L.Bloom, "Optical pumping", *Scientific American*, pp.72-80, 1960.

[35] P.Grivet and L.Malnar, "Measurement of weak magnetic fields by magnetic resonance", *Advances in Electronics and Electron Physics, 23*, pp.39-151, 1967.

[36] F.Primdahl, "The fluxgate magnetometer", *J.Phys.E.:Sci.Instrum, 12*, pp.241-253, 1979.

[37] F.Acker, "Calculation of the signal voltage induced in a toroidal proton precession magnetometer sensor", *IEEE Trans Geoscience Electronics, GE-9*, pp.98-103, 1971.

[38] T.Casselman, "Calculation of the performance of a magnetorestrictive permalloy magnetic field sensor", *IEEE Trans Magnetics, MAG-16*, pp.461-464, 1980.

[39] J.Clarke, "Low- frequency applications of superconducting quantum interference devices", *Proc.IEEE 61*, pp.8-19, 1973. stable r.f. biased superconducting point - contact quantum devices", *J.Appl.Phys. 41*, p.1572, 1970.

[40] A.Yariv and H.Winsor, "Proposal for detection of magnetic fields through magnetorestrictive perturbation of optical fibers", *Optics Letters, 5*, pp.87-89, 1980.

ELECTROSTATIC METHODS

General

[41] L.Slichter and M.Telkes, "Electrical properties of rocks and minerals", *Handbook of Physical Constants, Geological Society of America Special Paper*, F.Birch, Ed., pp.299-319, 1942.

[42] E.Parkhomenko, *Electrical Properties of Rocks*. New York: Plenum, 1967.

[43] M.J.Campbell and J.Ulrichs, "Electrical properties of rocks and their significance for lunar radar observations", *J.Geophys.Res. 74*, pp. 5867- 5881, 1969.

[44] D.Jupp and K.Vozoff, "Stable Iterative Methods for the Inversion of Geophysical Data", *Geophys. J. R. Astr.Soc. 42*, pp.957 - 976, 1975.

Conductivity Methods

[45] C.V.Keller and F.C.Frischknecht, *Electrical Methods in Geophysical Prospecting*. Oxford: Pergamon, 1966.

[46] G.Kunetz, *Principles of Direct Current Resistivity Prospecting*. Berlin: Gebruder Borntrager, 1966.

Conductivity Imaging

[47] R.Henderson and J.Webster, "An impedance camera for spatially specific measurements of the thorax", *IEEE Trans.Bio.Eng. BME-25*, pp.250-254, 1978.

[48] R.J.Lytle and K.A.Dines, "An impedance camera: A system for determining the spatial variation of electrical conductivity", *Report UCRL-52413*, Lawrence Livermore Laboratory, Livermore, California, 1978.

[49] K.A.Dines and R.J.Lytle, "Computerized geophysical tomography", *Proc.IEEE 67*, p.1065, 1979.

[50] K.A.Dines and R.J.Lytle, "Analysis of electrical conductivity imaging", *Geophysics 46*, pp. 1025-1036, 1981.

[51] L.R.Price, "Electrical impedance computed tomography (ICT): A new imaging technique", *IEEE Trans.Nuc.Sci. NS-26*, pp.2736-2739, 1979.

[52] R.Bates, G.McKinnon and A.Seager, "A limitation on systems for imaging electrical conductivity distributions", *IEEE Trans.Bio.Eng. BME-27*, pp.418-420, 1980.

[53] R.Nakonechny, "A Preconditioned Conjugate Gradient Method Using a Sparse Linked-List Technique for the Solution of Field Problems", *M.Sc. Thesis, Technical Report TR83-3*, University of Manitoba, 1983.

[54] A.Wexler,B.Fry and M.Neuman, "An impedance computed tomography algorithm and system", *Proc. Optical Society of America meeting on Industrial Applications of Computed Tomography and NMR Imaging*, Hecla Island, Manitoba, Canada, August 1984.

[55] A.Wexler and C.J.Mandel, "An impedance computed tomography algorithm and system for ground water and hazardous waste imaging", *Proceedings of the Second Canadian/American Conference on Hydrogeology*, Banff Alberta June 25-29 1985. (pub. National Water Well Assoc., Dublin OH)

[56] A.Tamburi,R.Allard and U.Roeper, "Tomographic imaging of ground water pollution plumes", *Proceedings of the Second Canadian/American Conference on Hydrogeology*, Banff Alberta June 25-29 1985. (pub. National Water Well Assoc., Dublin OH)

Induced Polarization

[57] J.S.Sumner, *Principles of Induced Polarization for Geophysical Exploration.* Amsterdam: Elsevier, 1976.

[58] -, *Advances in Induced Polarization and Complex Resistivity (short course).* Tucson: University of Arizona, 1981.

[59] A.Howland-Rose, G.Linford, D.Pitcher and H.Seigel, "Some recent magnetic polarization developments - Part 1:theory", *Geophysics 45*, pp.37- 54, 1980.

ELECTROMAGNETIC INDUCTION

General

[60] D.F.Bleil, Ed., *Natural Electromagnetic Phenomena Below 30 KC/S*, New York: Plenum, 1964.

[61] J.E.Hipp, "Soil electromagnetic parameters as functions of frequency, soil density and soil moisture", *Proc.IEEE 62*, p.98, 1974.

Electromagnetic Induction Theory

[62] J.R.Wait and K.P.Spies, "Quasi-static transient response of a conducting permeable sphere", *Geophysics 35*, pp.789- 792, 1969.

[63] M.N.Nabighian, " Quasi-static transient response of a conducting permeable sphere in a dipolar field", *Geophysics 35*, pp.303- 309, 1970.

[64] S.K.Singh, "Electromagnetic transient response of a conducting sphere embedded in a conducting medium", *Geophysics 38*, pp.864- 893, 1973.

[65] J.R.Wait, "A conducting permeable sphere in the presence of a coil carrying an oscillating current", *Can. J. Phys. 31*, pp. 670- 678, 1953.

[66] Y.Das,J.E.McFee and R.H.Chesney, "Time domain response of a sphere in the field of a coil-theory and experiment", *IEEE Trans GeoScience and Remote Sensing GE-22*,p.360, 1984.

[67] K.M.Mitzner, "An integral equation approach to scattering from a body of finite conductivity", *Rad.Sci. V2*, 1967.

[68] T.B.A. Senior, "Impedance boundary condition for imperfectly conducting surfaces", *App.Sci.Res. 8B*, 1961.

[69] A.A.Sebak and L.Shafai, "Transient response computation of spheroidal objects using impedance boundary conditions",*IEEE Trans AP AP-32*, p.1116, 1984.

Applications

[70] J.R.Wait, "Review of electromagnetic methods in nondestructive testing of wire ropes", *Proc.IEEE. 67*,pp.892- 903, 1979.

[71] R.Callarotti and M.Alfonzo, "Measurement of the conductivity of metallic cylinders by means of an inductive method", *J. Appl. ,Phys. 43*, pp. 3040-3047, 1972.

[72] C.Colani and M.Aitken, "A new type of locating device. The instrument", *Prozspezioni Archeologiche*, pp.15-23, 1966.

[73] E.B.Glennie, "Inductive detection of buried services", *Proc.IEE 125*, pp.14-15, 1978.

Inverse Methods

[74] Y.Das, J.E.McFee and R.H.Chesney, "Determination of depth of shallowly buried objects by electromagnetic induction",*IEEE Trans GeoScience and Remote Sensing GE-23*, p.60, 1985.

[75] S.H.Ward, "Unique determination of conductivity, susceptibility, size and depth in multifrequency electromagnetic exploration", *Geophysics 24*, p.531, 1959.

[76] W.H.Huggins, "Representation and analysis of signals part 1, the use of orthogonalized exponentials", *Department of Electrical Engineering Report, Johns Hopkins University*, 1957.

[77] R.N.McDonough, "Matched exponents for the representation of signals", *Ph.D.Thesis Johns Hopkins University*, 1963.

[78] Y.Das,J.E.McFee and M.Bell, "Detection and identification of buried ordance by magnetic and electromagnetic means (U)", *Suffield Report 283* 1981, UNCLASSIFIED.

[79] R.H.Chesney, Y.Das, J.E.McFee and M.Ito, "Identification of metallic spheroids by classification of their electromagnetic responses", *IEEE Trans PAMI PAMI-6*,p.809, 1984.

Instruments and Facilities

[80] B.Roston, "Development of locators of small metallic bodies buried in the ground", *J. of the IEE 95*, pp.653- 667, 1948.

[81] R.Macario, "Discriminative metal detector", *Wireless World*, pp.43-46, July 1978.

[82] J.Corbyn, "Pulse induction metal detector", *Wireless World*, pp.40-44, March 1980.

[83] J.Corbyn, "Pulse induction metal detector - 2", *Wireless World*, pp.58-59, April 1980.

[84] J.E.McFee, R.H.Chesney, Y.Das, J.Toews, M.Turnbull, R.Pinnell, and M.Bell, "An experimental time domain electromagnetic induction system",*Rev. Sci. Instrum 55*, p.968, 1984.

[85] Y.Das, J.Toews and J.E.McFee, "Vehicle-mounted ordnance locator : an experimental prototype (U)", *Suffield Report 434*, 1988, UNCLASSIFIED.

Table 1.1

MAIN CHARACTERISTICS OF EXPLOSIVE MUNITIONS

CHARACTERISTIC	UXO	LANDMINE	IED
Number of shapes	Many	Few	Many
Types of shapes	Prolate Spheroid/ cone on cylinder	Oblate spheroid/ squat cylinder	Various
Size	Many	Few	Many
Background clutter	Heavy: only 1 – 10% of metal mass is UXO	Moderate: explosive vapours/ Sparse: metal	Sparse-moderate: depends on scenario/detector
Typical depth	0 to 2 meters	< 0.3 meter	Varies
Case materials	Metallic, mostly ferrous	Metal, plastic, wood, none	Metal, plastic, wood, none
Chief detection problems	1. Need location, depth est. 2. Need size/shape discrimination	1. Need to detect explosive for nonmetallic mines	1. Need to detect explosive due to lack of consistency

UNCLASSIFIED

Table 1.2

METHODS FOR DETECTING EXPLOSIVE MUNITIONS

METHOD	REMOTE/ QUASI-REMOTE
Magnetostatics	Q
Electromagnetic Induction	Q
Conductivity Imaging	Q
Ground Penetrating Radar	Q
Acoustics	Q
RF Resonance Absorption	Q
Nuclear	Q
Trace Gas Analysis	Q
Biochemical Detection	Q
Optical – Ultraviolet	Q, R
Optical – Visible	R
Optical – Infrared – Near	R
Optical – Infrared – Thermal	Q, R
Microwaves – Passive	Q, R
Microwaves – Active	Q, R
Human Perception Channels	?

Table 1.3

ELECTRICAL PROPERTIES OF TWO COMMON MATERIALS IN REMOTE SENSING

MATERIAL	CONDUCTIVITY S/m	FREQUENCY Hz	SKIN DEPTH m
SALINE	10^{1}	1000	0.16
		100	0.50
		10	0.16
SOIL (MAXIMUM CONDUCTIVITY)	10^{-1}	1000	1.6
		100	5.0
		10	16.

Table 2.1

STANDARD NOMENCLATURE OF GEOMAGNETIC FIELD COMPONENTS

Component	Standard letter symbol	Average value near latitude 45°N (nT)
Total field	F	45000
Horizontal component	H	15000-25000
Vertical component	Z	40000
Declination (angle between H and the geographical north direction)	D	Depends on location
Inclination or dip (angle between F and the horizontal plane)	I	60-70° (F pointing down)

Table 2.2

MAGNETIC UNITS

Quantity	Typical Symbol	Units
Magnetic Induction or Magnetic Flux Density	$\vec{b}$, $\vec{B}$	**1 nanoTesla** (nT) $= 10^{-9}$ **Tesla** (Weber/m^2) $= 10^{-5}$ Gauss $= 1$ gamma (γ)
Magnetic Field or Magnetic Field Intensity	$\vec{h}$, $\vec{H}$	1 nT/μ_0 $= 10^{-5}$ Oersteds (Gilberts/cm) $= 7.96 \times 10^{-4}$ **A/m** $= 7.96 \times 10^{-7}$ emu
Magnetization	$\vec{M}'$	same as $\vec{H}$
Magnetic Dipole Moment	$\vec{m}$, $\vec{M}$, $\vec{M}^{(1)}$	**1 A·m^2** $= 10^3$emu

Table 2.3

COMPARISON OF SOME PROPERTIES OF Q AND B_3 IN A HORIZONTAL MEASUREMENT PLANE (See Figure 2.13)

Property	Q	B_3
Number of extrema	1	2 or 3
Type of extrema	maximum	1 maximum, 1 minimum 1 saddle point (except for horizontal dipole)
Position in plane of maximum	$0 \leq x_1 \leq 0.15x_3,\ x_2 = 0$	$0 \leq x_1 \leq 0.5x_3,\ x_2 = 0$
Position in plane of minimum	n/a	$-2x_3 \leq x_1 \leq -0.5x_3,\ x_2 = 0$
Radius of half maximum field (vertical dipole only)	$0.4x_3$	$0.5x_3$
Symmetry	$Q(x_2) = Q(-x_2)$	$B_3(x_2) = B_3(-x_2)$
Determination of position in plane	location is almost directly under field maximum	extensive computation required
Determination of depth and dipole moment	not straightforward from simple measurements	comes from same computation as for position in plane

Table 2.4

DIMENSIONS OF SPHEROIDAL OBJECTS FOR CLASSIFICATION EXPERIMENTS

OBJECT NUMBER	LENGTH OF SYMMETRY AXIS (a) IN M	RATIO OF AXES LENGTHS (e)
1	0.010	3.75
2	0.020	3.40
3	0.030	2.50
4	0.045	2.50
5	0.060	3.50
6	0.090	3.50

Table 2.5

PROBABILITY OF MISCLASSIFICATION FOR SPHEROIDS OF TABLE 2.4

PERCENT NOISE	PROBABILITY OF MISCLASSIFICATION (%)	PERCENT NOISE	PROBABILITY OF MISCLASSIFICATION (%)
0	1.1	10	7.1
1	1.1	25	16.4
2	1.4	50	30.3
5	2.9	75	39.0

Table 3.1

ELECTROMAGNETIC PROPERTIES OF RELEVANT MATERIALS

Material	Dielectric Constant	Conductivity (S/m)	Relative Permeability
A.Soils			
dry sand	$4 \rightarrow 6$	$10^{-7} \rightarrow 10^{-3}$	1
water saturated sand	30	$10^{-4} \rightarrow 10^{-2}$	1
water saturated silt	10	$10^{-3} \rightarrow 10^{-2}$	1
water saturated clay	$8 \rightarrow 12$	$10^{-1} \rightarrow 1$	1
dry,sandy,flat coastal land	10	2×10^{-3}	1
marshy,forested,flat land	12	8×10^{-3}	1
rich agricultural land, low hills	15	10^{-2}	1
pastoral land, medium hills and forestation	13	5×10^{-3}	1
granite, dry	5	10^{-8}	1
limestone, dry	7	10^{-9}	1
B.Metals			
silver	1	$6.3 \times 10^{+7}$	1
copper	1	$6.0 \times 10^{+7}$	1
gold	1	$4.3 \times 10^{+7}$	1
aluminum	1	$3.8 \times 10^{+7}$	1
iron	1	$1.0 \times 10^{+7}$	$50 \rightarrow 1000$
bismuth	1	$9.4 \times 10^{+5}$	1
C.Miscellaneous			
air	1	0	
fresh water	81	$10^{-4} \rightarrow 3 \times 10^{-2}$	1
sea water	81	4	
fresh water ice	4	$10^{-4} \rightarrow 10^{-2}$	1
permafrost	$4 \rightarrow 8$	$10^{-5} \rightarrow 10^{-2}$	1

Table 3.2

CONDUCTIVITIES FOR THREE SIMPLE ANISOTROPY MODELS

Model	$\sigma_1 = 10\sigma_2$	$\sigma_1 = 100\sigma_2$
a	$\sigma_x = \sigma_y = \sigma_z = 1.47\sigma_2$	$\sigma_x = \sigma_y = \sigma_z = 7.47\sigma_2$
b	$\sigma_x = \sigma_y = 2.8\sigma_2$ $\sigma_z = 1.22\sigma_2$	$\sigma_x = \sigma_y = 20.8\sigma_2$ $\sigma_z = 1.25\sigma_2$
c	$\sigma_x = \sigma_y = \sigma_z = 1.53\sigma_2$	$\sigma_x = \sigma_y = \sigma_z = 1.72\sigma_2$

Table 4.1

δ_m AS A FUNCTION OF m AND μ_r FOR $n = 1$

μ_r	$m=1$	$m=2$	$m=3$	$m=4$	$m=5$	$m=6$	$m=7$	$m=8$	$m=20$
1	π	2π	3π	4π	5π	6π	7π	8π	20π
10	4.102	7.105	10.11	13.14	16.2	19.28	22.37	25.47	62.97
20	4.28	7.37	10.42	13.47	16.53	19.6	22.67	25.76	63.12
50	4.4	7.58	10.69	13.8	16.9	19.99	23.09	26.18	63.48
100	4.45	7.65	10.8	13.93	17.05	20.17	23.29	26.4	63.82
150	4.46	7.67	10.83	13.97	17.1	20.24	23.37	26.49	63.98
100	4.47	7.68	10.85	13.99	17.14	20.27	23.4	26.53	64.01

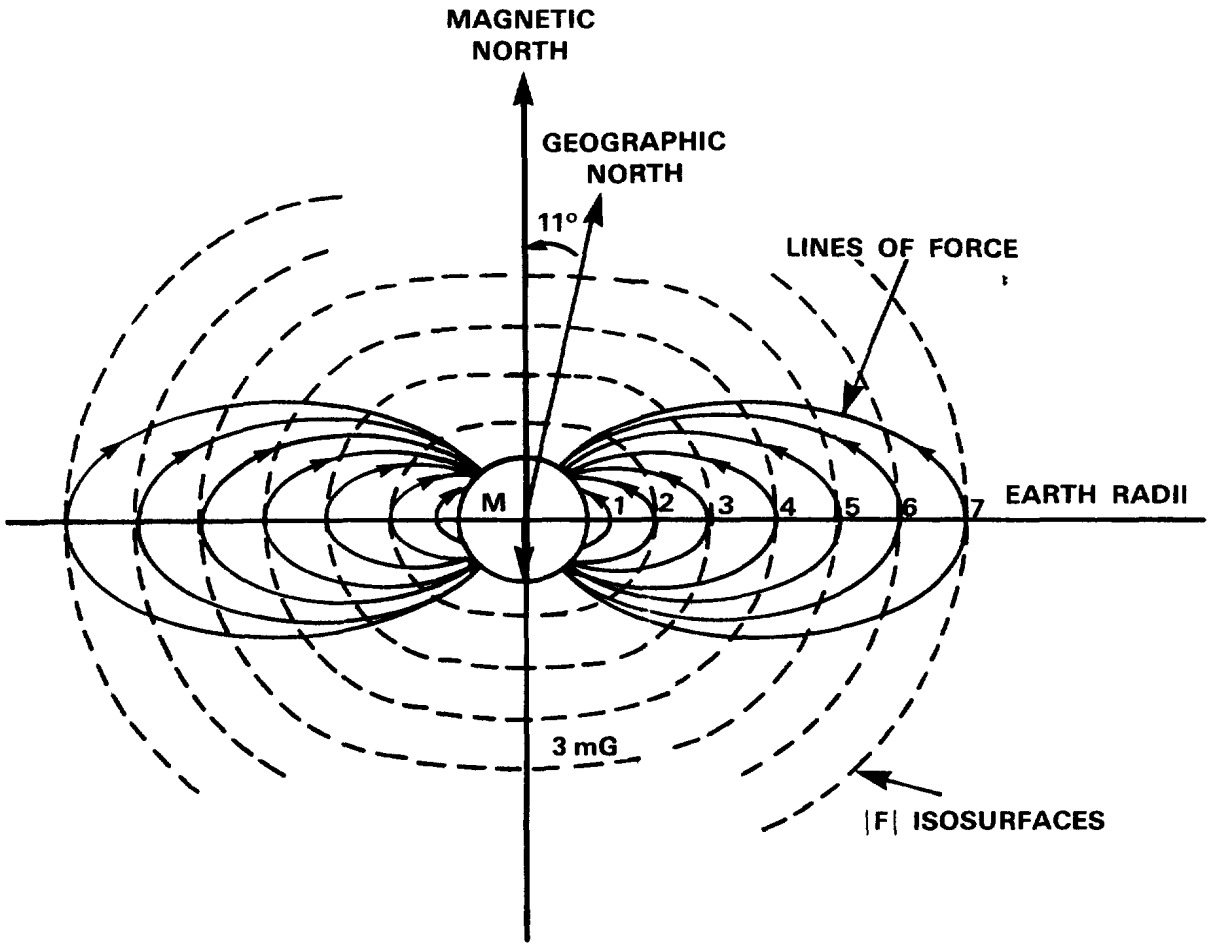

Figure 2.1

THE EARTH AS A MAGNETIC DIPOLE
(Grivet and Malnar)

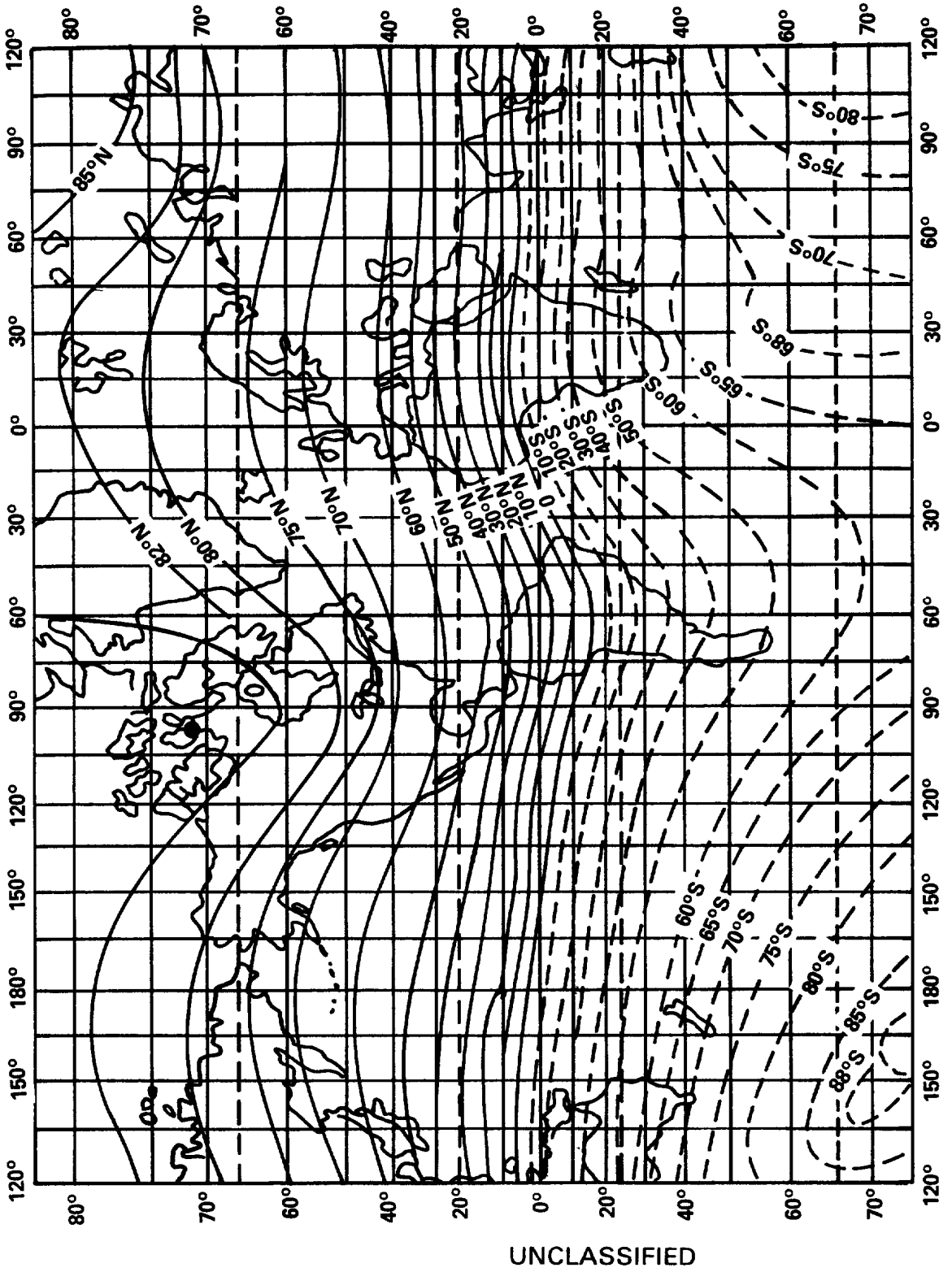

SOURCE: U.S.N.H.O.

Figure 2.2

THE GEOMAGNETIC INCLINATION IN DEGREES OF ARC FROM THE HORIZONTAL

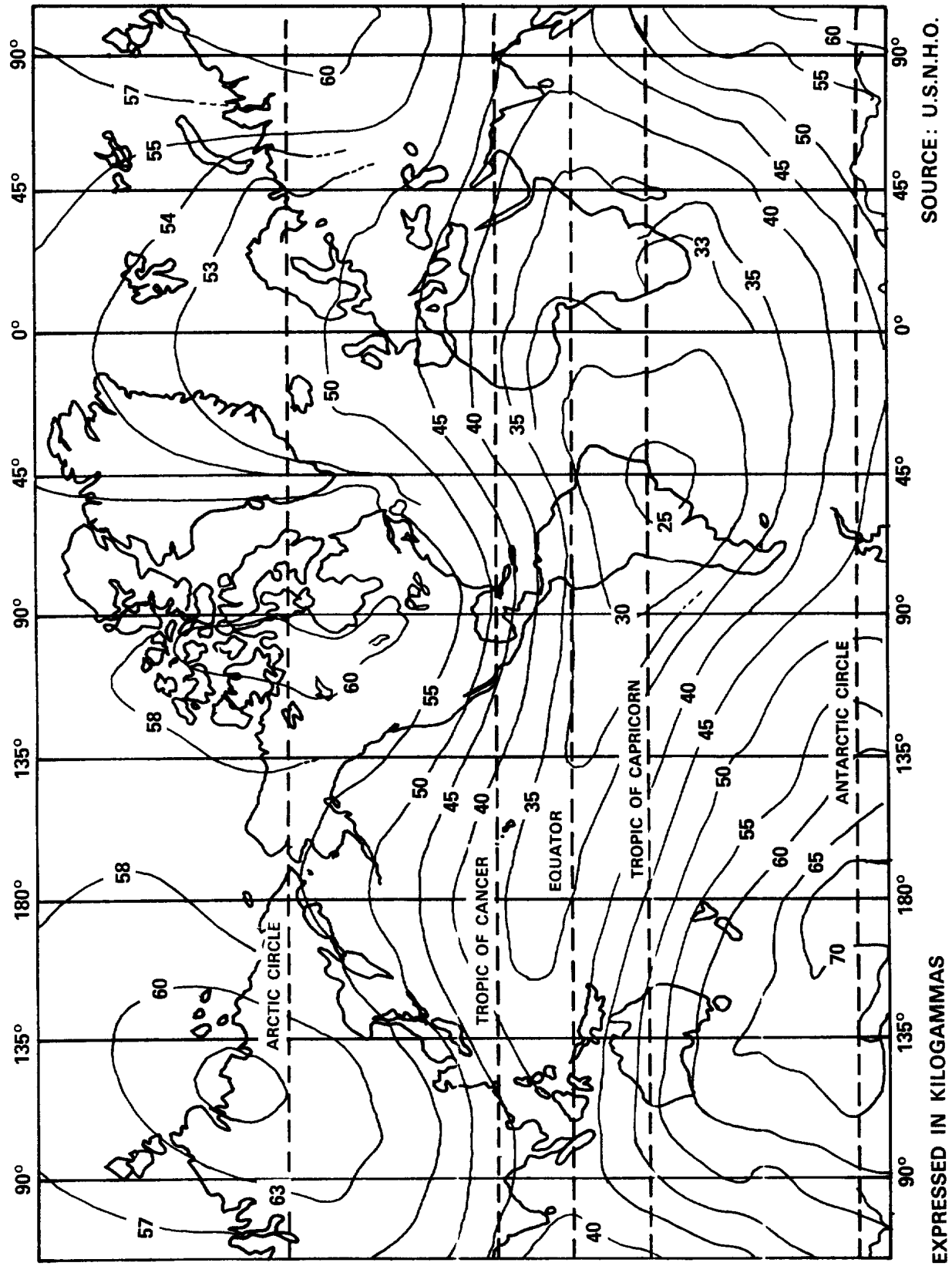

Figure 2.3

THE TOTAL INTENSITY OF THE EARTH'S MAGNETIC FIELD

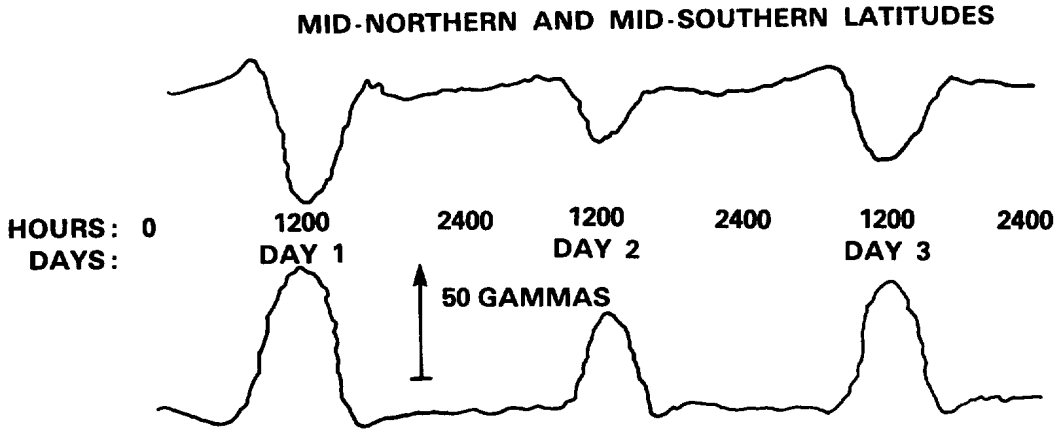

TYPICAL DIURNAL VARIATIONS IN TOTAL FIELD INTENSITY

Figure 2.4

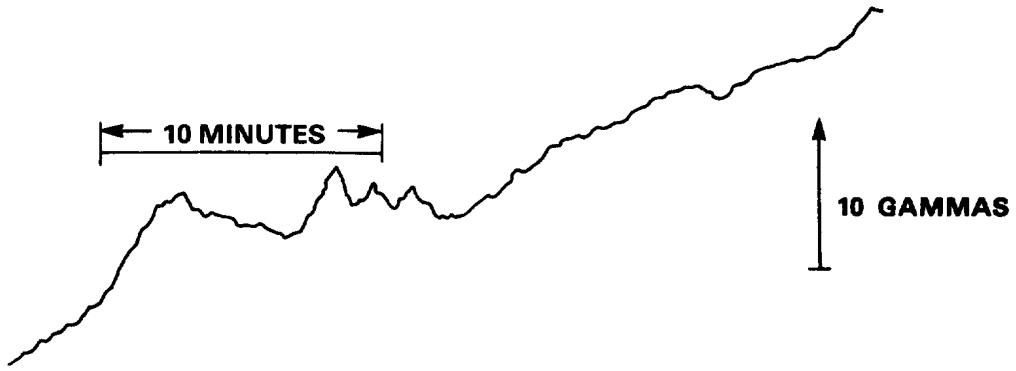

TYPICAL MICROPULSATIONS

Figure 2.5

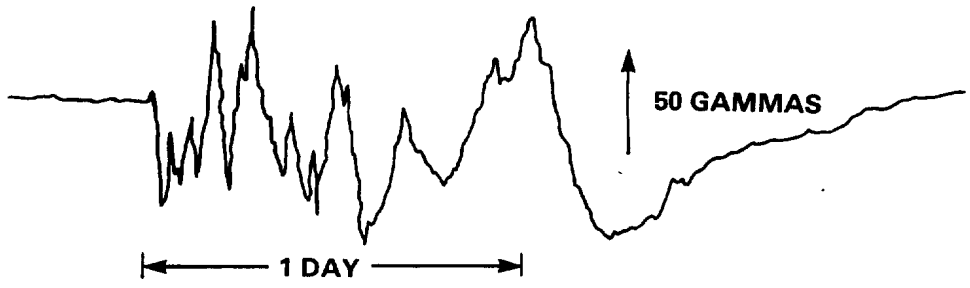

TYPICAL MAGNETIC STORM

Figure 2.6

TEMPORAL VARIATIONS IN THE GEOMAGNETIC FIELD (Breiner)

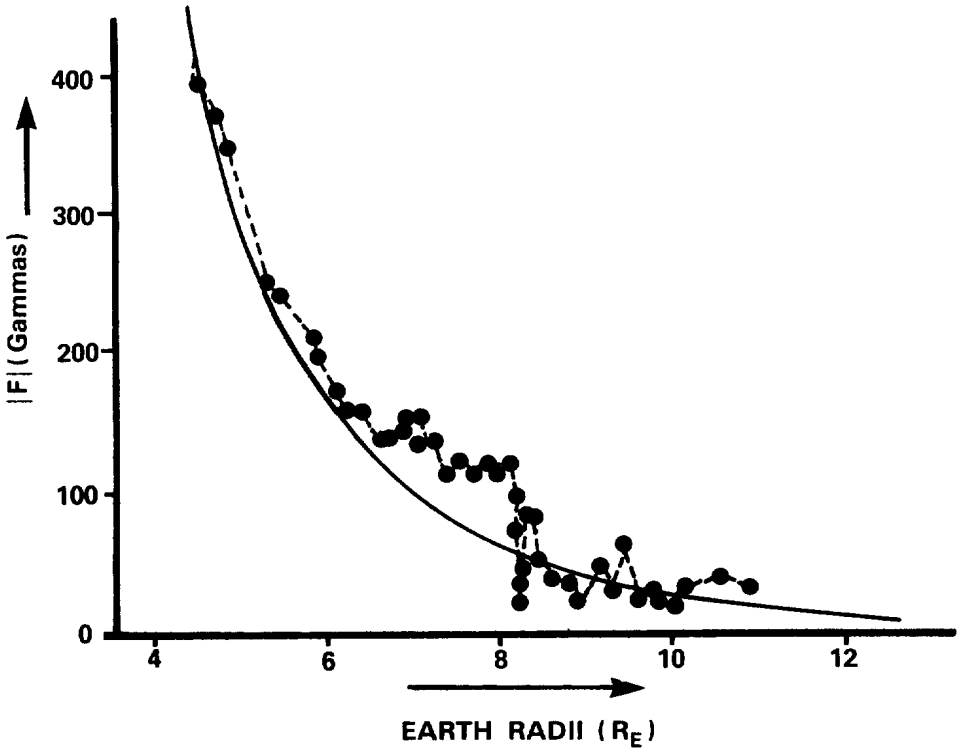

Figure 2.7

PIONEER V "NEAR ZONE" FIELD MEASUREMENTS
(Grivet and Malnar)

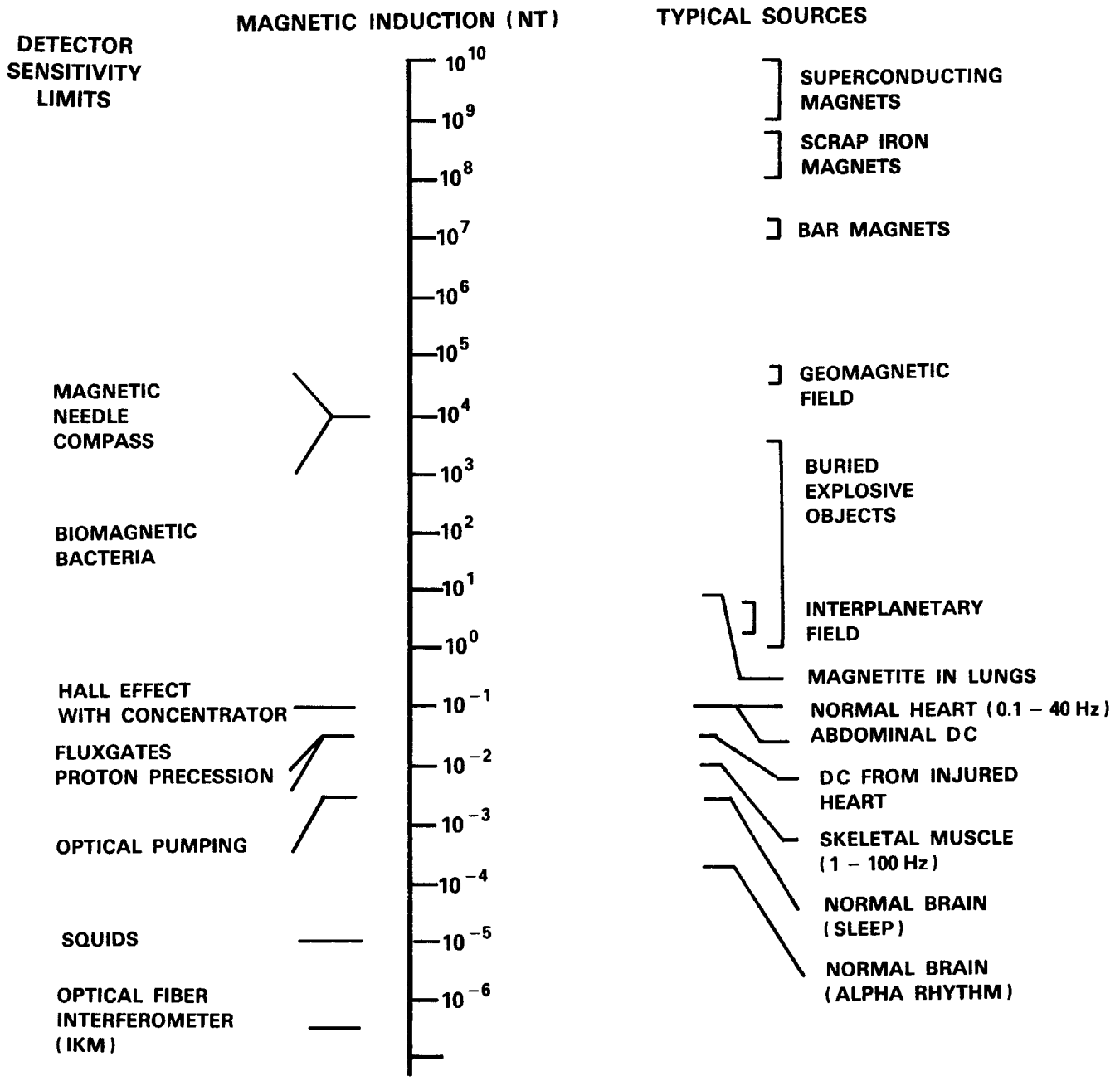

Figure 2.8

TYPICAL MAGNETIC SOURCE STRENGTHS AND DETECTOR SENSITIVITIES

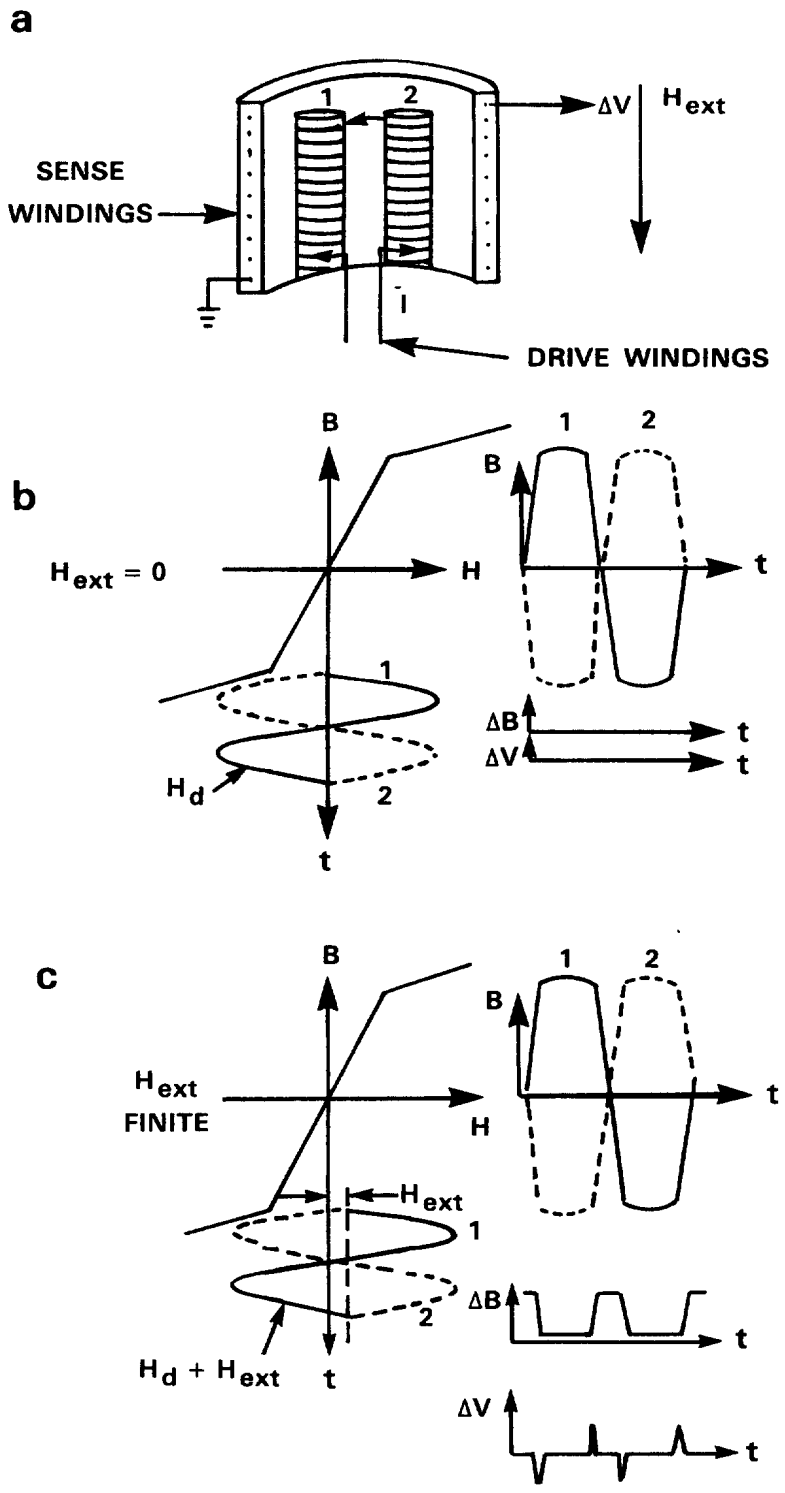

Figure 2.9

FLUXGATE MAGNETOMETER PRINCIPLE OF OPERATION

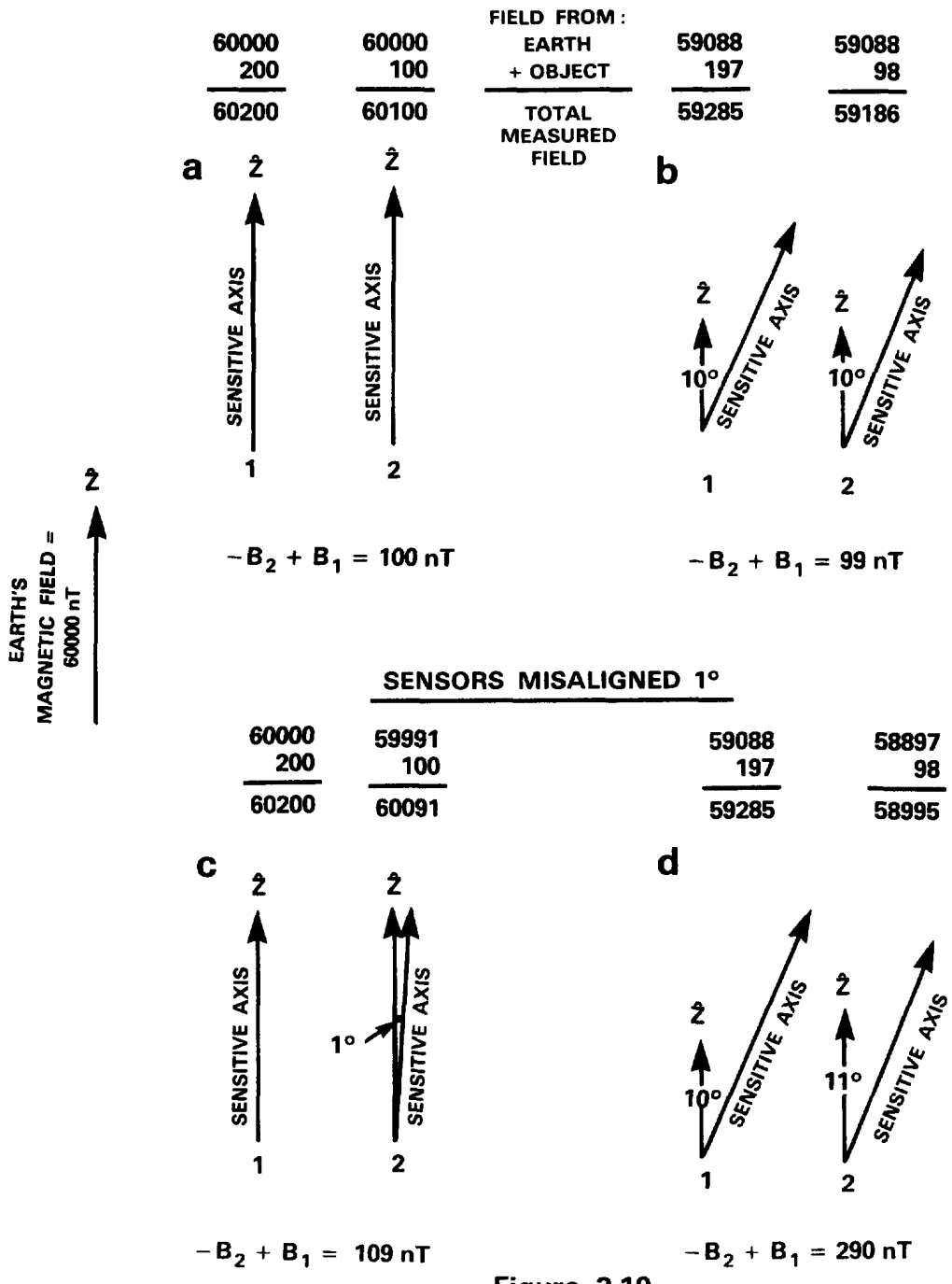

Figure 2.10

HOW MISALIGNMENT IN A VECTOR GRADIOMETER AFFECTS ERROR IN GRADIENT MEASUREMENT

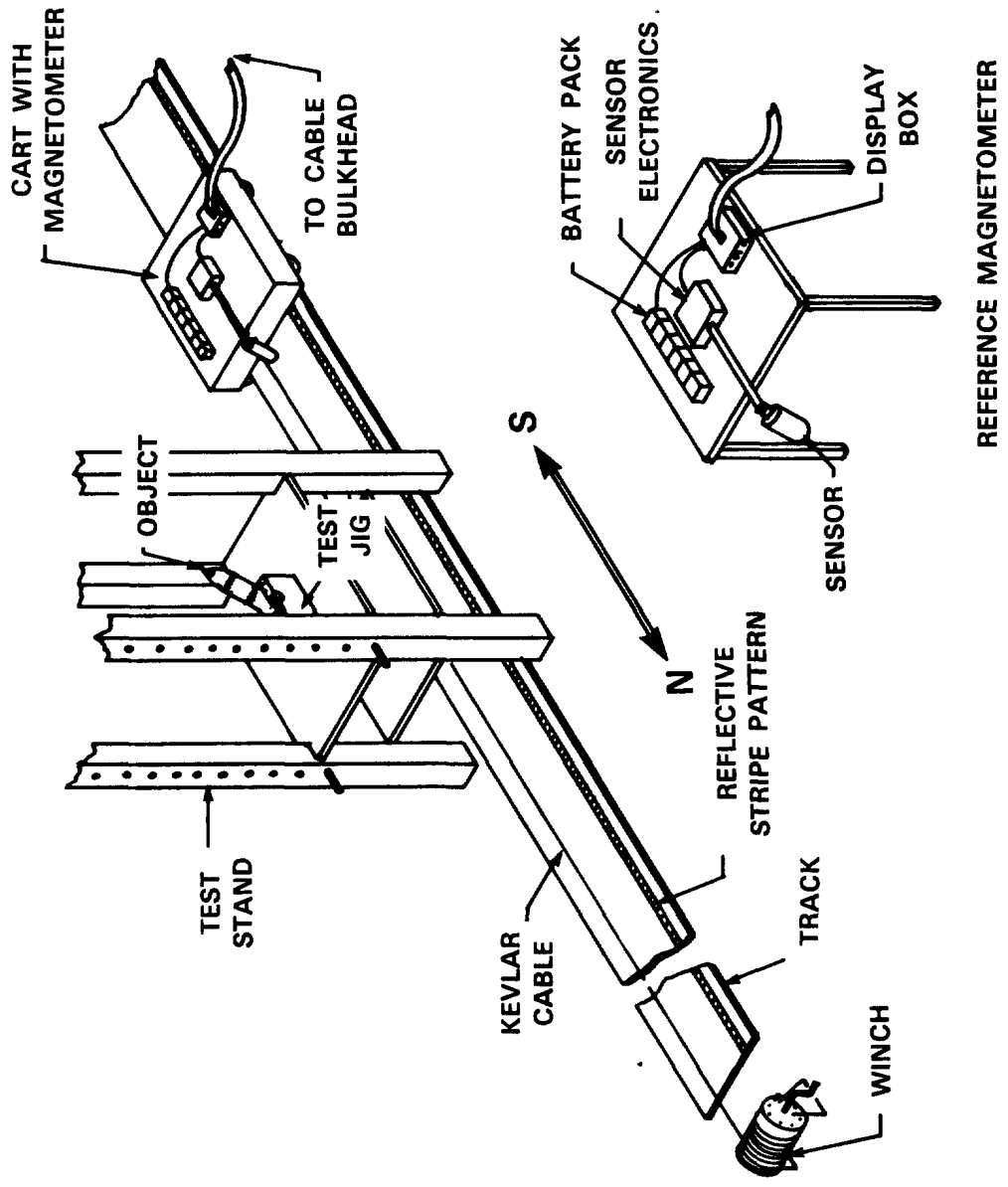

Figure 2.11

EXPERIMENTAL CONFIGURATION TO MEASURE MAGNETIC FIELDS OF A COMPACT OBJECT AS A FUNCTION OF POSITION (McFee *et al.*, 1985)

Striped track is "read" by optical sensor on cart. Apparatus is entirely nonmetallic and is situated in a nonmetallic laboratory in an isolated location.

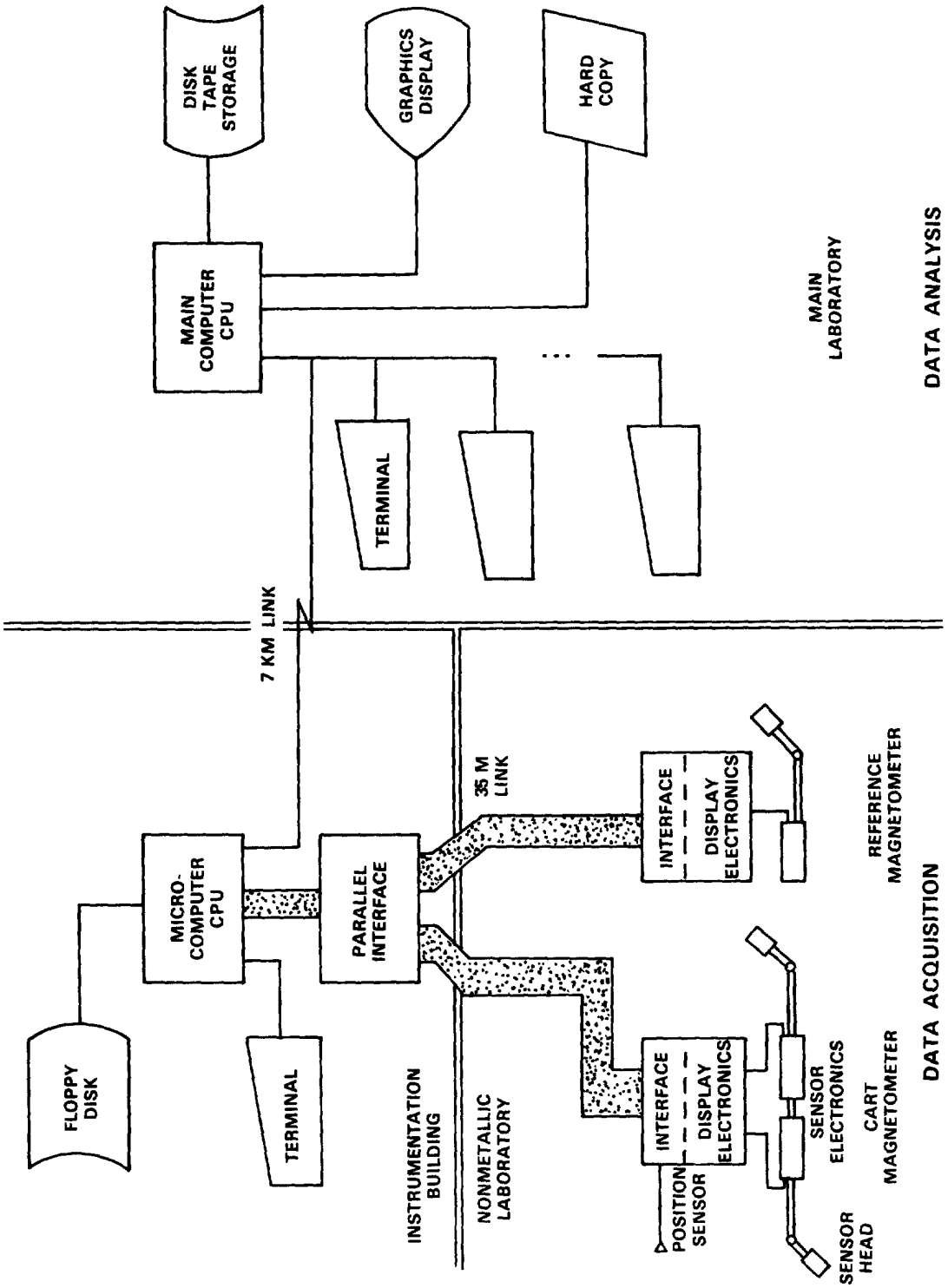

Figure 2.12

DATA COLLECTION SYSTEM FOR EXPERIMENTS OF FIGURE 2.11

Note distance of instrumentation from sensors.

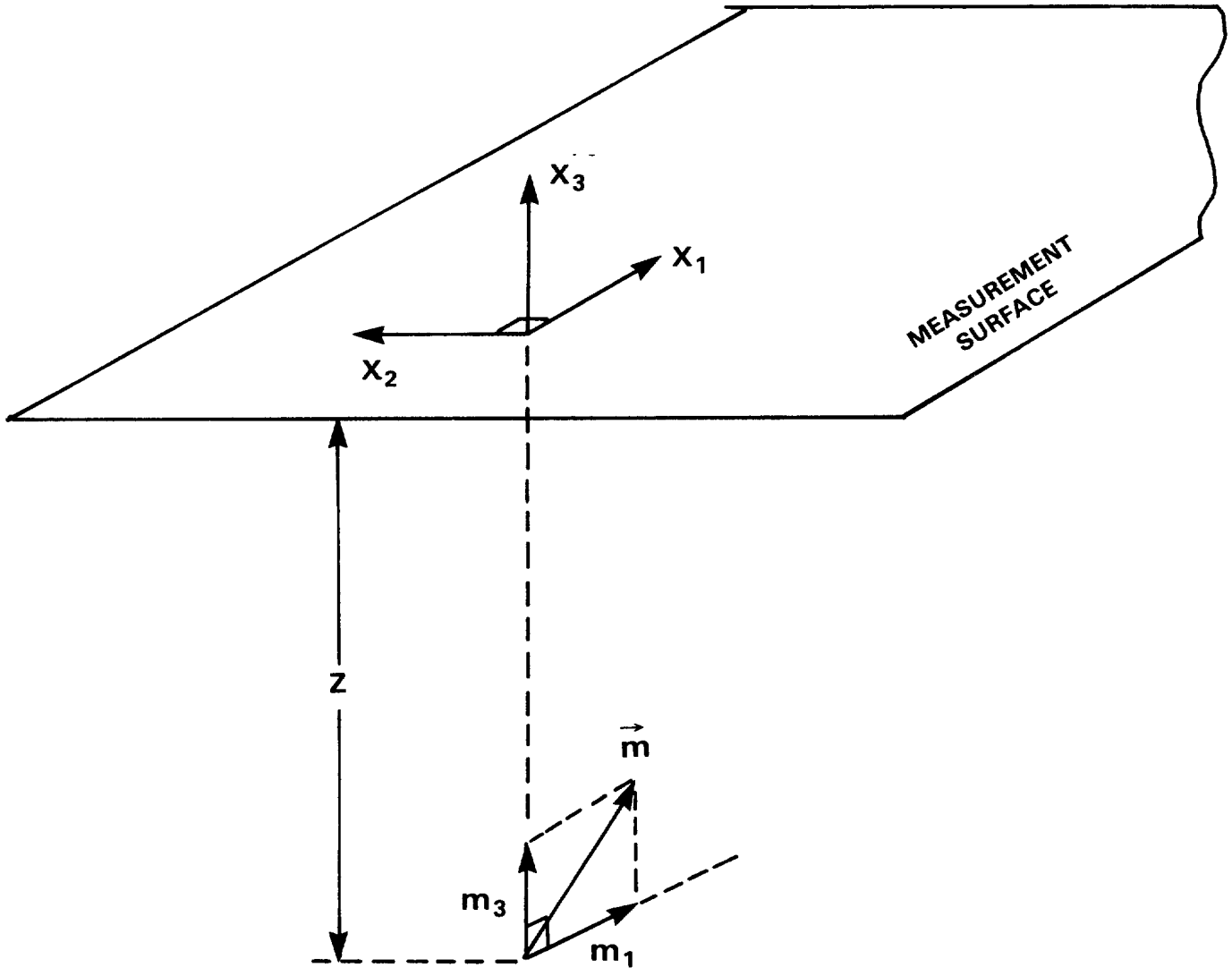

Figure 2.13

GEOMETRY FOR DIPOLE LOCATION

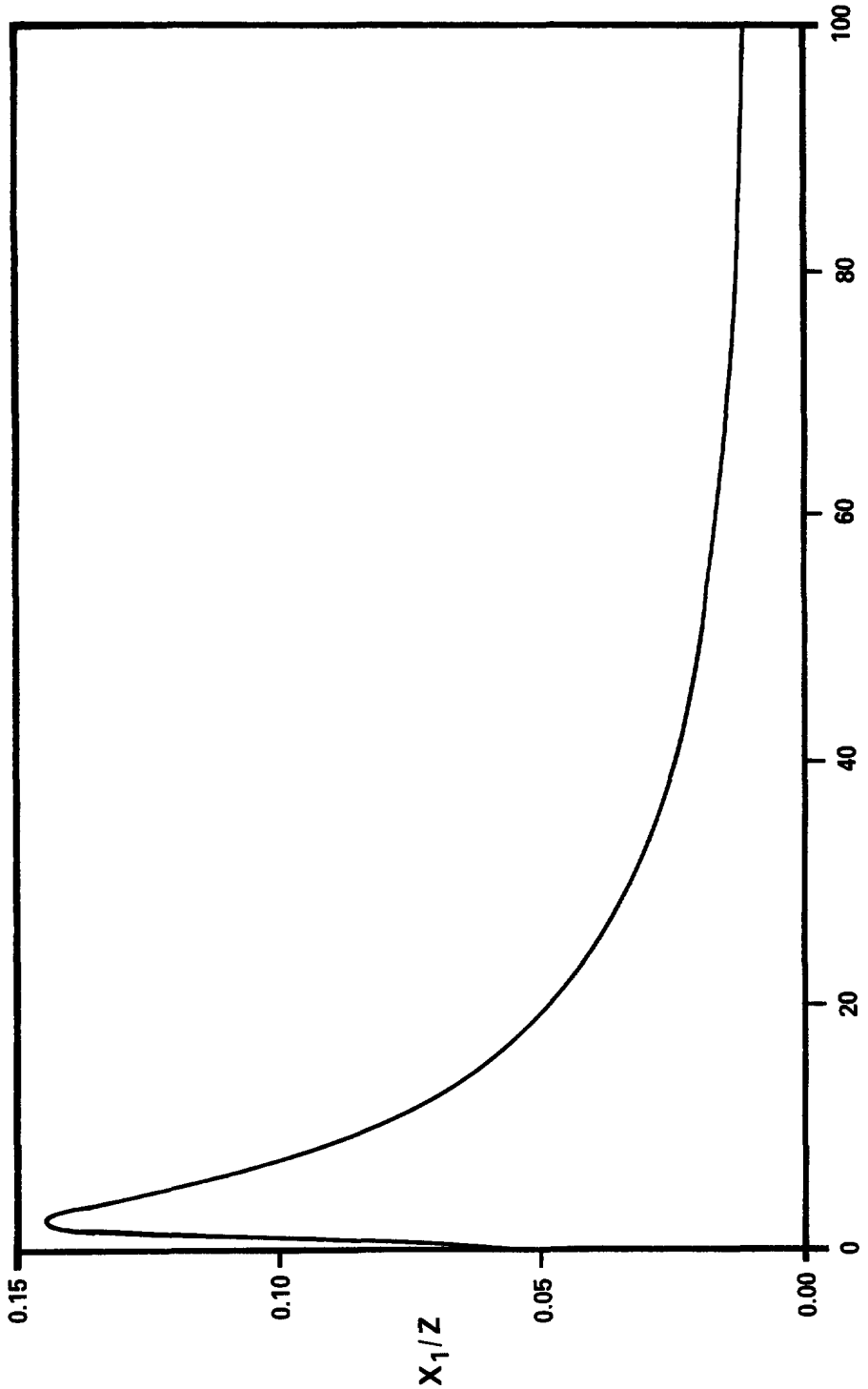

Figure 2.14

POSITION ON 1-AXIS OF MAXIMUM OF THE GRADIENT MEASUREMENT QUANTITY Q (NORMALIZED TO DEPTH OF DIPOLE) VERSUS RATIO OF 1- AND 3- COMPONENTS OF DIPOLE MOMENT

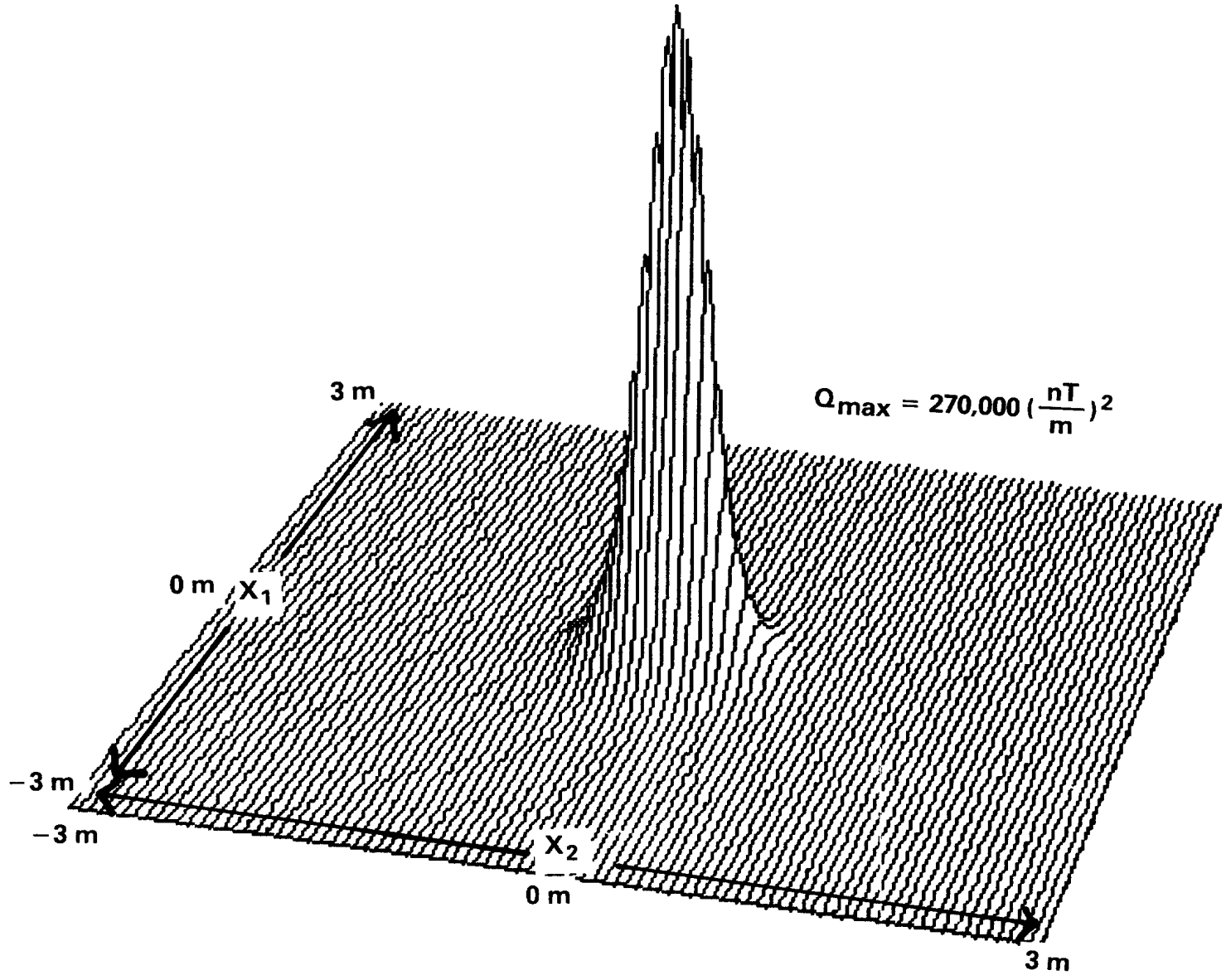

Figure 2.15

MAP OF *Q* IN PLANE 1 m ABOVE A DIPOLE
Dipole Moment $(m_1, m_2, m_3) = (0, 0, 1)$ A·m^2

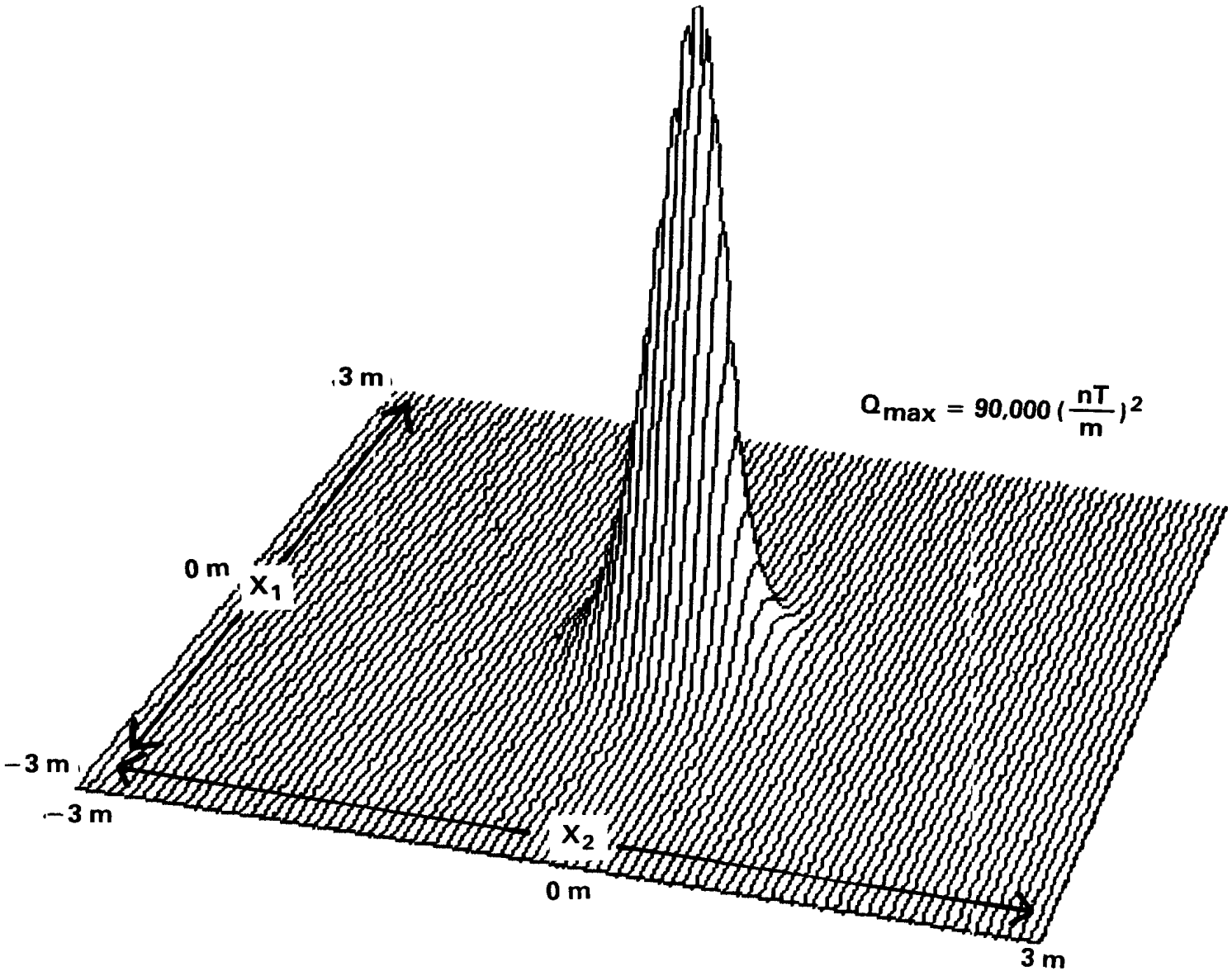

Figure 2.16

MAP OF *Q* IN PLANE 1 m ABOVE A DIPOLE
Dipole Moment $(m_1, m_2, m_3) = (1, 0, 0)$ A·m^2

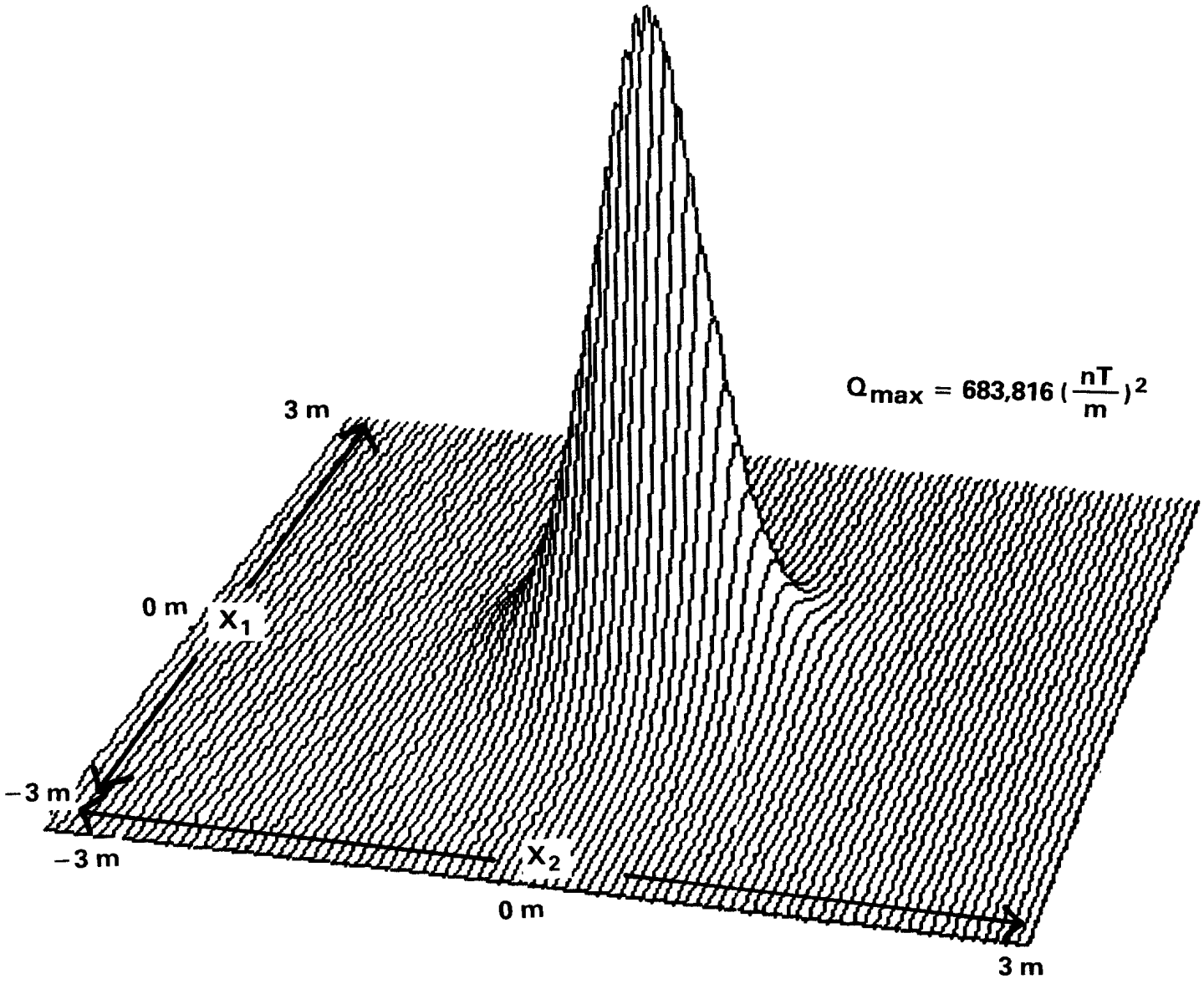

Figure 2.17

MAP OF Q IN PLANE 1 m ABOVE A DIPOLE
Dipole Moment $(m_1, m_2, m_3) = (2, 0, 1)$ A·m^2

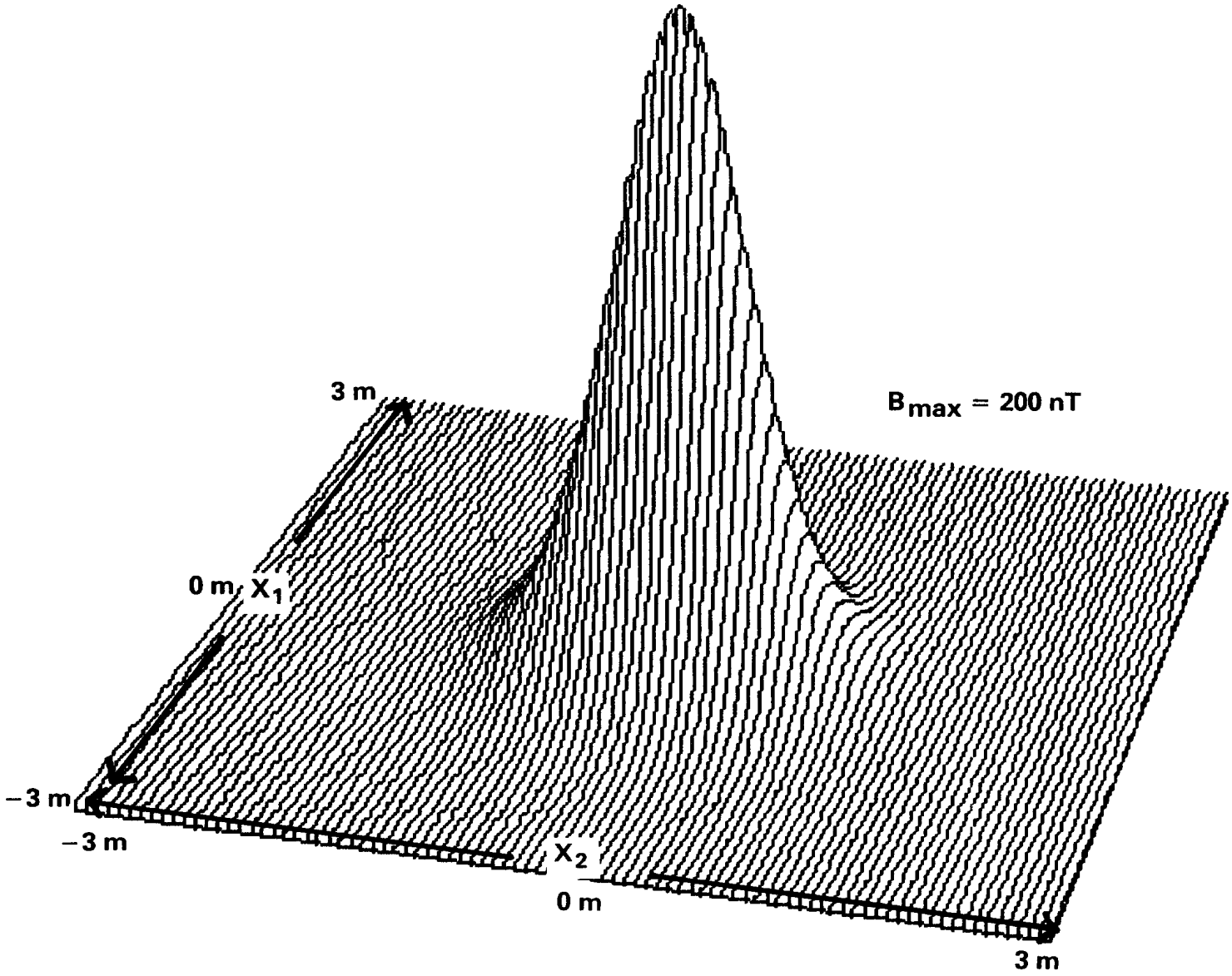

Figure 2.18

MAP OF b_3 IN PLANE 1 m ABOVE A DIPOLE
Dipole Moment (m_1, m_2, m_3) = (0, 0, 1) A·m^2

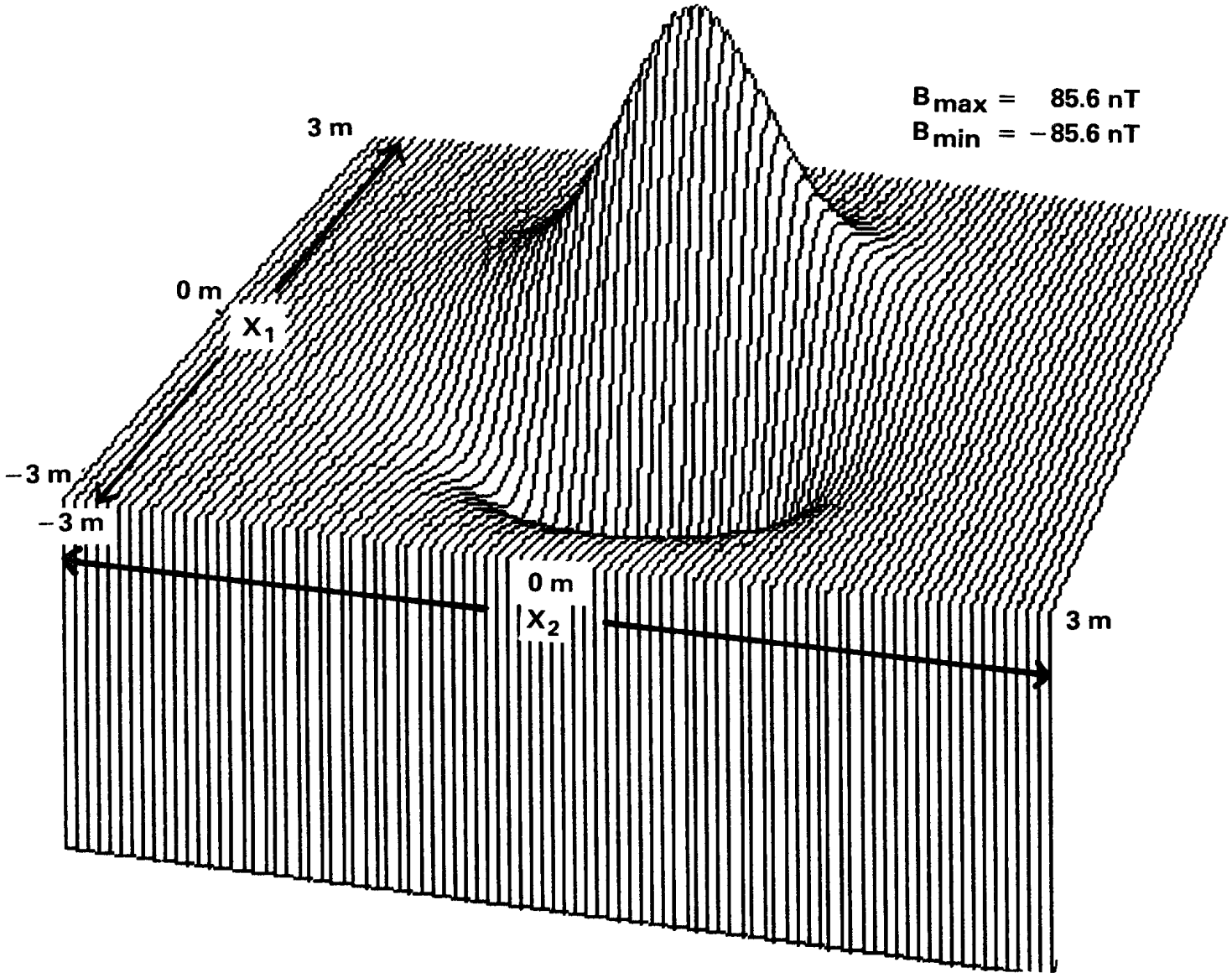

Figure 2.19

MAP OF b_3 IN PLANE 1 m ABOVE A DIPOLE
Dipole Moment $(m_1, m_2, m_3) = (1, 0, 0)$ A·m^2

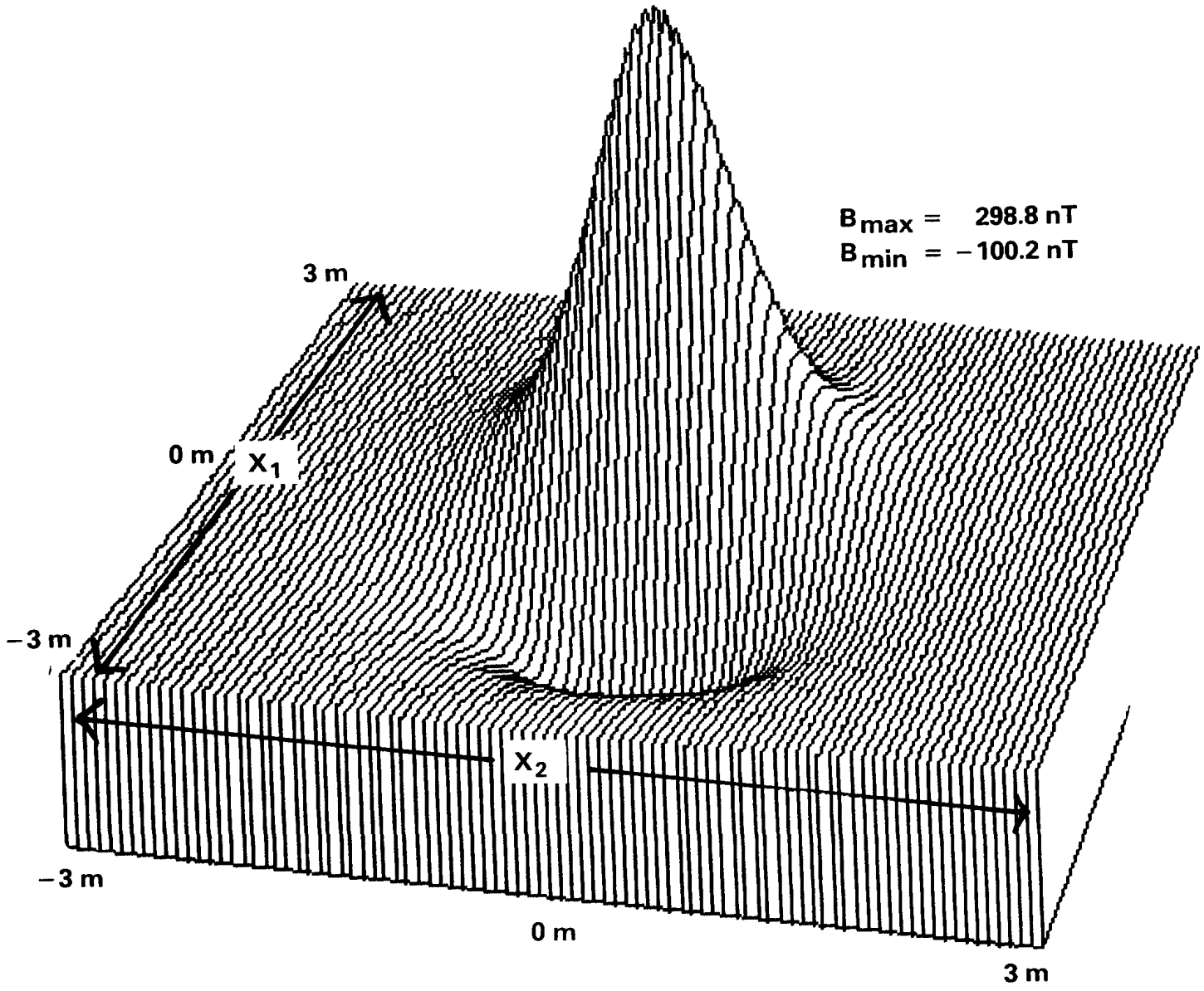

Figure 2.20

MAP OF b_3 IN PLANE 1 m ABOVE A DIPOLE
Dipole Moment $(m_1, m_2, m_3) = (2, 0, 1)$ A·m^2

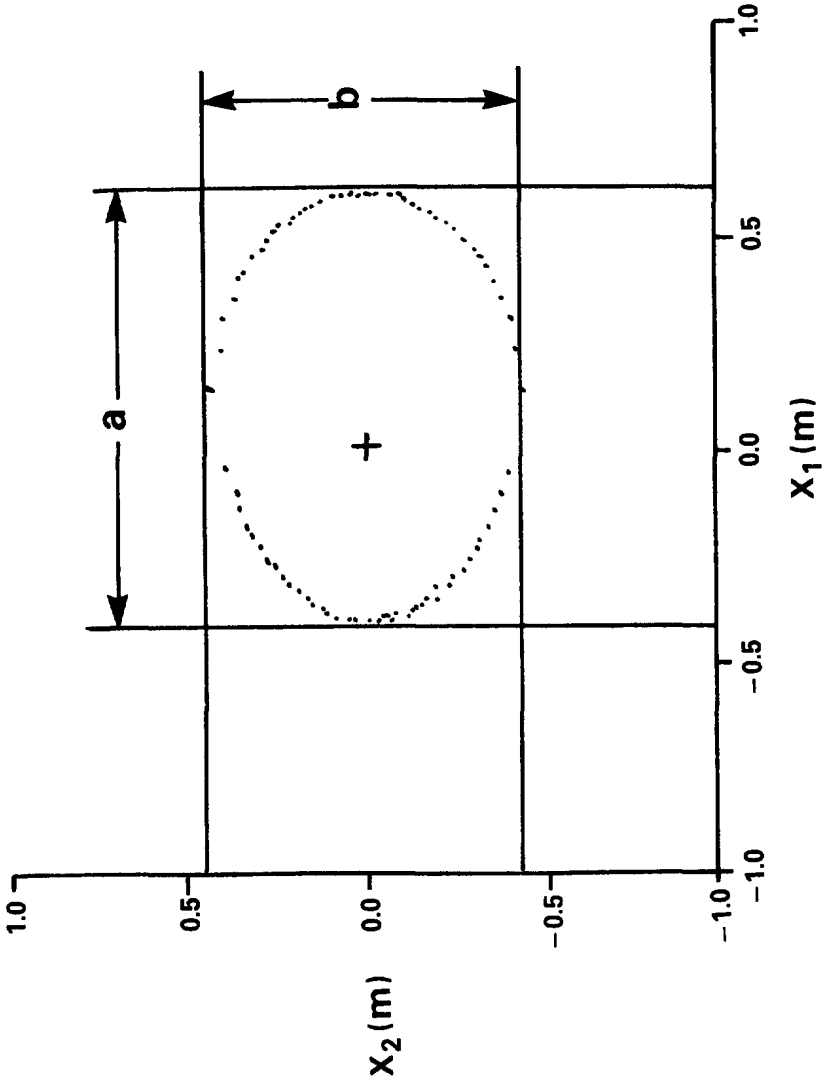

Figure 2.21

VALUE OF 1/2 Q_{max} IN PLANE 1 m ABOVE A DIPOLE
Note that locus is not centered about (X_1, X_2) = (0, 0).

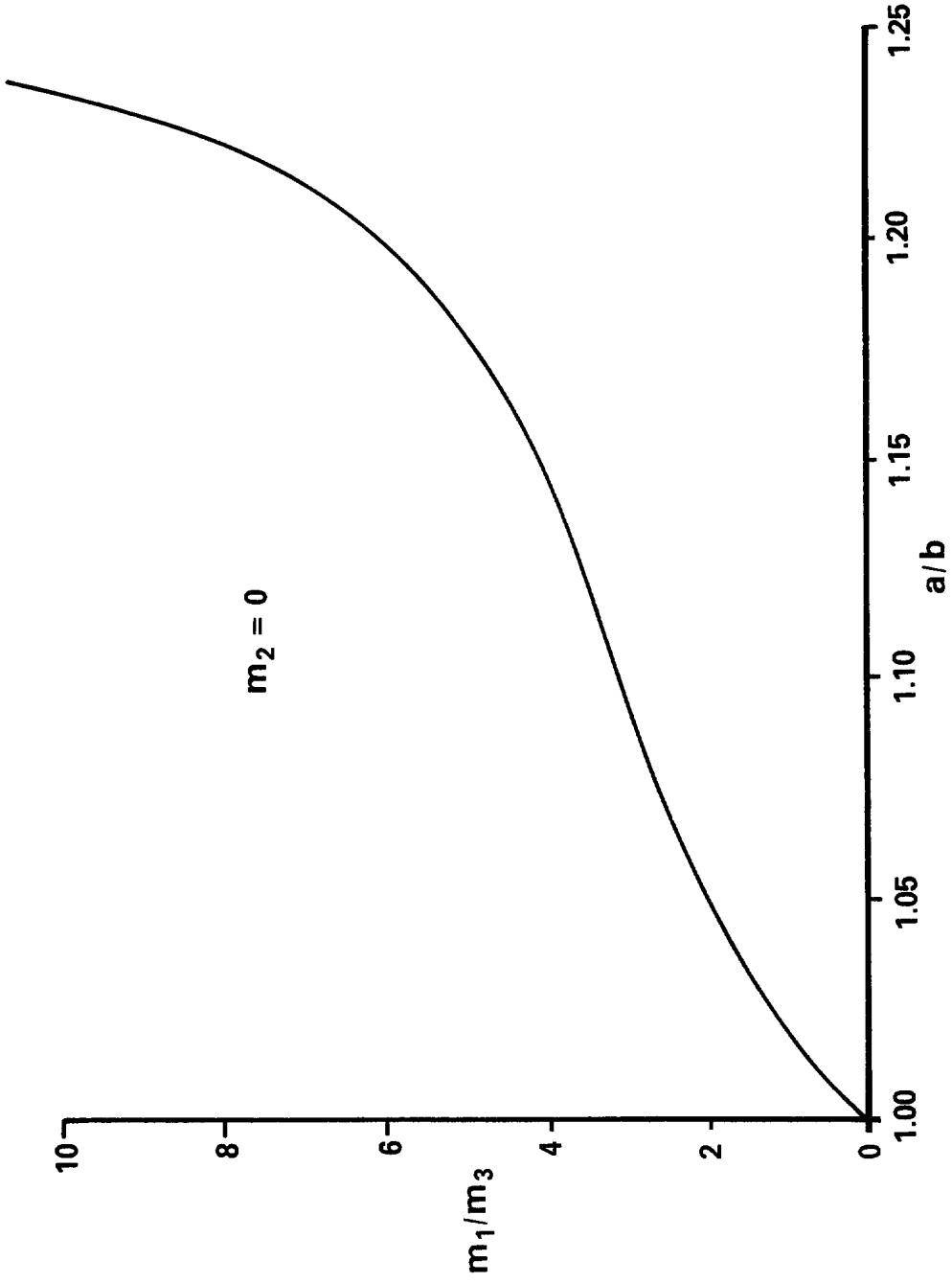

Figure 2.22

RATIO OF MAXIMUM EXTENT IN X_1 AND X_2 DIRECTIONS OF LOCUS OF 1/2 Q_{max} VERSUS RATIO OF 1- AND 3-COMPONENTS OF DIPOLE MOMENT

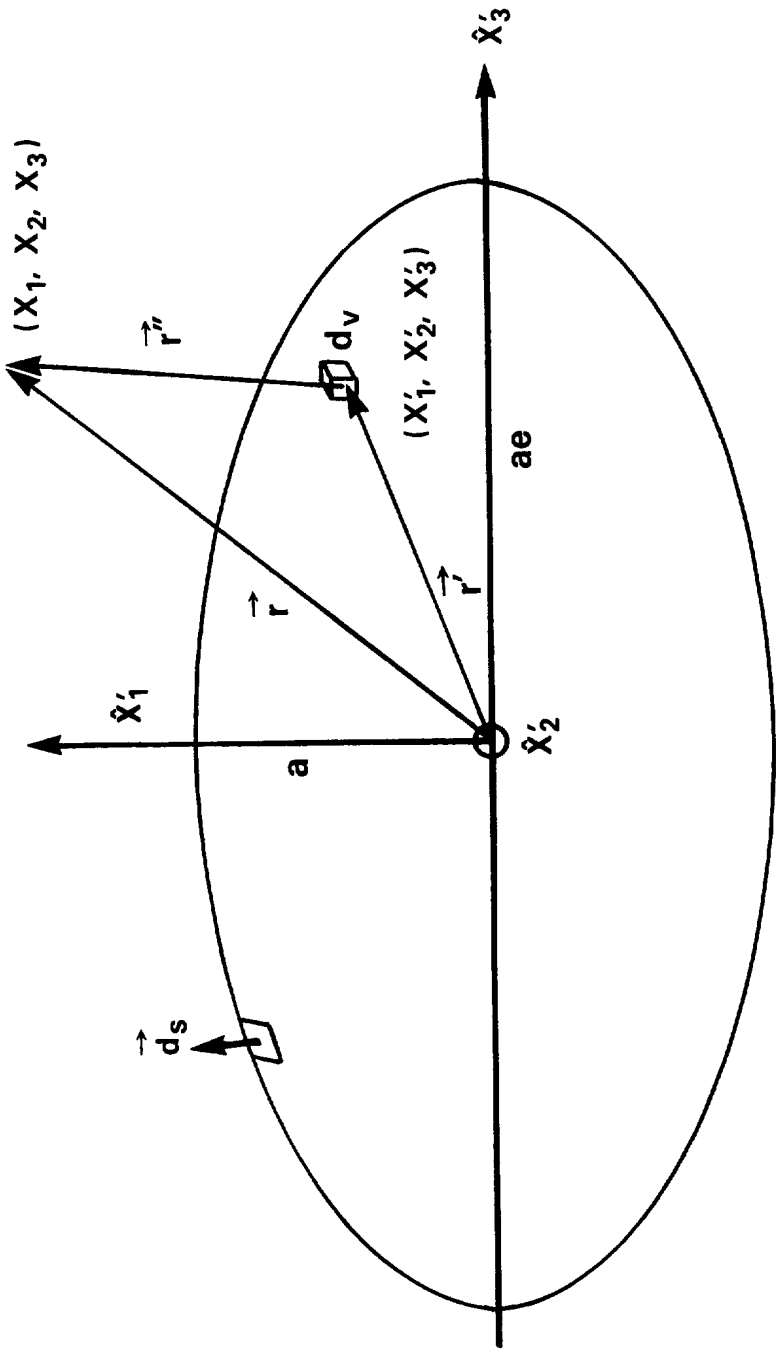

Figure 2.23

GEOMETRY FOR CALCULATION OF MULTIPOLE MOMENTS OF A SPHEROID

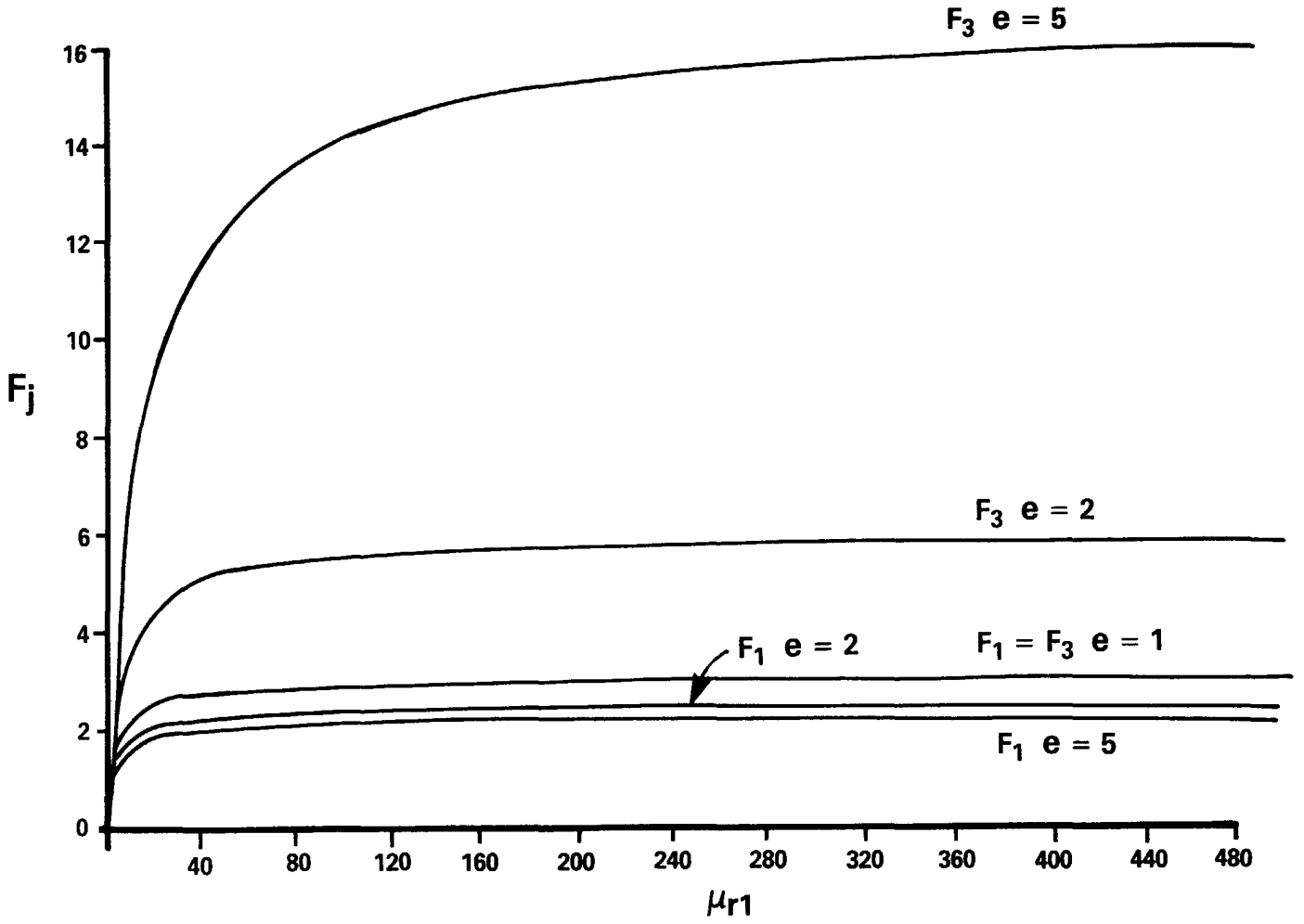

Figure 2.24

F_j FACTOR VERSUS SPHEROID RELATIVE PERMEABILITY FOR j = 1, 3 AND VARIOUS SPHEROID SHAPE PARAMETERS e

Relative permeability of surrounding medium is 1. For fixed orientation, dipole moment induced in spheroid along j axis will be proportional to F_j.

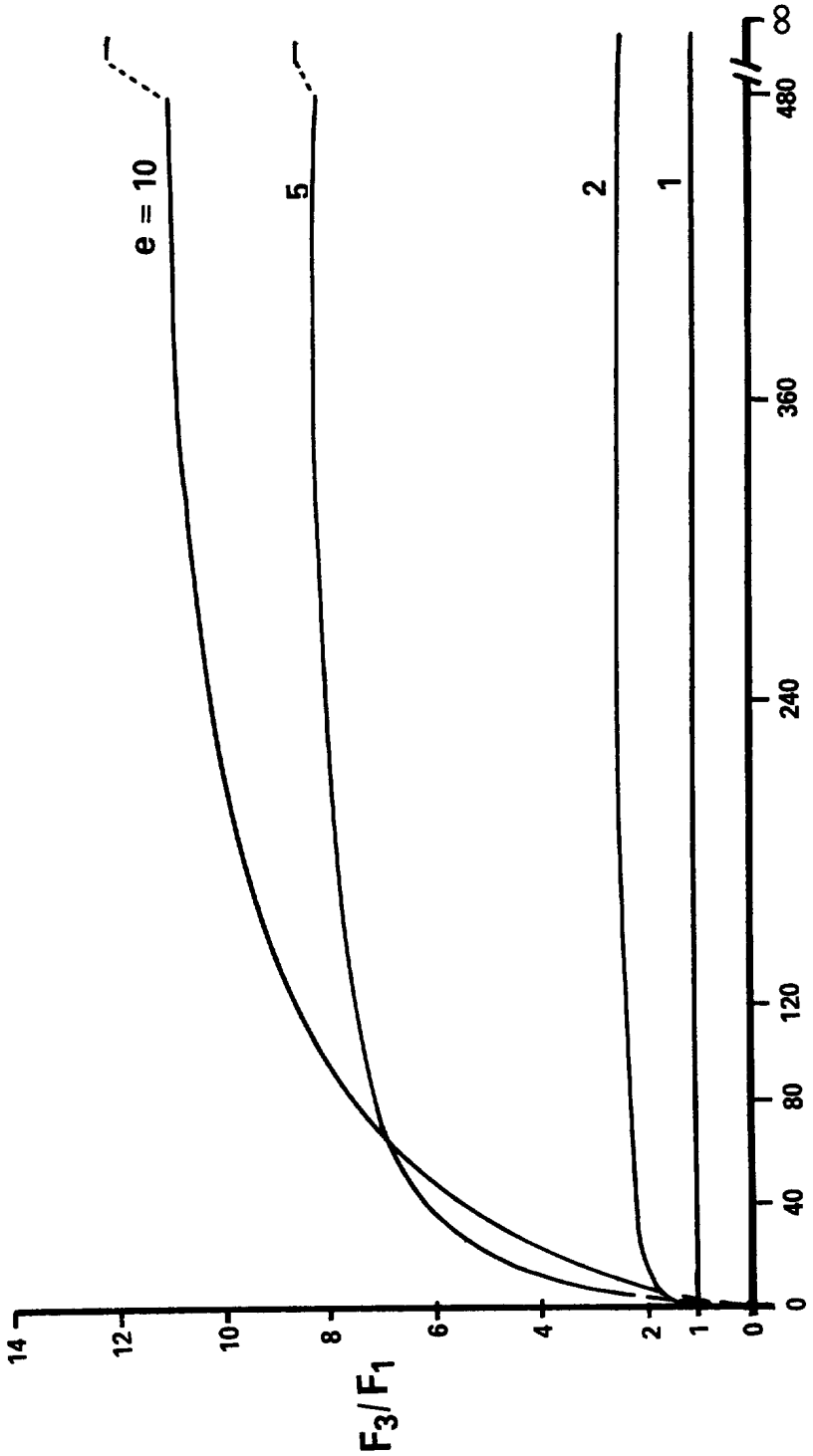

Figure 2.25

RATIO OF F_3 TO F_1 VERSUS SPHEROID RELATIVE PERMEABILITY FOR VARIOUS SPHEROID SHAPE PARAMETERS e

Relative permeability of surrounding medium is 1. For fixed orientation, ratio will be proportional to ratio of dipole moments induced in spheroid along 3 and 1 axes.

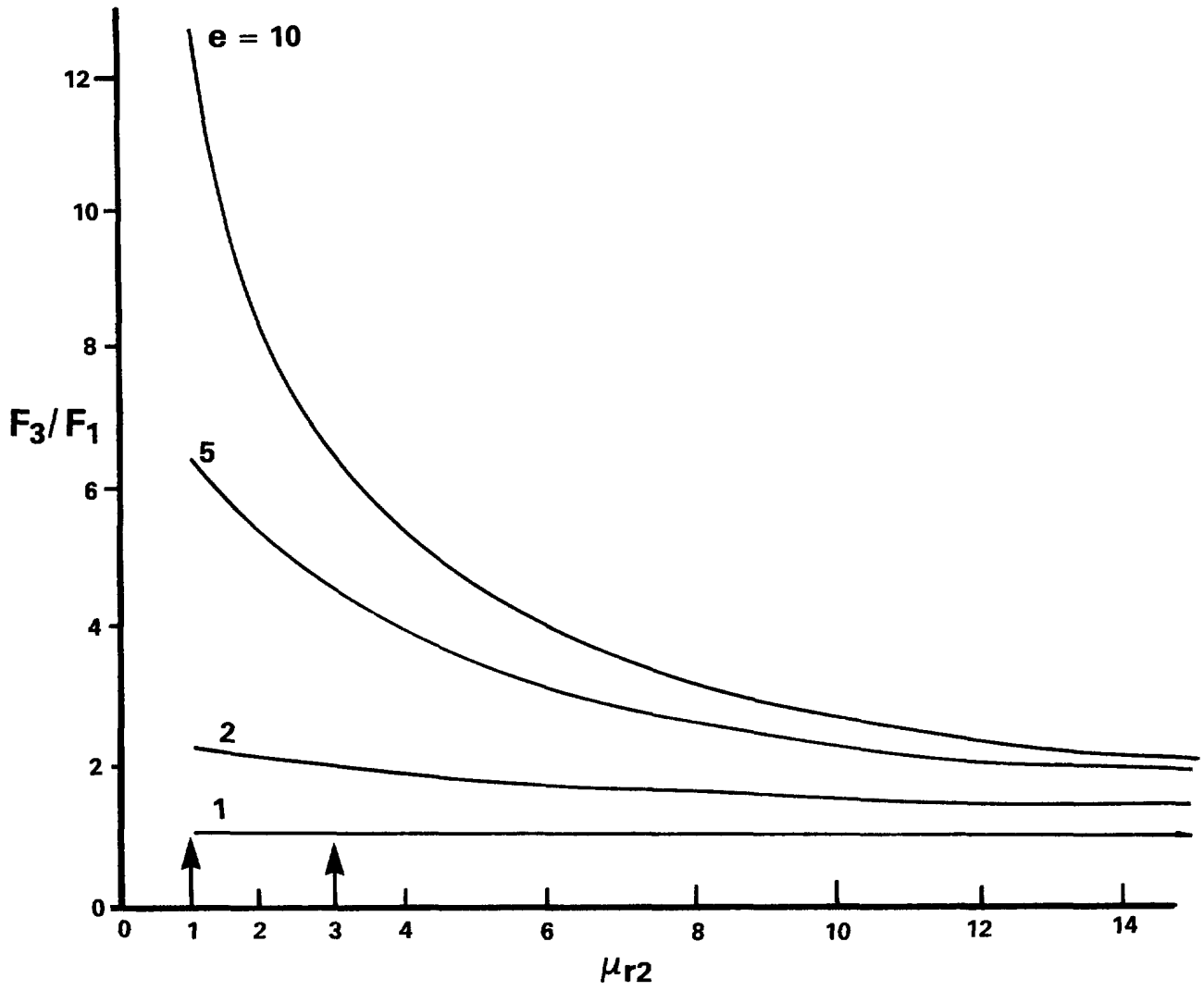

Figure 2.26

RATIO OF F_3 TO F_1 VERSUS RELATIVE PERMEABILITY OF SURROUNDING MEDIUM FOR VARIOUS SPHEROID SHAPE PARAMETERS *e*

Relative permeability of spheroid is 50. Most rocks have $\mu_{r2} = 1$ while the maximum for most ferrous rocks is $\mu_{r2} = 3$.

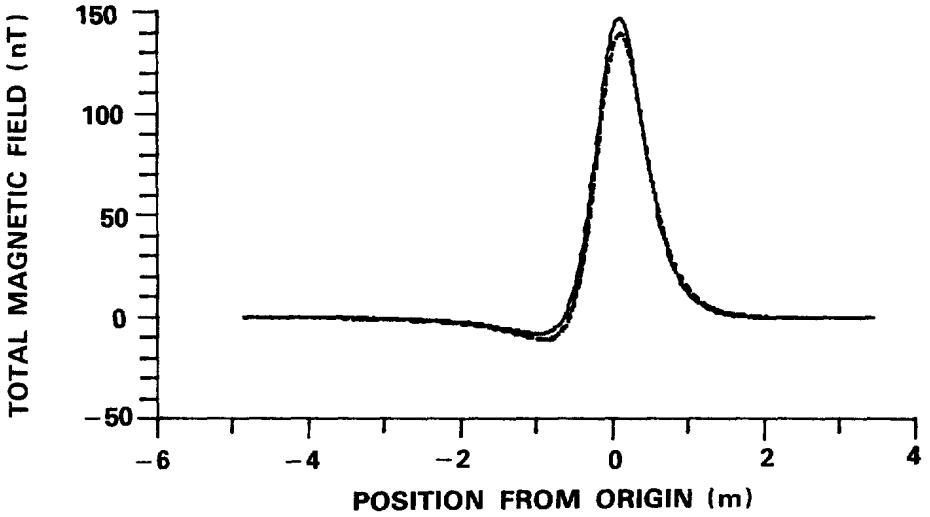

Figure 2.27

MEASURED TOTAL MAGNETIC FIELD OF A .08 m RADIUS MILD STEEL SPHERE AT A DEPTH OF 0.73 m (SOLID LINE)

Geometry is that of Figure 2.11. Sphere center is directly under position value 0. Dotted line is theoretical prediction (McFee *et al.*, 1985).

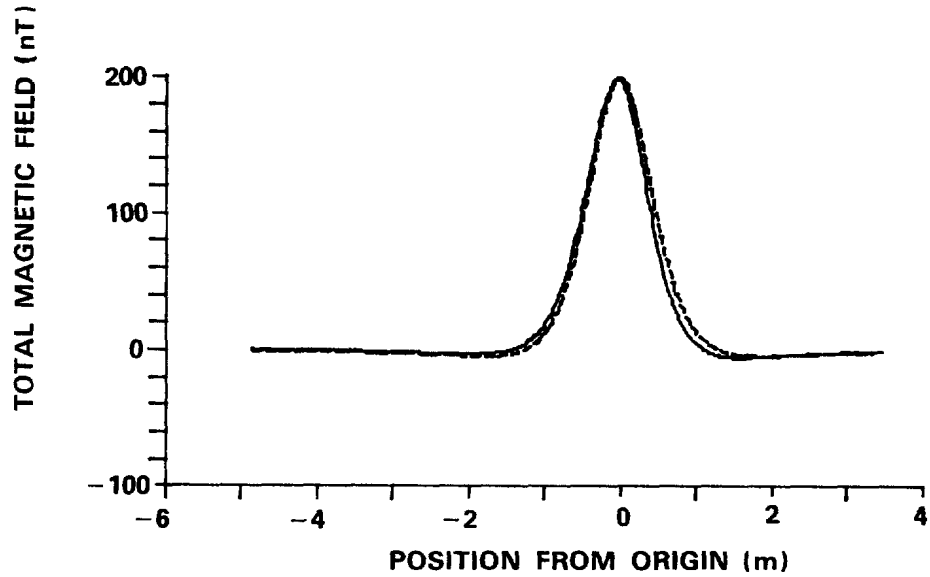

Figure 2.28

MEASURED TOTAL MAGNETIC FIELD OF A 105 mm HOWITZER SHELL AT A DEPTH OF 0.96 m (SOLID LINE).

Geometry is that of Figure 2.11. Symmetry axis is tilted 47° from vertical and its projection is 43° from magnetic north. Shell center is directly under position value 0. Dotted line is theoretical prediction (McFee *et al.*, 1985).

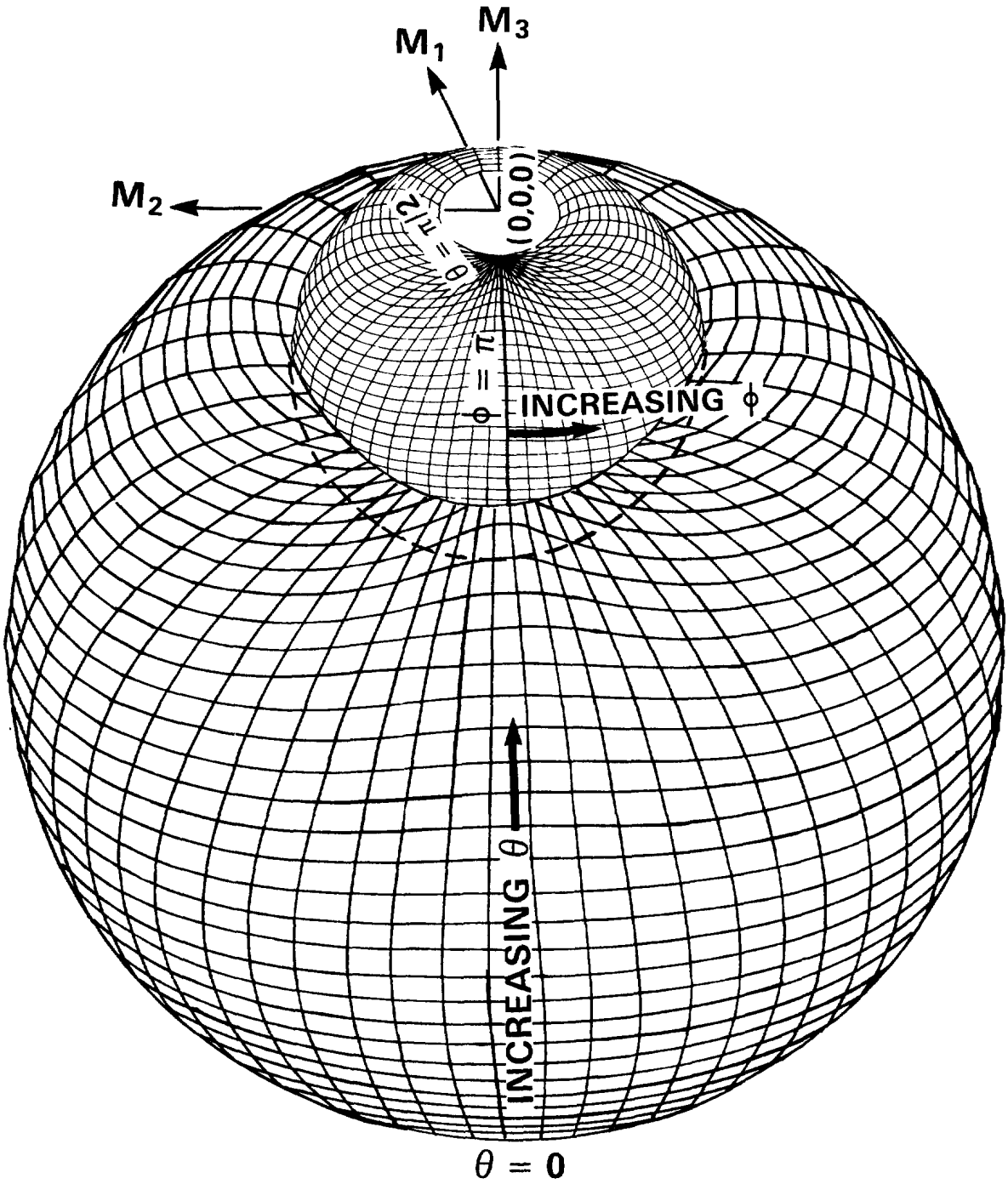

Figure 2.29

THE DESIGN PROTOTYPE MANIFOLDS FOR TWO DIFFERENT FERROUS SPHEROIDS. Each manifold is a surface consisting of a continuum of points. Each point is the head of a magnetic dipole moment vector corresponding to a polar angle, θ, and azimuthal angle, ϕ, of the symmetry axis of the spheroid with respect to a space-fixed coordinate system.

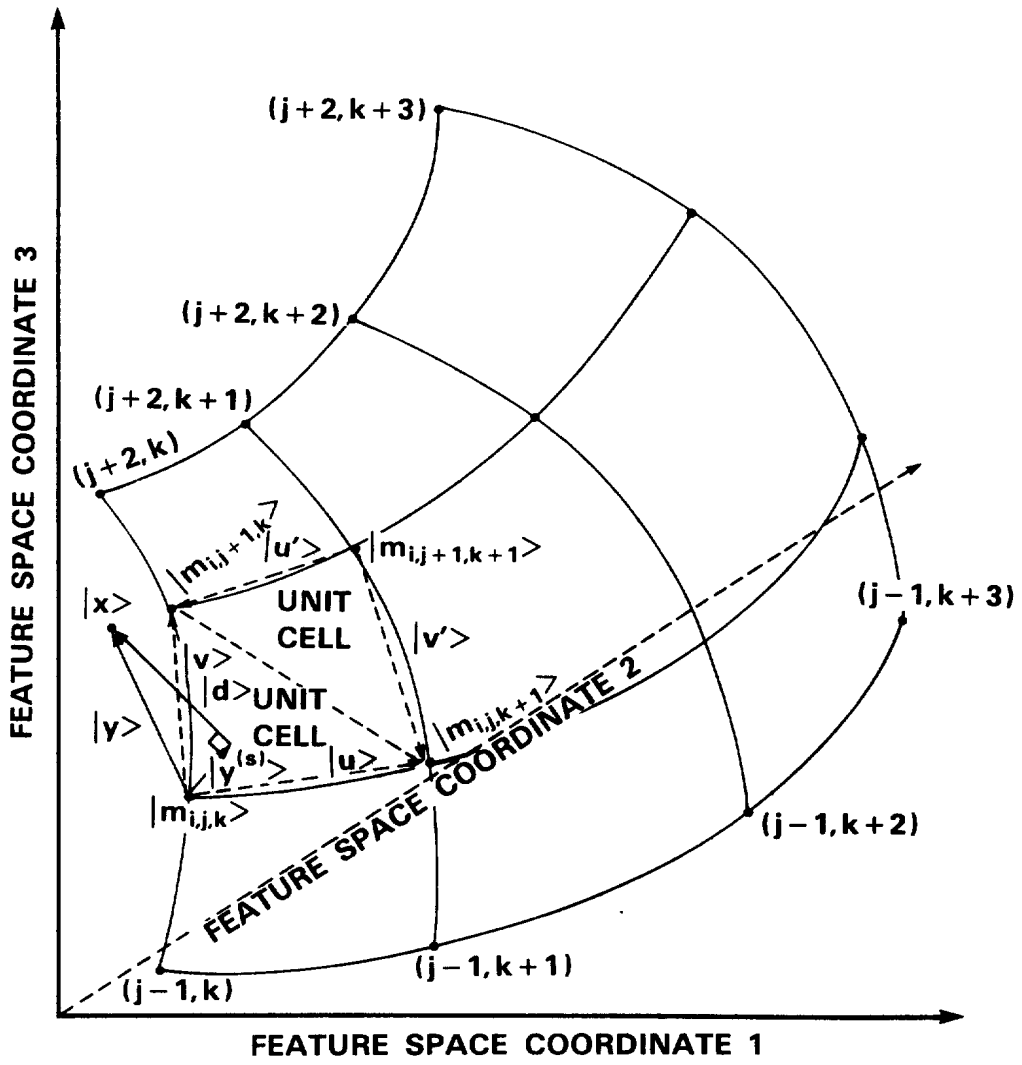

Figure 2.30

PORTION OF A TWO DIMENSIONAL PROTOTYPE MANIFOLD IN A THREE DIMENSIONAL FEATURE SPACE AND ITS APPROXIMATION BY A SET OF UNIT CELLS.

Each unit cell is a triangle formed by three adjacent points sampled on the manifold.

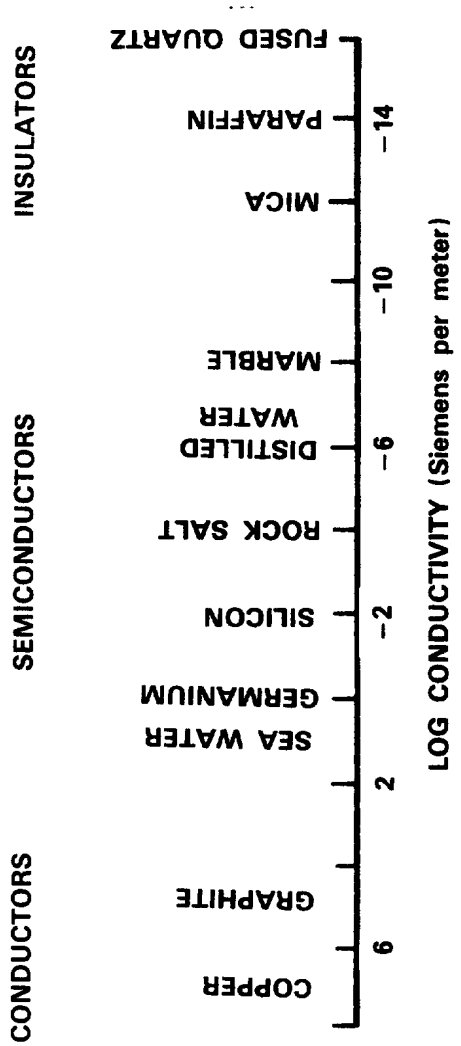

Figure 3.1

CONDUCTIVITY SPECTRUM (Ward and Fraser)

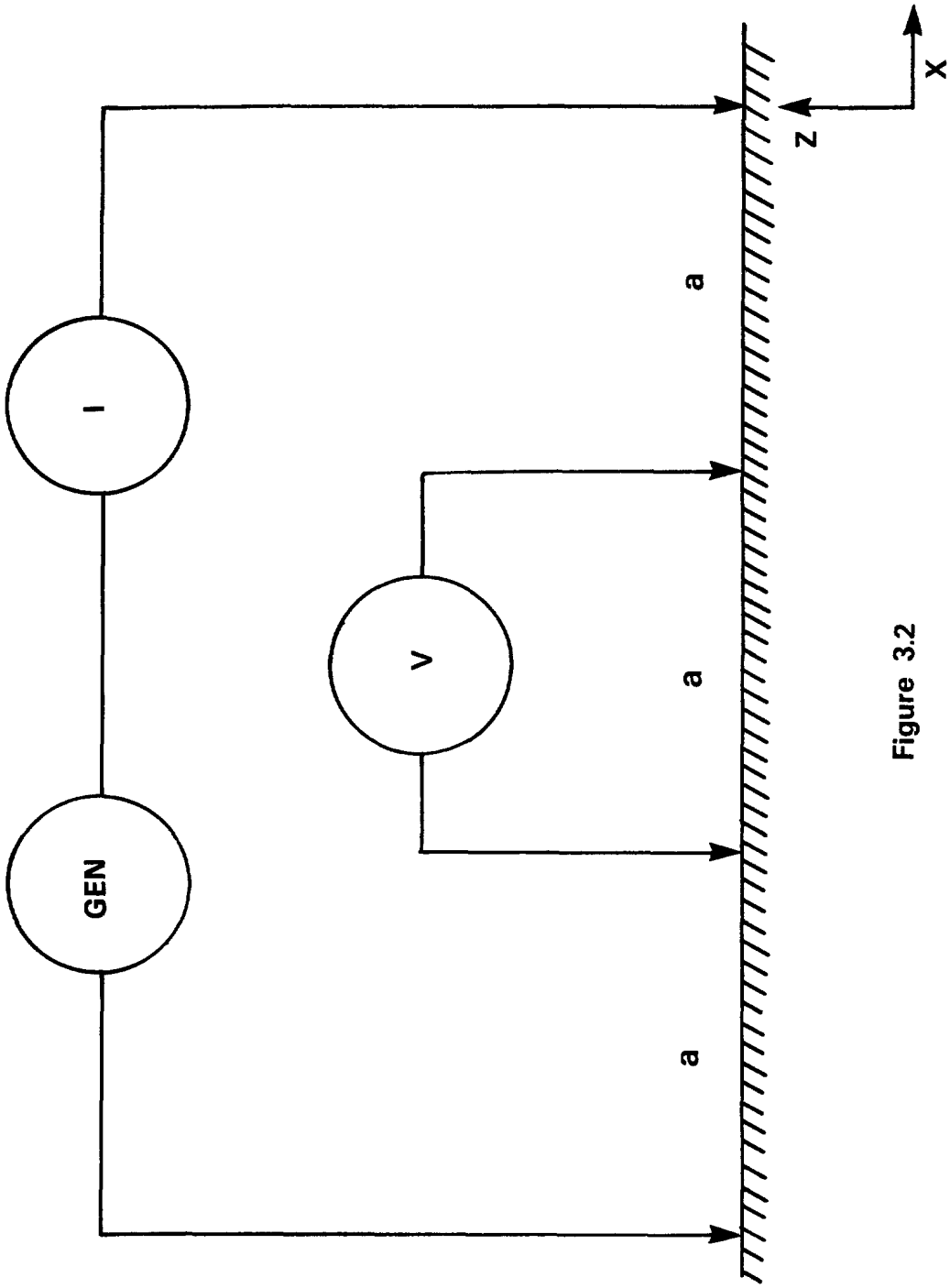

Figure 3.2

SCHEMATIC REPRESENTATION OF THE WENNER ARRAY

The parameter *a* would be increased to measure deeper layers in the medium.

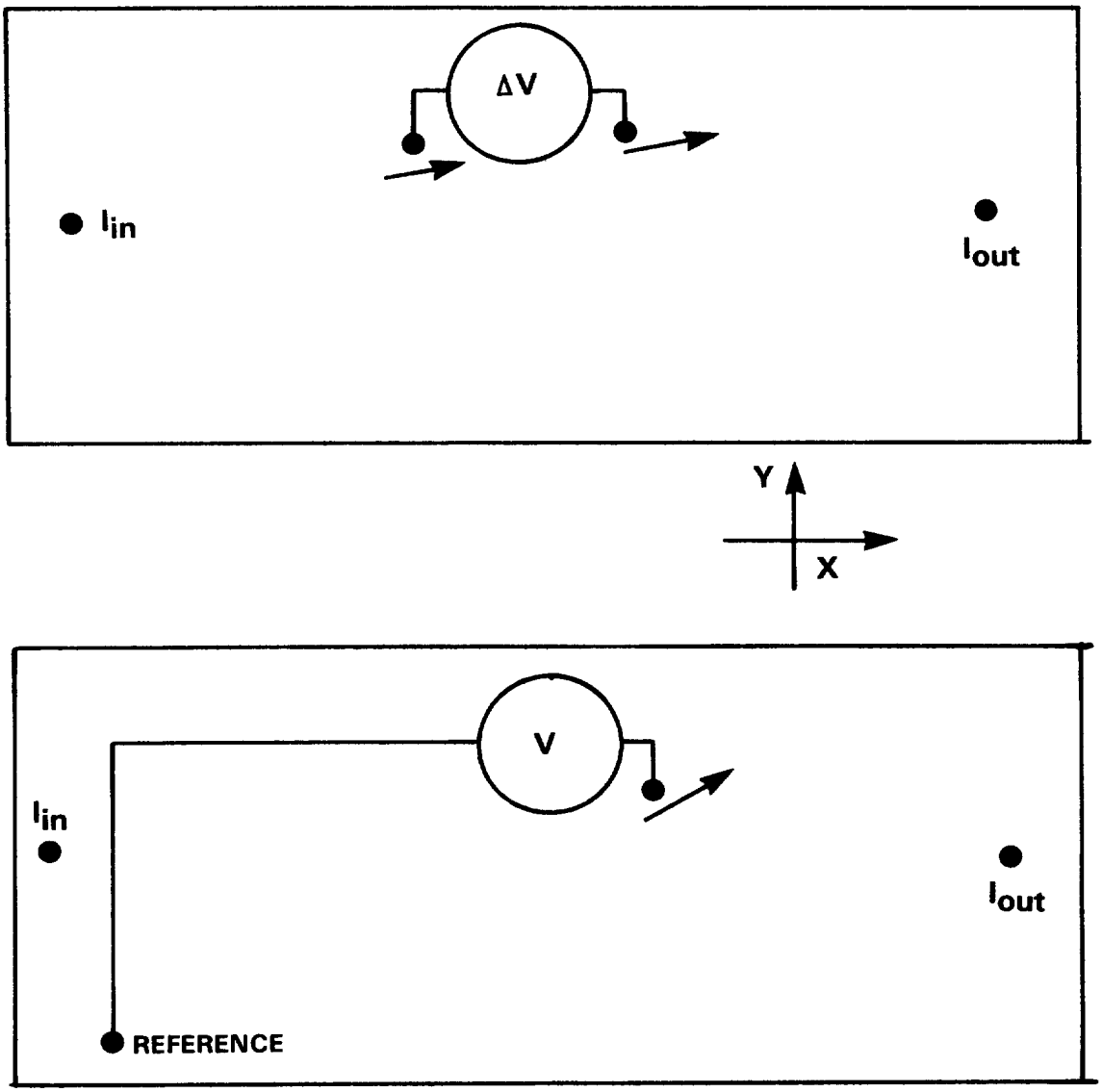

Figure 3.3

TWO SCHEMES FOR HORIZONTAL EXPLORATION

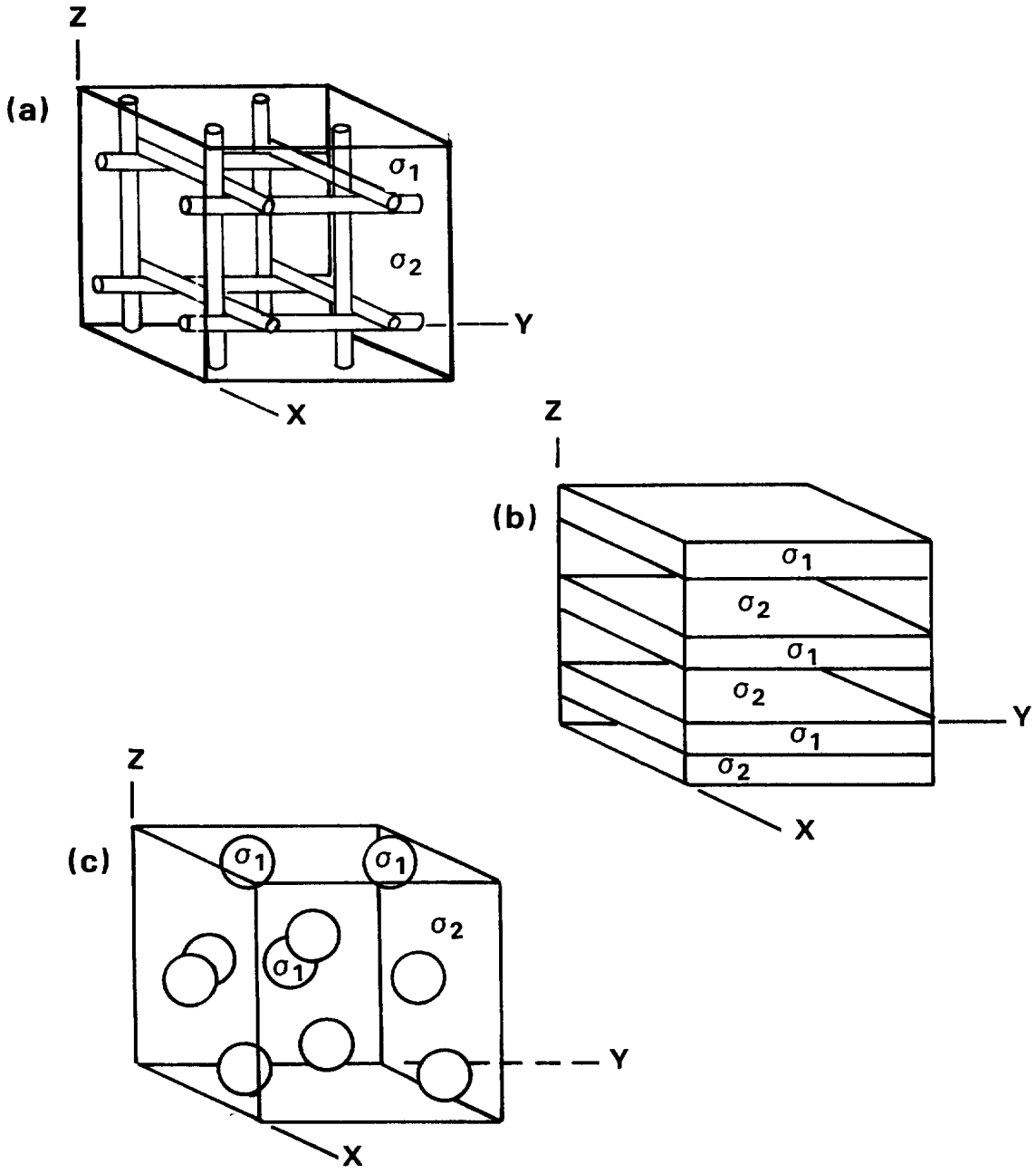

Figure 3.4

THREE MODELS OF CONDUCTIVITY ANISOTROPY

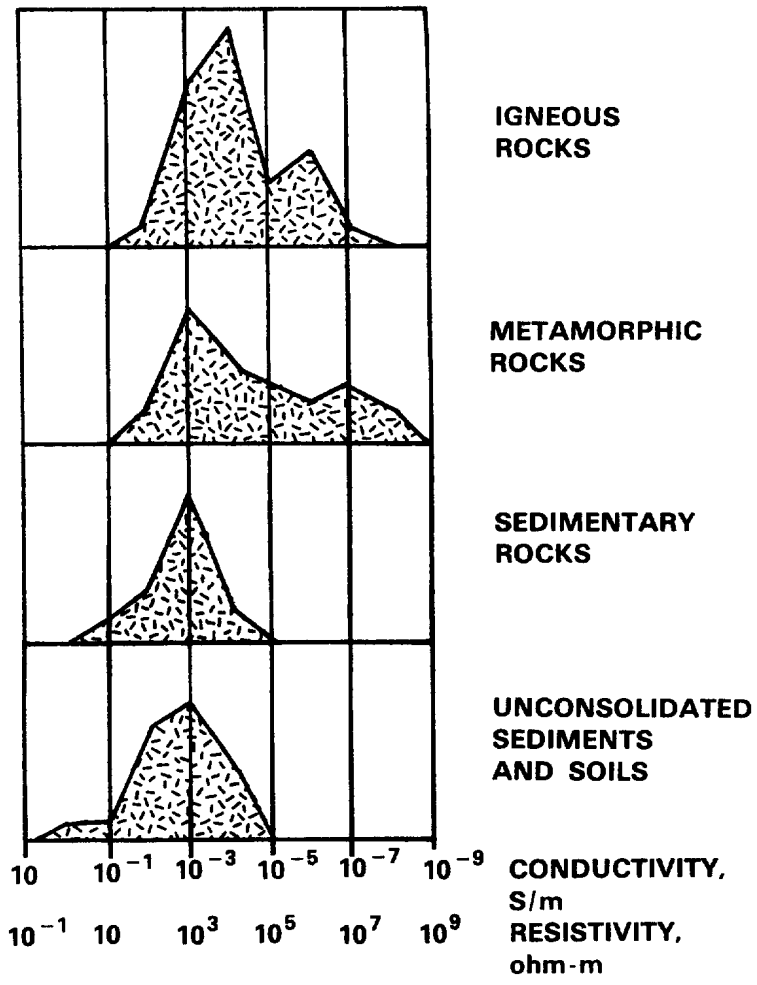

Figure 3.5

CONDUCTIVITIES OF TYPICAL ROCK TYPES
(Slichter and Telkes)

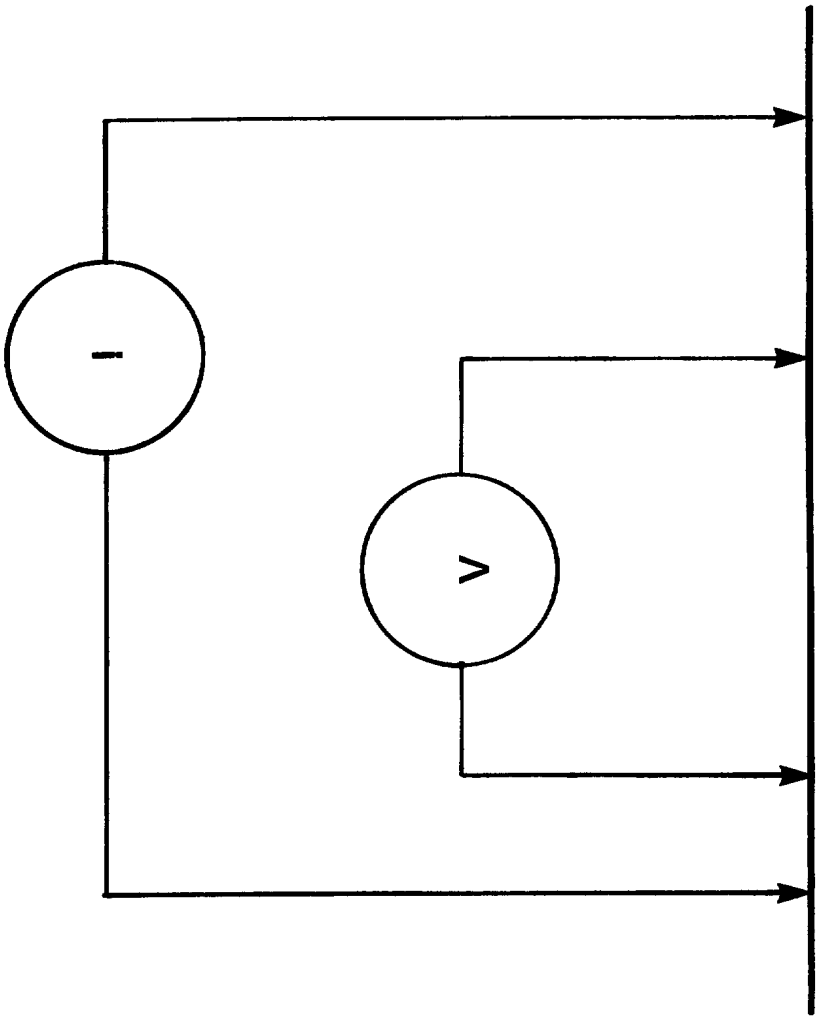

Figure 3.6
GENERAL GEOMETRY FOR RESISTIVITY MEASUREMENTS

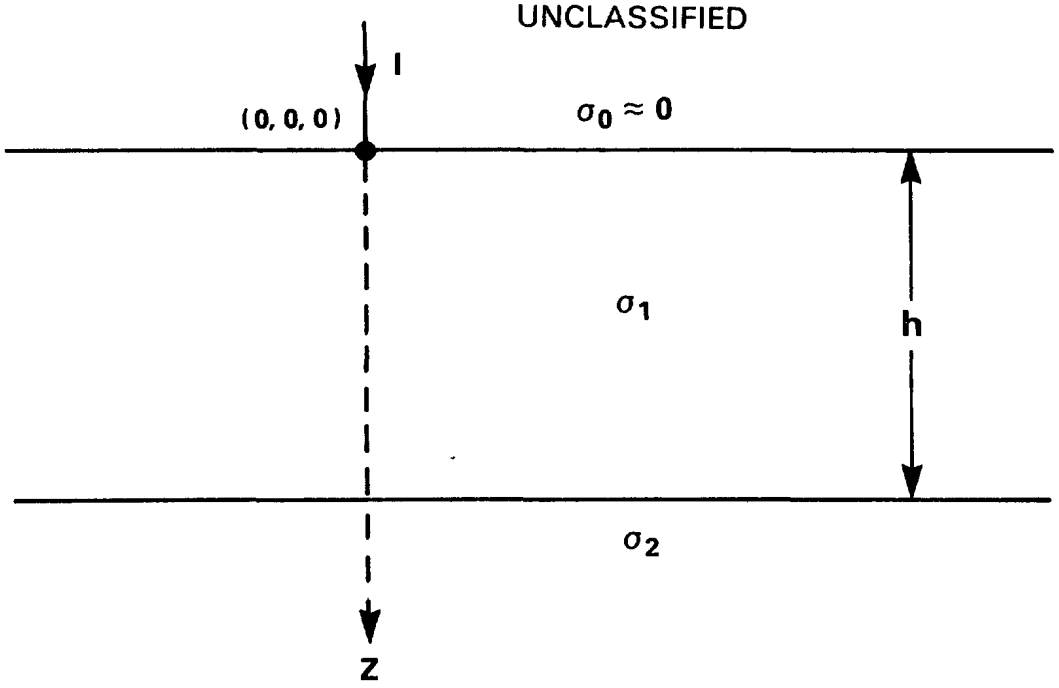

Figure 3.7

TWO LAYER EARTH GEOMETRY

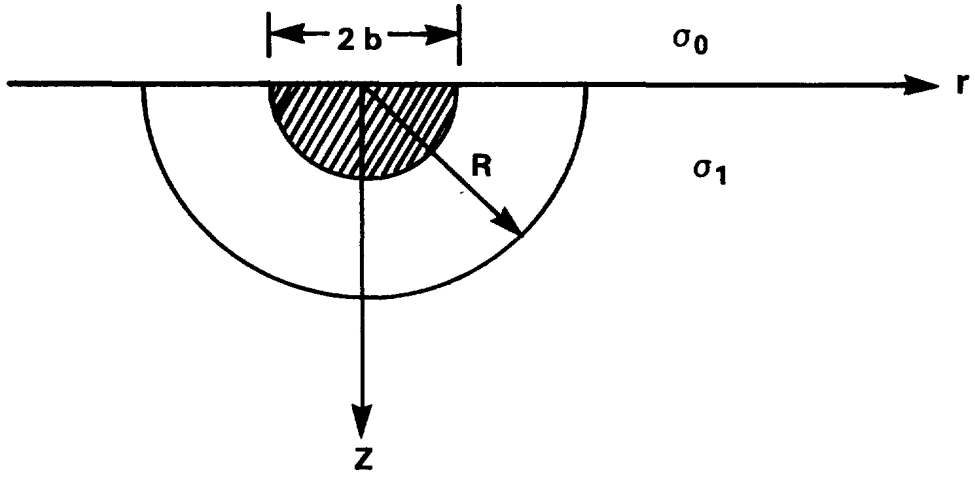

Figure 3.8

BLOWUP OF THE ELECTRODE PORTION (0, 0, 0) OF FIGURE 3.7

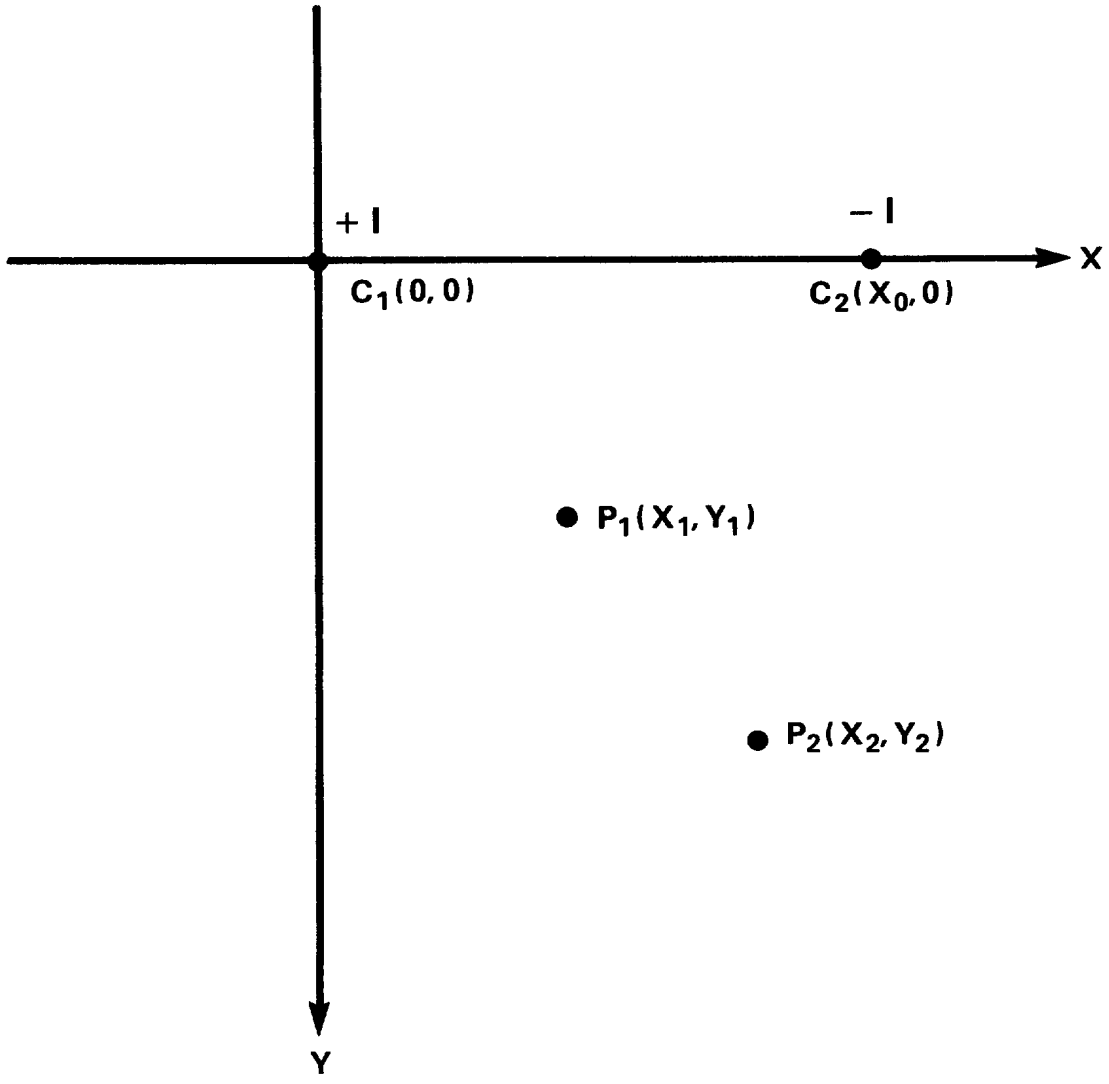

Figure 3.9

FOUR ELECTRODE GEOMETRY

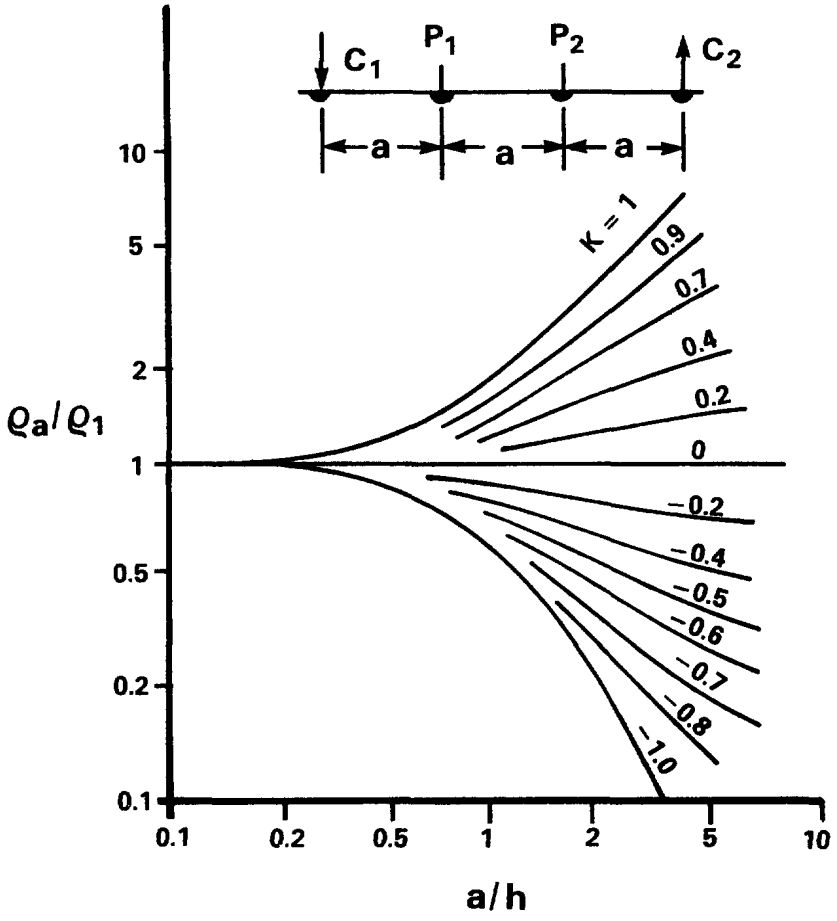

Figure 3.10

RATIO OF APPARENT RESISTIVITY TO TOP LAYER RESISTIVITY FOR 2 LAYER EARTH MODEL AND WENNER ARRAY OF SPACING *a* (Wait, 1982)
Top layer thickness is *h*. *K* is defined in text.

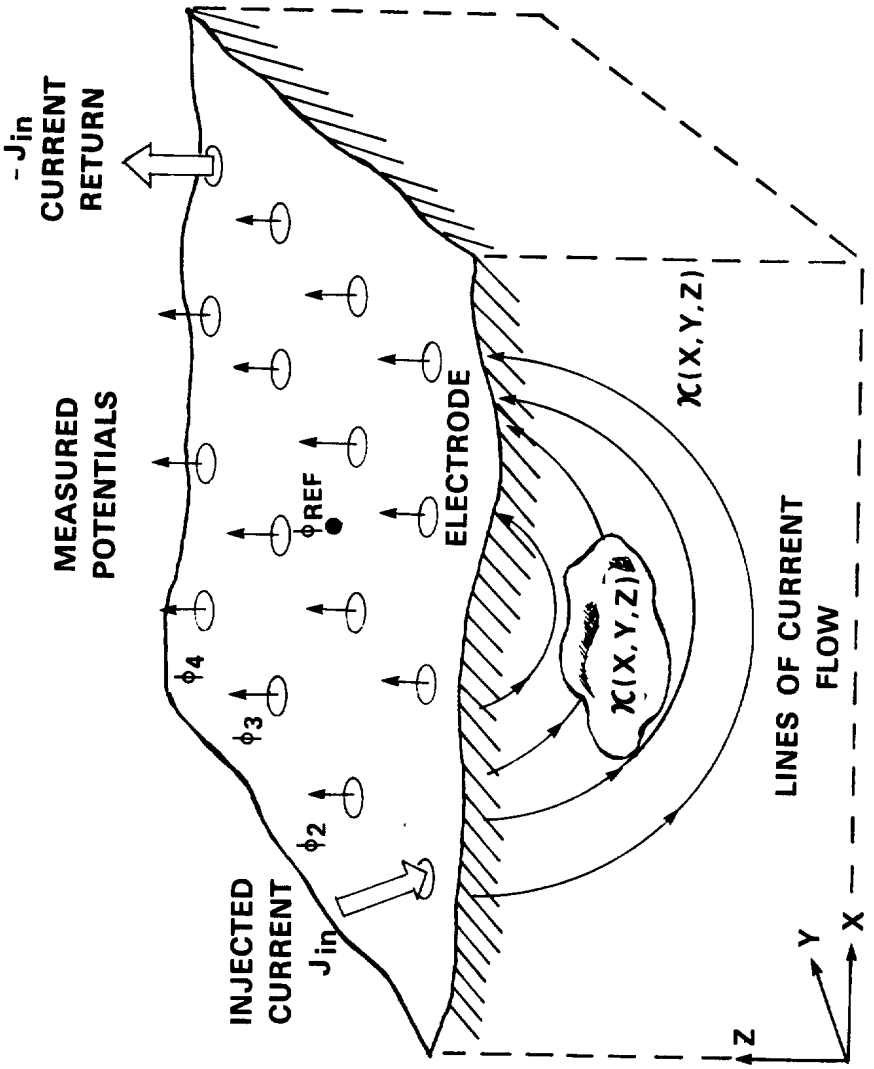

Figure 3.11

GEOMETRY FOR CONDUCTIVITY IMAGING OF HIDDEN OR BURIED COMPACT OBJECTS

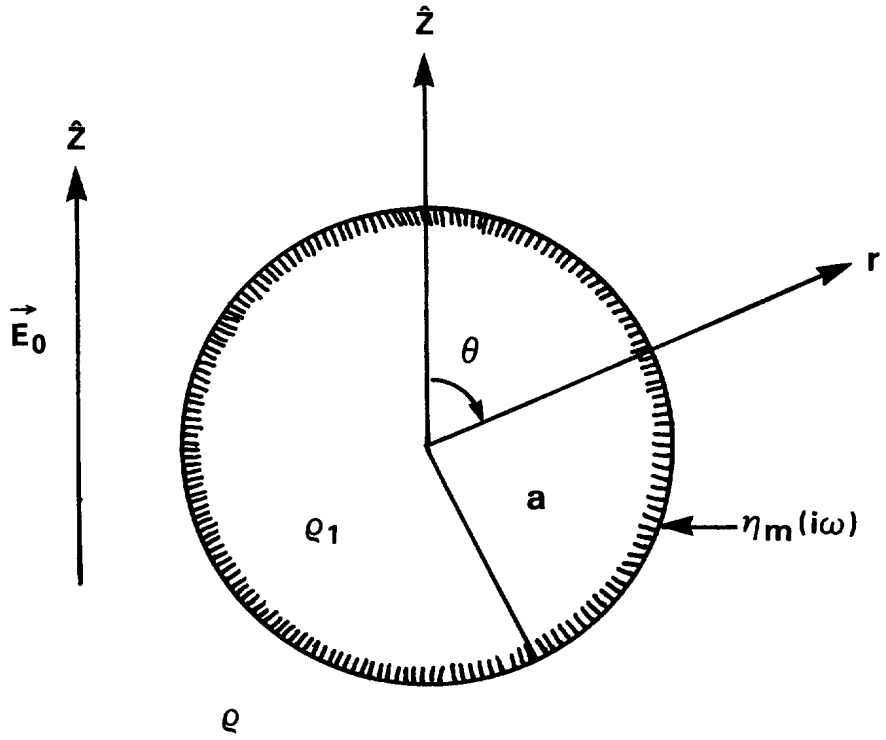

Figure 3.13

MICROSCOPIC MODEL FOR INDUCED POLARIZATION IMPEDANCE
Spherical particle has a complex surface impedance η and volume resistivity ϱ

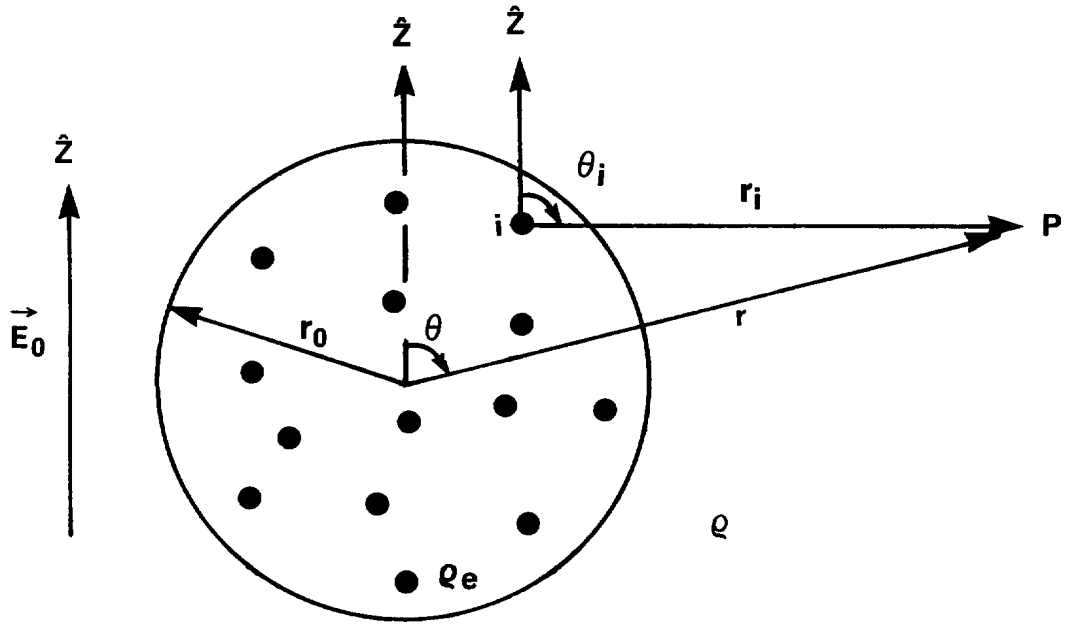

Figure 3.14

MACROSCOPIC SHPERICAL VOLUME CONTAINING A NUMBER OF IDENTICAL MICROSCOPIC SPHERES AS IN FIGURE 3.13

Figure 3.15

NORMALIZED STEP FREQUENCY RESPONSE USING THE *N*-POLE MODEL FOR RESISTIVITY

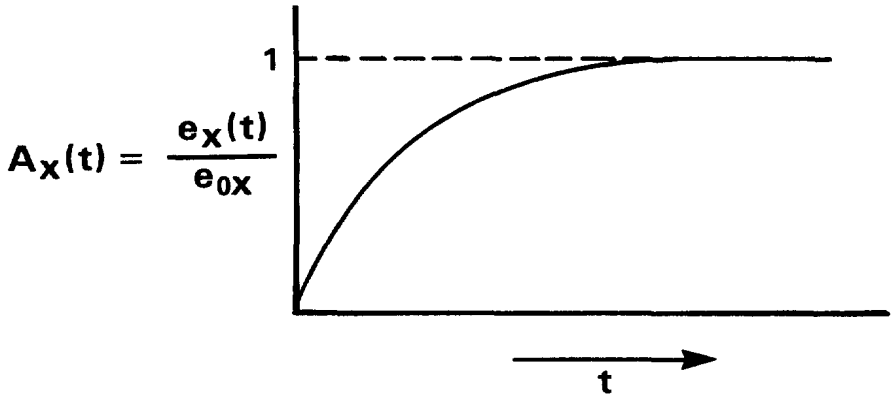

Figure 3.16

TYPICAL IMPRESSED CURRENT WAVEFORM USED IN INDUCED POLARIZATION EXPERIMENTS

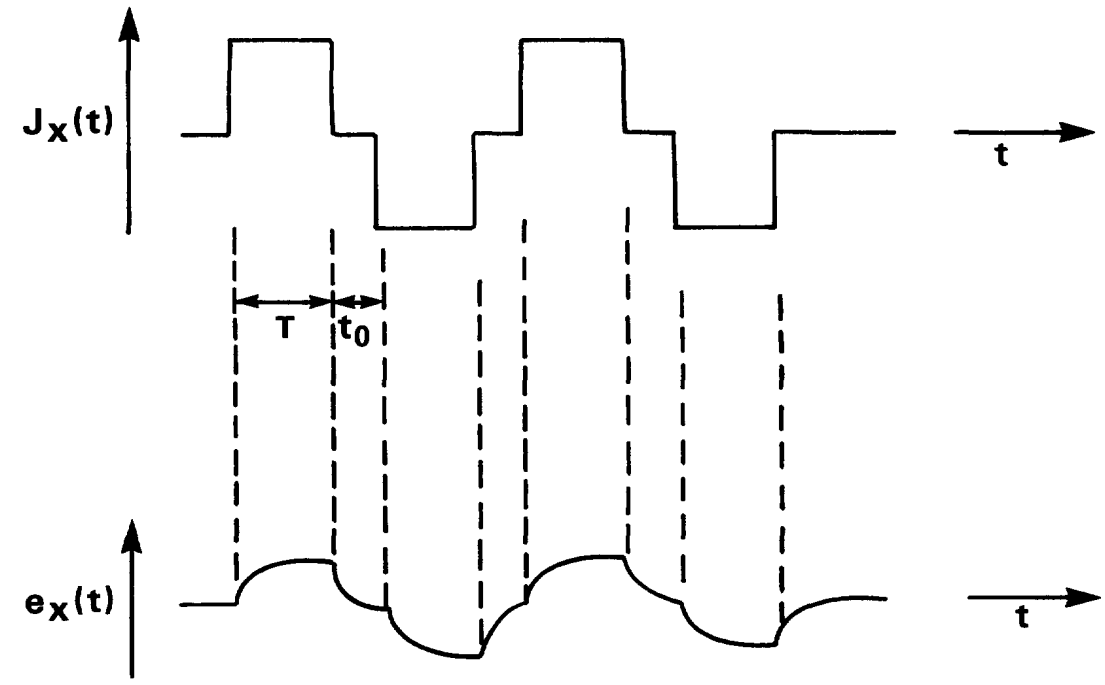

Figure 3.17

UNNORMALIZED RESPONSE TO WAVEFORM OF FIGURE 3.16 USING THE *N*-POLE MODEL FOR RESISTIVITY

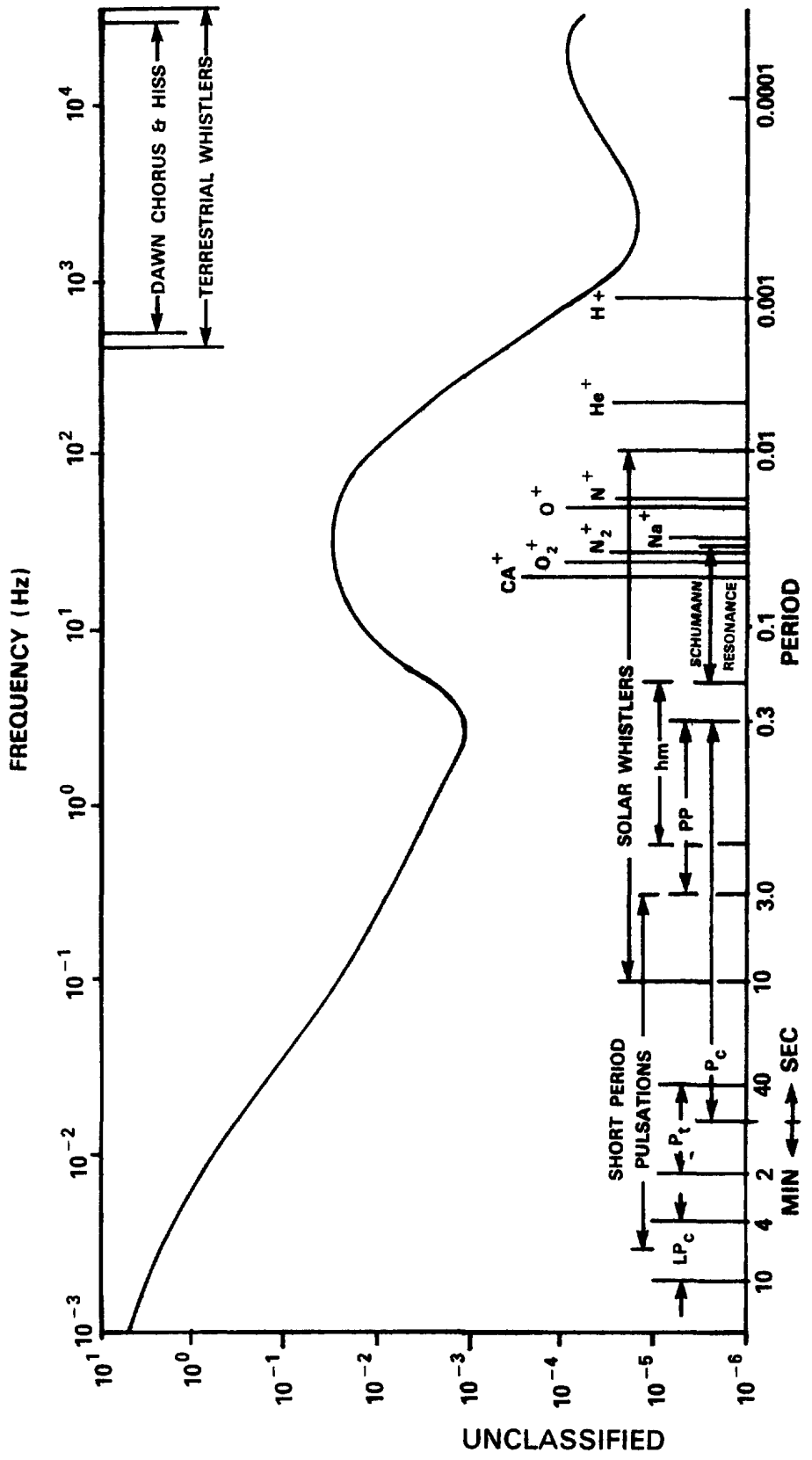

Figure 4.1

THE GEOMAGNETIC FREQUENCY SPECTRUM (Bleil)

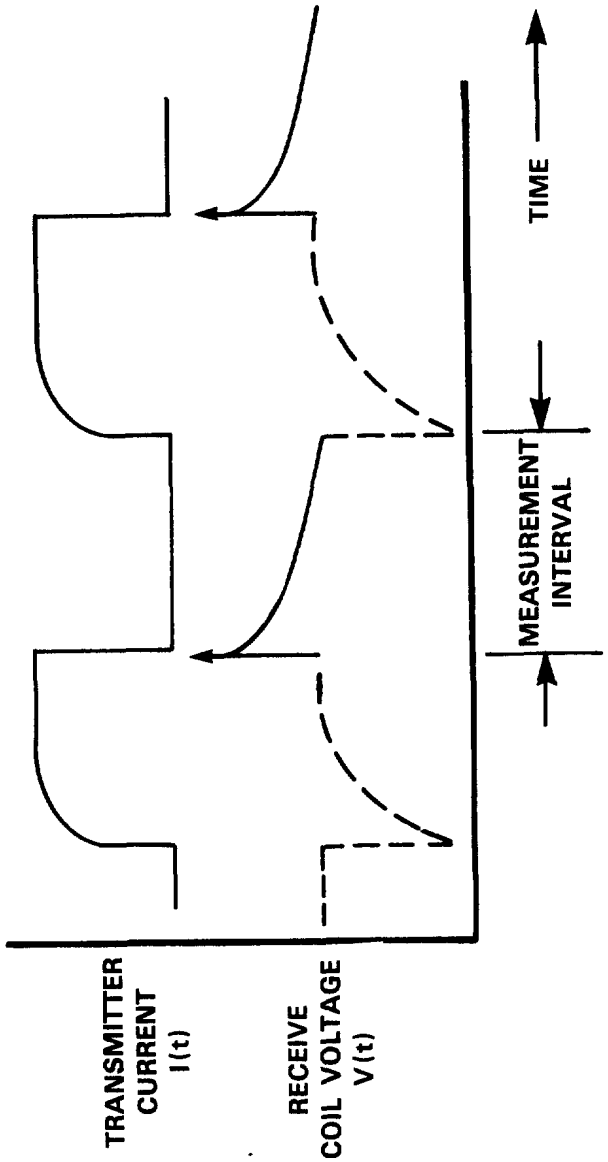

Figure 4.2

TIME DOMAIN ELECTROMAGNETIC INDUCTION ("PULSE INDUCTION") WAVEFORMS

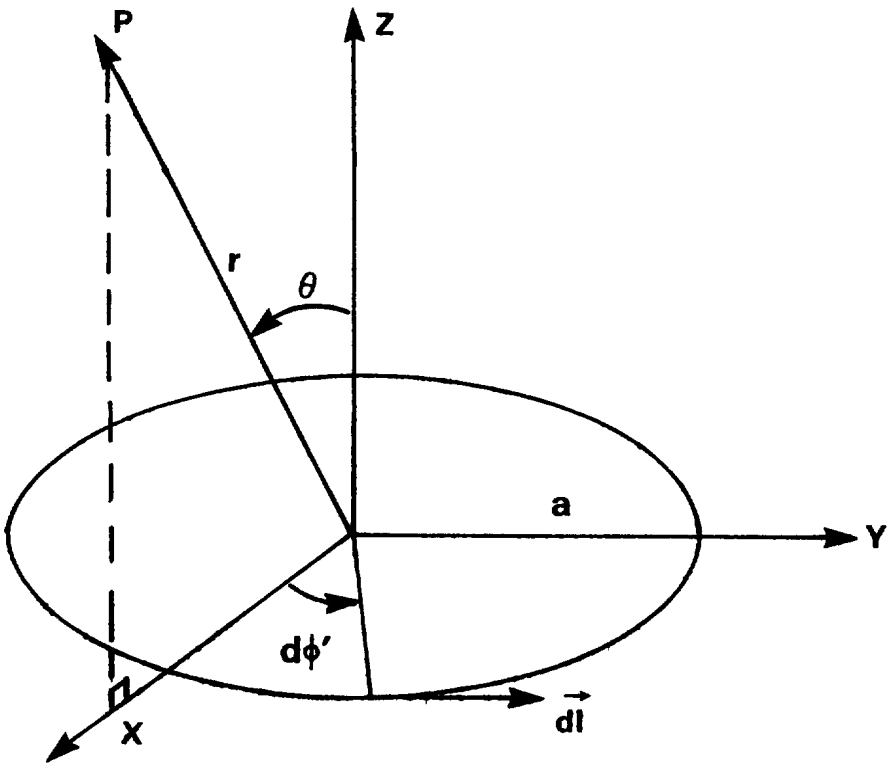

Figure 4.3

GEOMETRY OF A CURRENT CARRYING LOOP

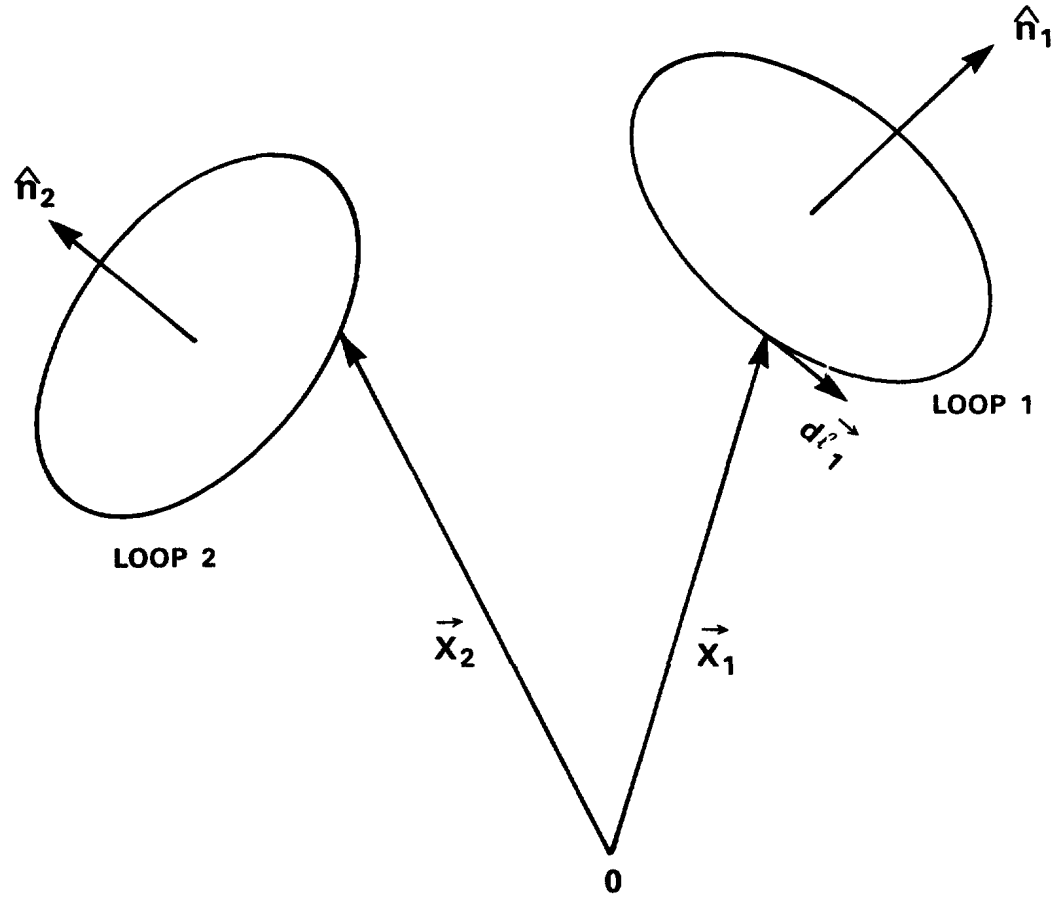

Figure 4.4

GEOMETRY FOR MUTUAL INDUCTANCE CALCULATIONS FOR TWO CURRENT CARRYING LOOPS

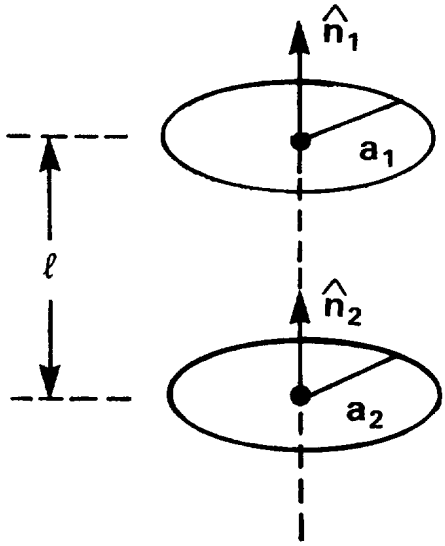

Figure 4.5a. COAXIAL GEOMETRY

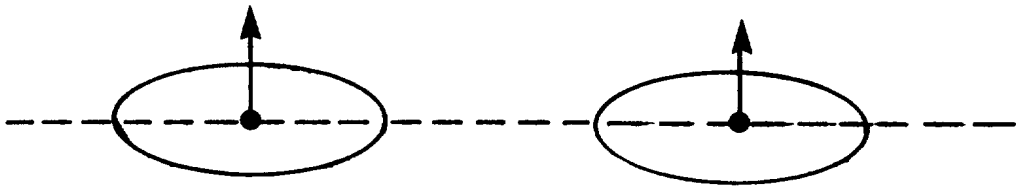

Figure 4.5b. COPLANAR GEOMETRY

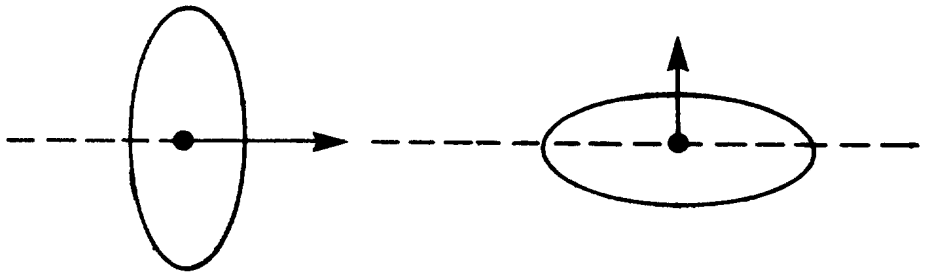

Figure 4.5c. ORTHOGONAL GEOMETRY

Figure 4.5

SPECIAL CASES FOR MUTUAL INDUCTANCE CALCULATIONS

For all cases $\ell \gg a_1, a_2$

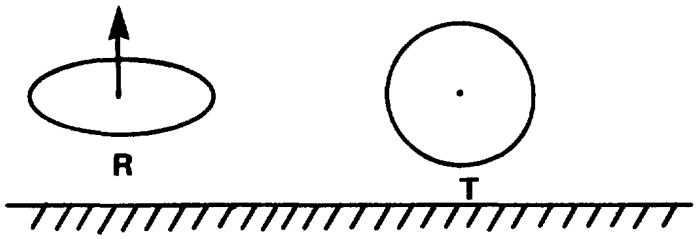

Figure 4.6a

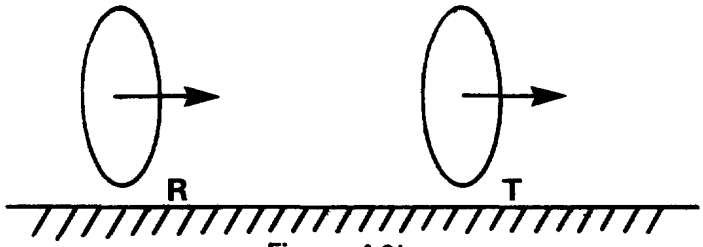

Figure 4.6b

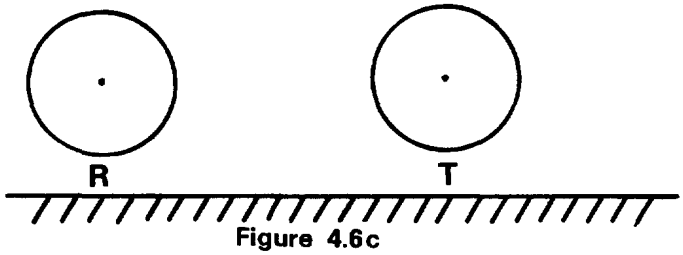

Figure 4.6c

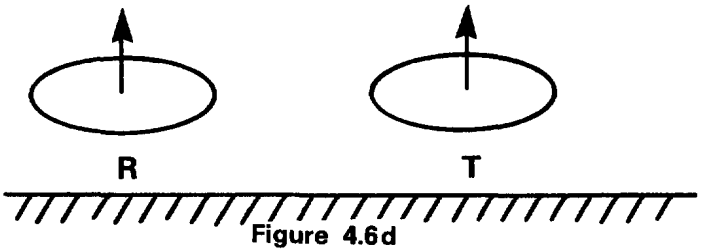

Figure 4.6d

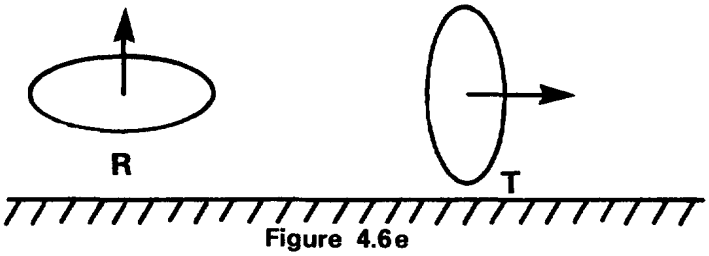

Figure 4.6e

Figure 4.6

VARIOUS COIL COUPLING GEOMETRIES FOR USE OVER AN INFINITE FLAT SHEET

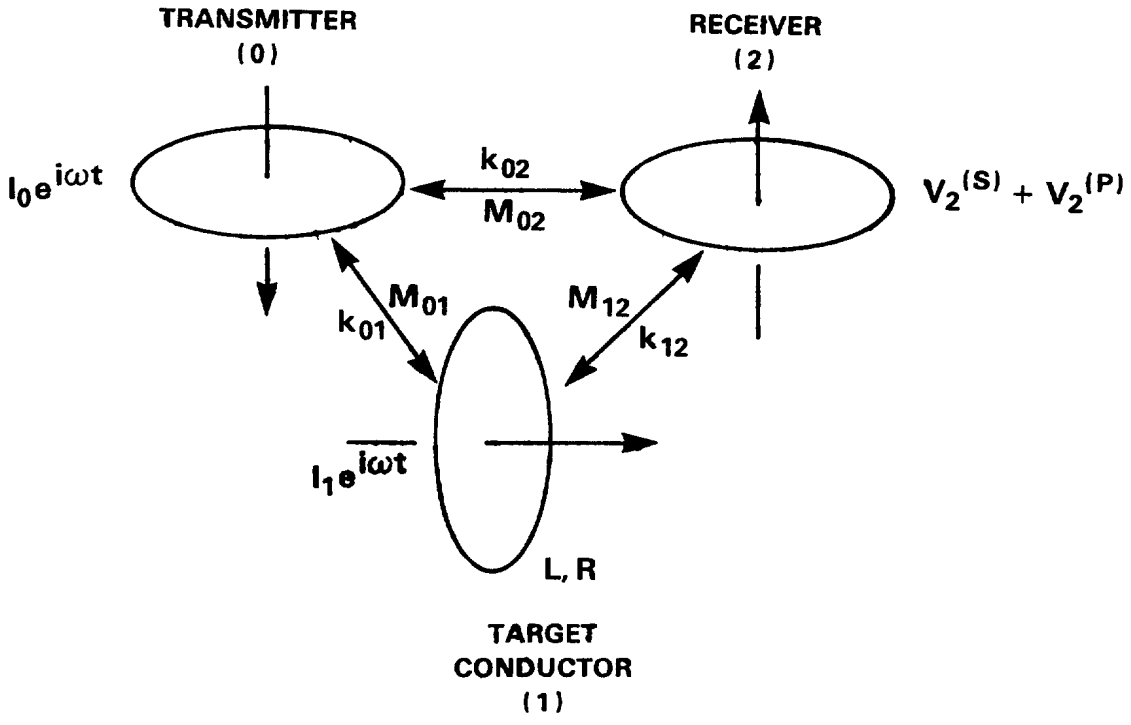

Figure 4.7

SIMPLE CIRCUIT MODEL OF ELECTROMAGNETIC INDUCTION

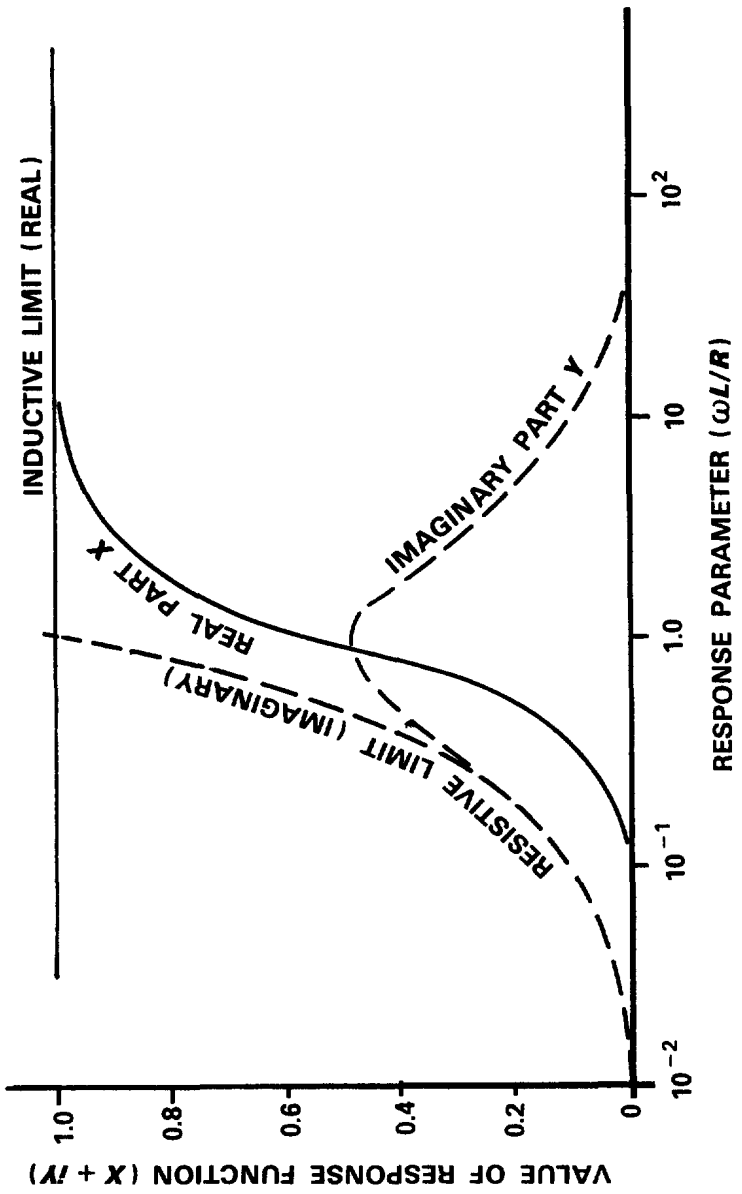

Figure 4.8

RESPONSE FUNCTION FOR SIMPLE CIRCUIT MODEL OF ELECTROMAGNETIC INDUCTION (Grant and West)

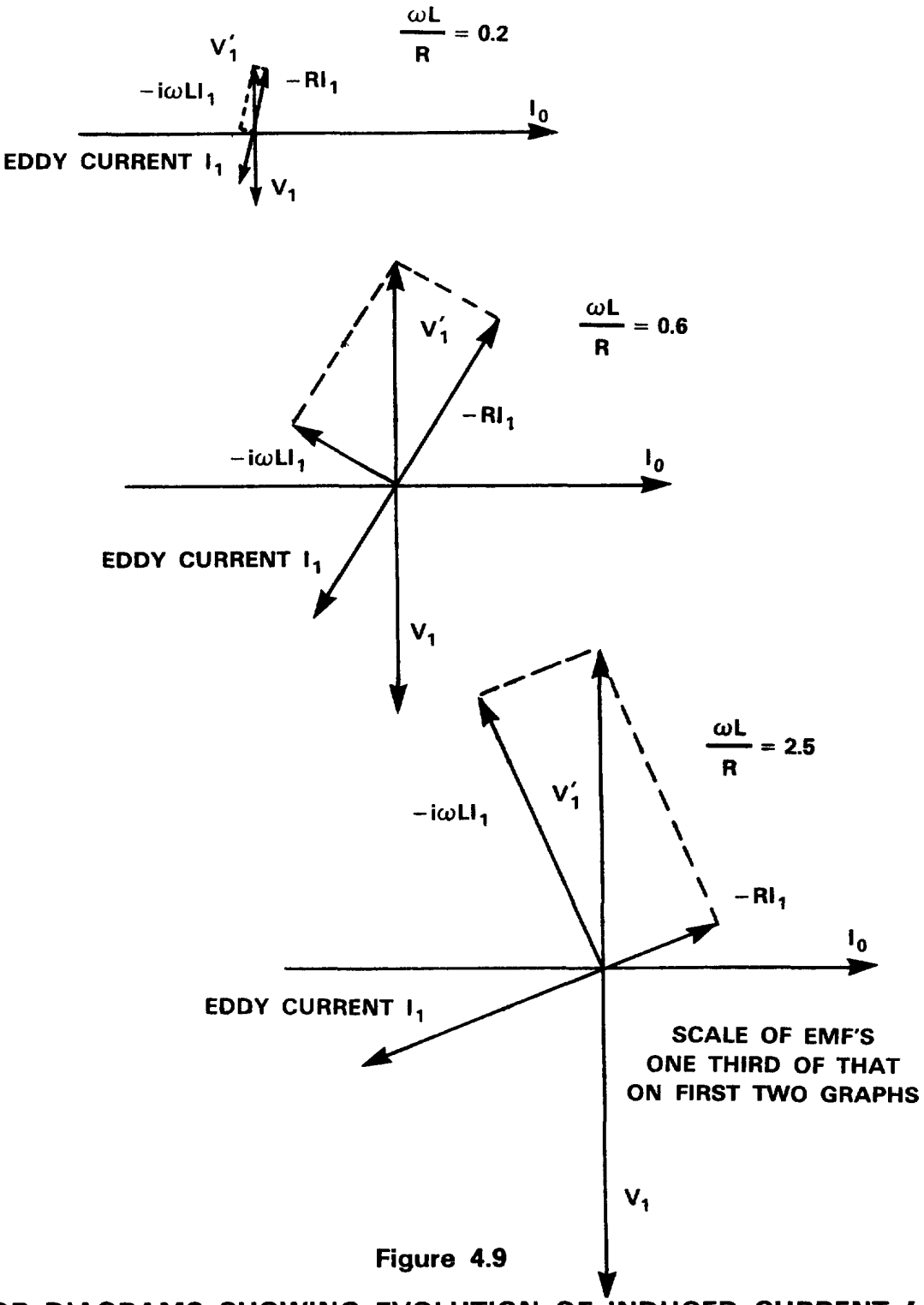

Figure 4.9

PHASOR DIAGRAMS SHOWING EVOLUTION OF INDUCED CURRENT I_1 IN TARGET CIRCUIT AS FREQUENCY ω OF INDUCING FIELD INCREASES
V_1 is due to primary magnetic field (current I_0). V_1' is due to secondary field (current I_1) (Grant and West).

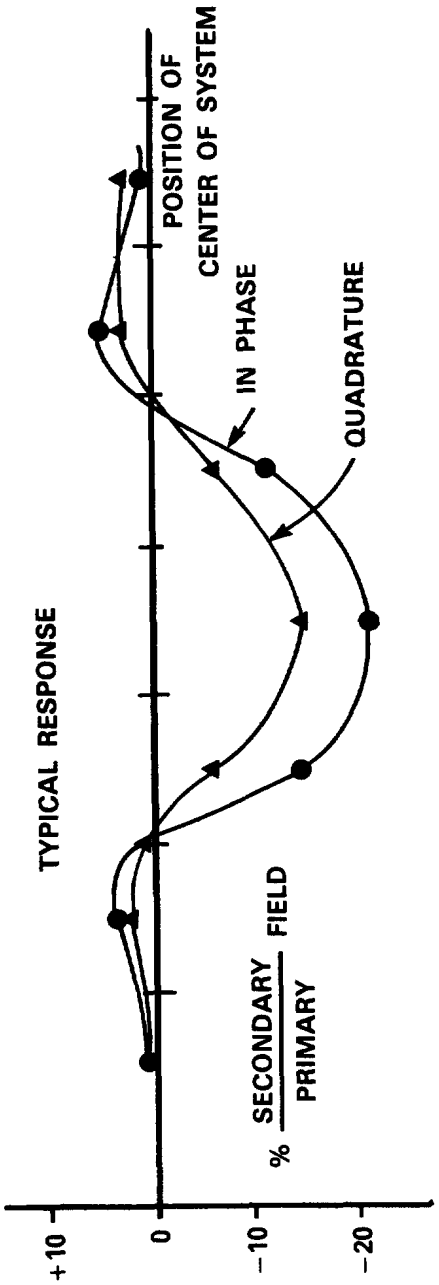

Figure 4.10

RESPONSE AS A FUNCTION OF POSITION OF SENSOR SYSTEM WITH RESPECT TO TARGET POSITION

Geometry is that of Figures 4.7, 4.11 and 4.12.

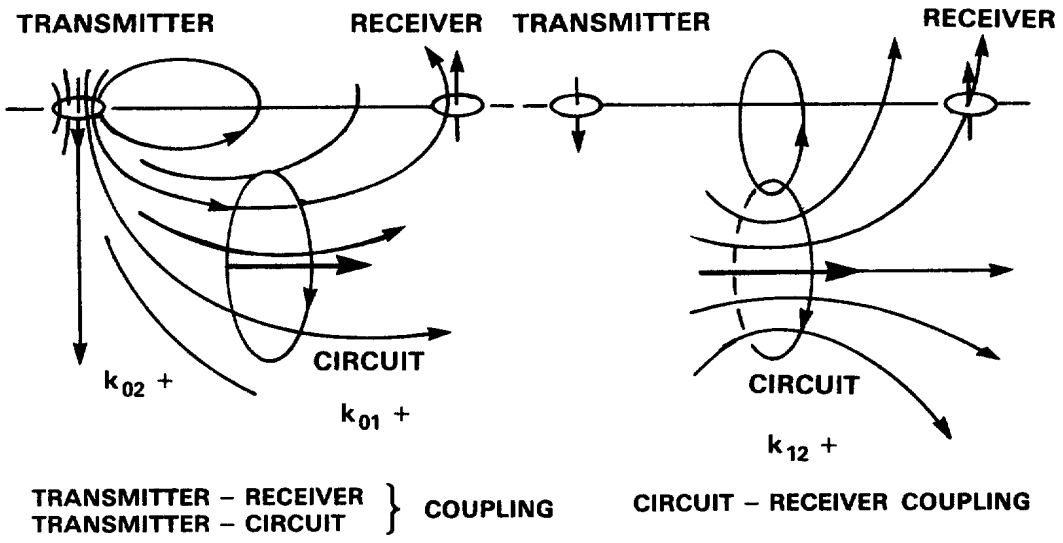

Figure 4.11

FLUX DIAGRAM TO QUALITATIVELY EXPLAIN RESPONSE OF FIGURE 4.10
In this case transmitter/receiver straddle target.

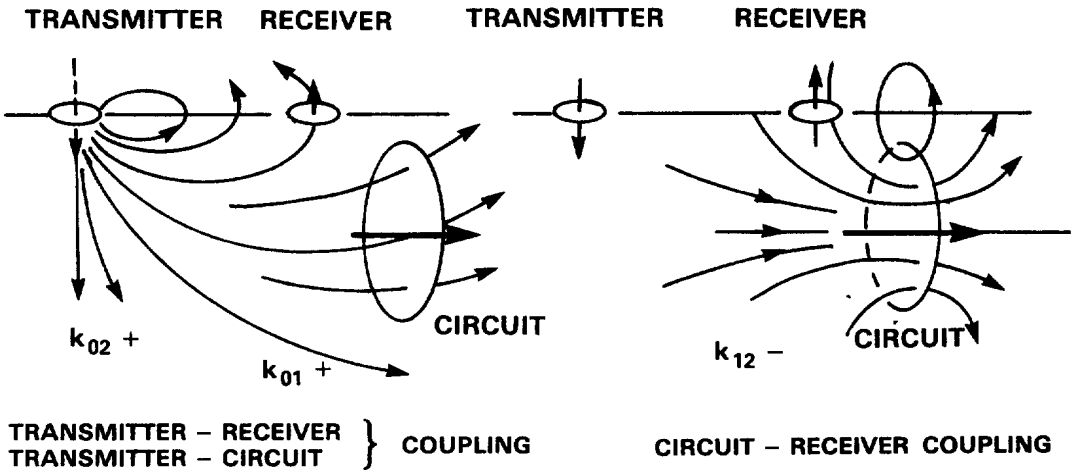

Figure 4.12

FLUX DIAGRAM TO QUALITATIVELY EXPLAIN RESPONSE OF FIGURE 4.10
In this case transmitter/receiver are to one side of target.

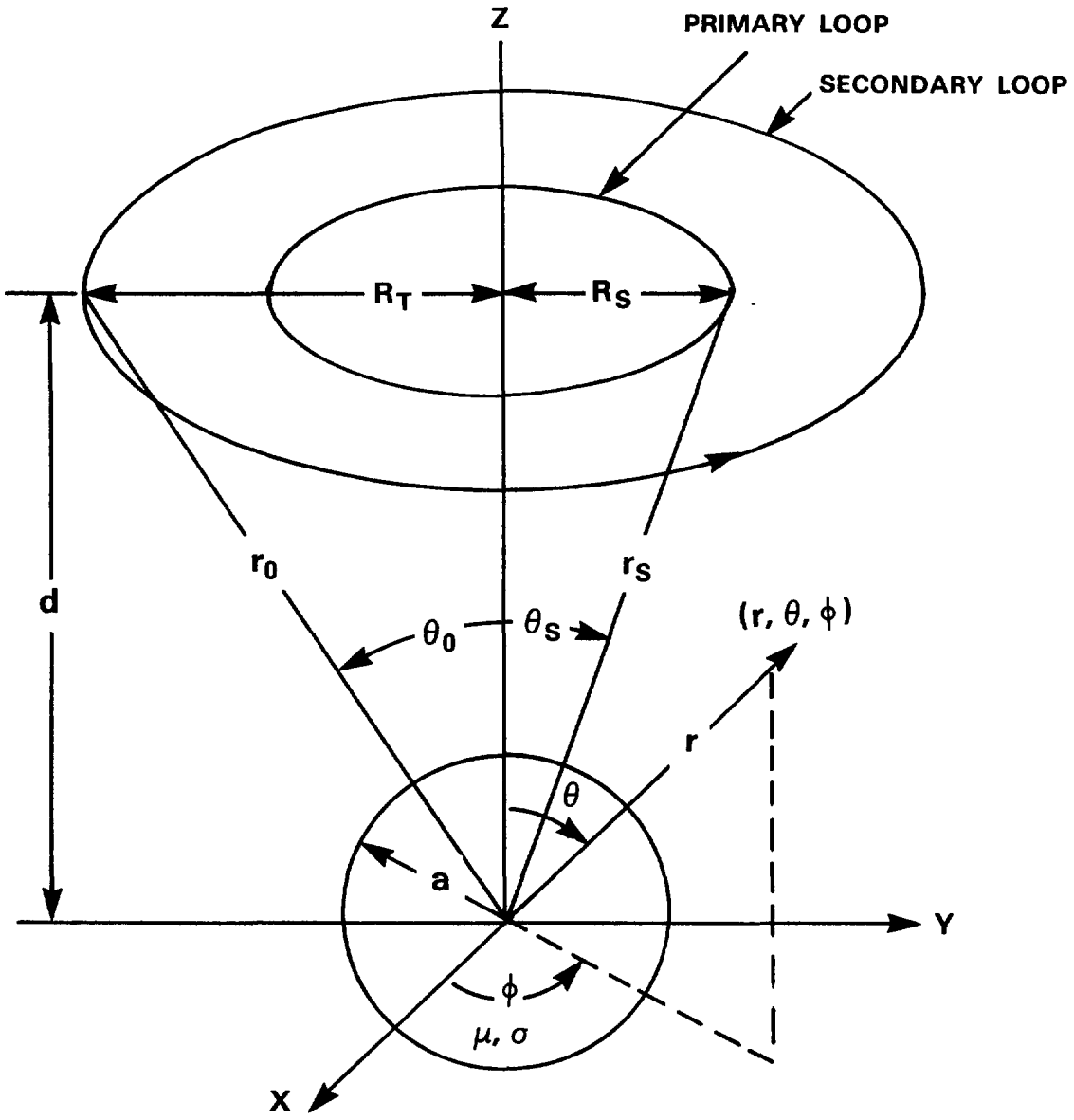

Figure 4.13

GEOMETRY FOR CALCULATION OF THE RESPONSE OF A SPHERE IN THE FIELD OF A COIL

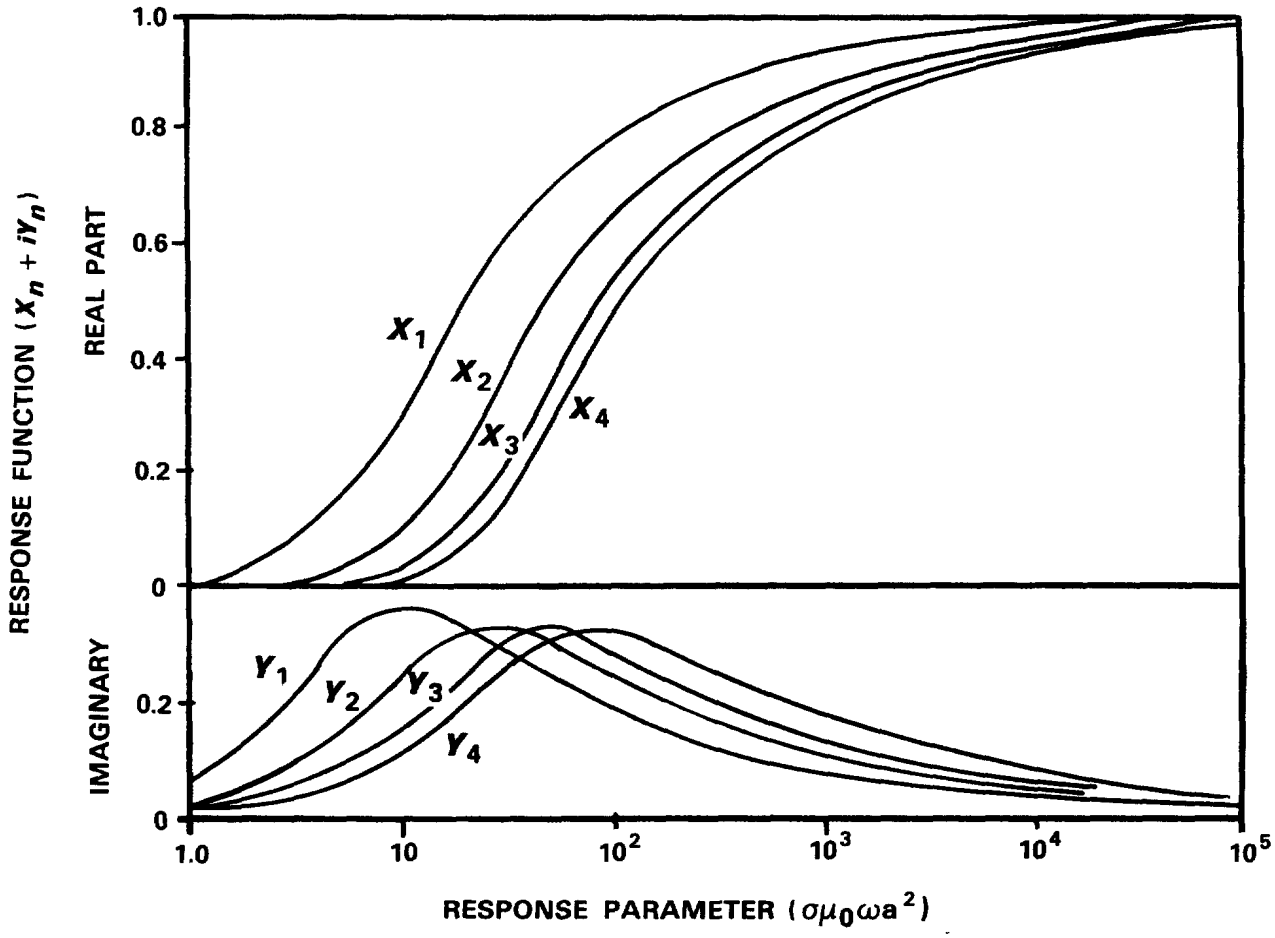

Figure 4.14

RESPONSE FUNCTIONS OF INDUCED MULTIPOLE MOMENTS FOR A SPHERICAL CONDUCTOR IN THE FIELD OF A COIL
The 4 lowest orders are shown (Wait, 1953).

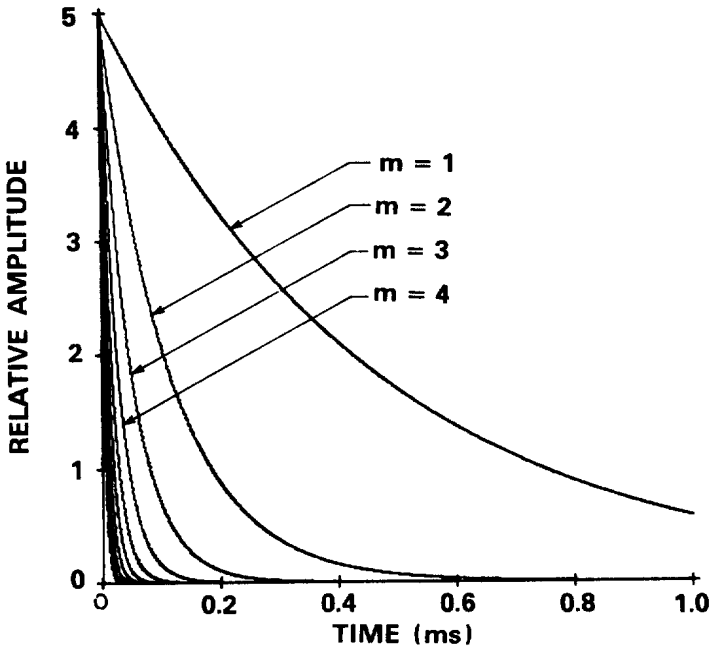

Figure 4.15

FIRST 10 TERMS OF THE TIME RESPONSE OF A MAGNETICALLY NONPERMEABLE SPHERE IN A UNIFORM MAGNETIC FIELD (Das and McFee, 1981).

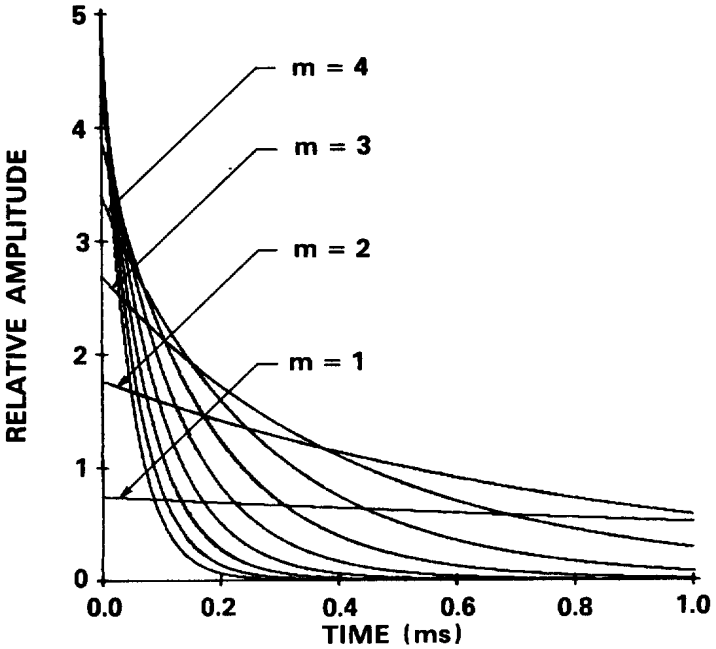

Figure 4.16

FIRST 10 TERMS OF THE TIME RESPONSE OF A MAGNETICALLY PERMEABLE SPHERE IN A UNIFORM MAGNETIC FIELD (Das and McFee, 1981).

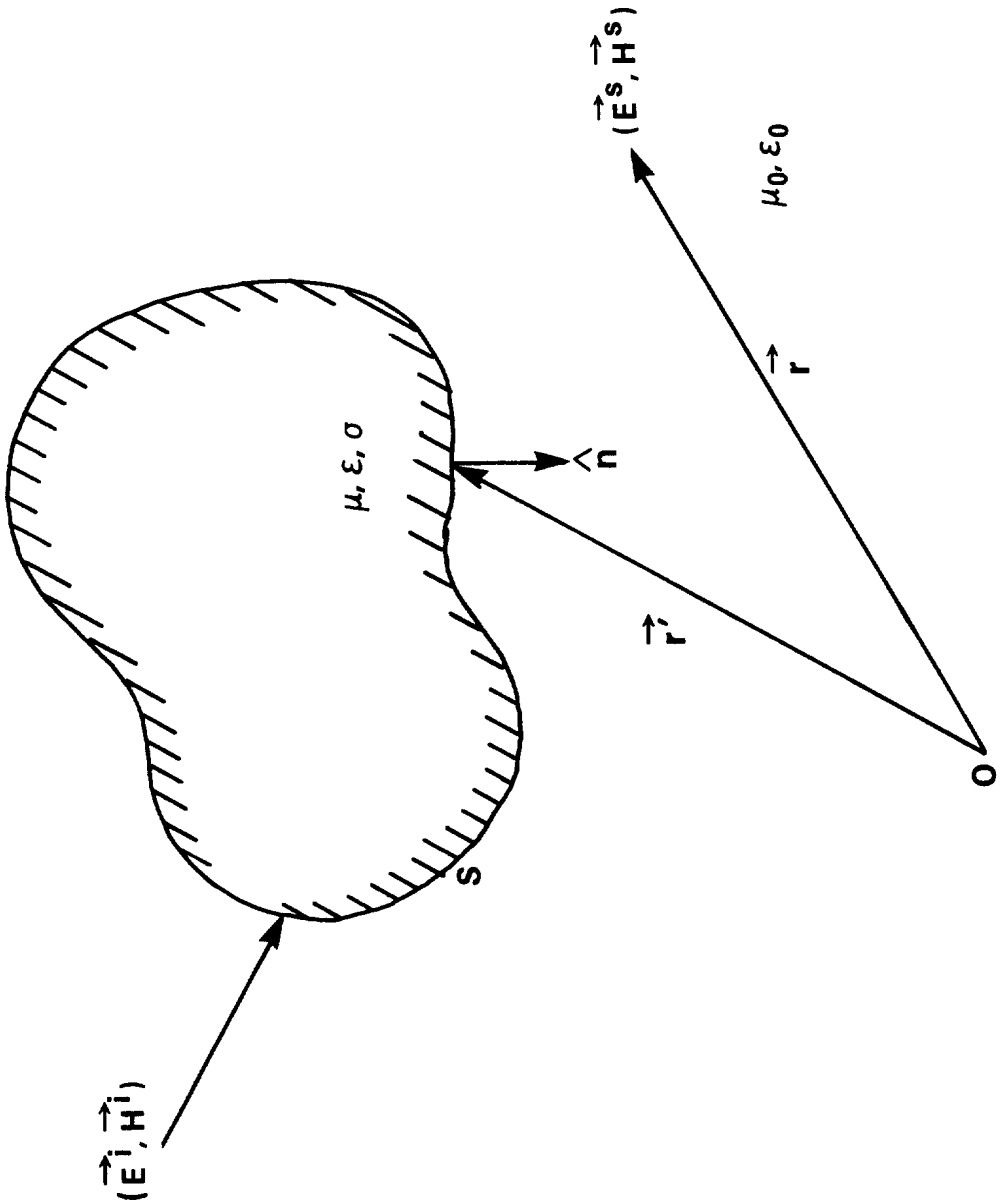

Figure 4.17 GEOMETRY FOR IMPEDANCE BOUNDARY COMPUTATIONS

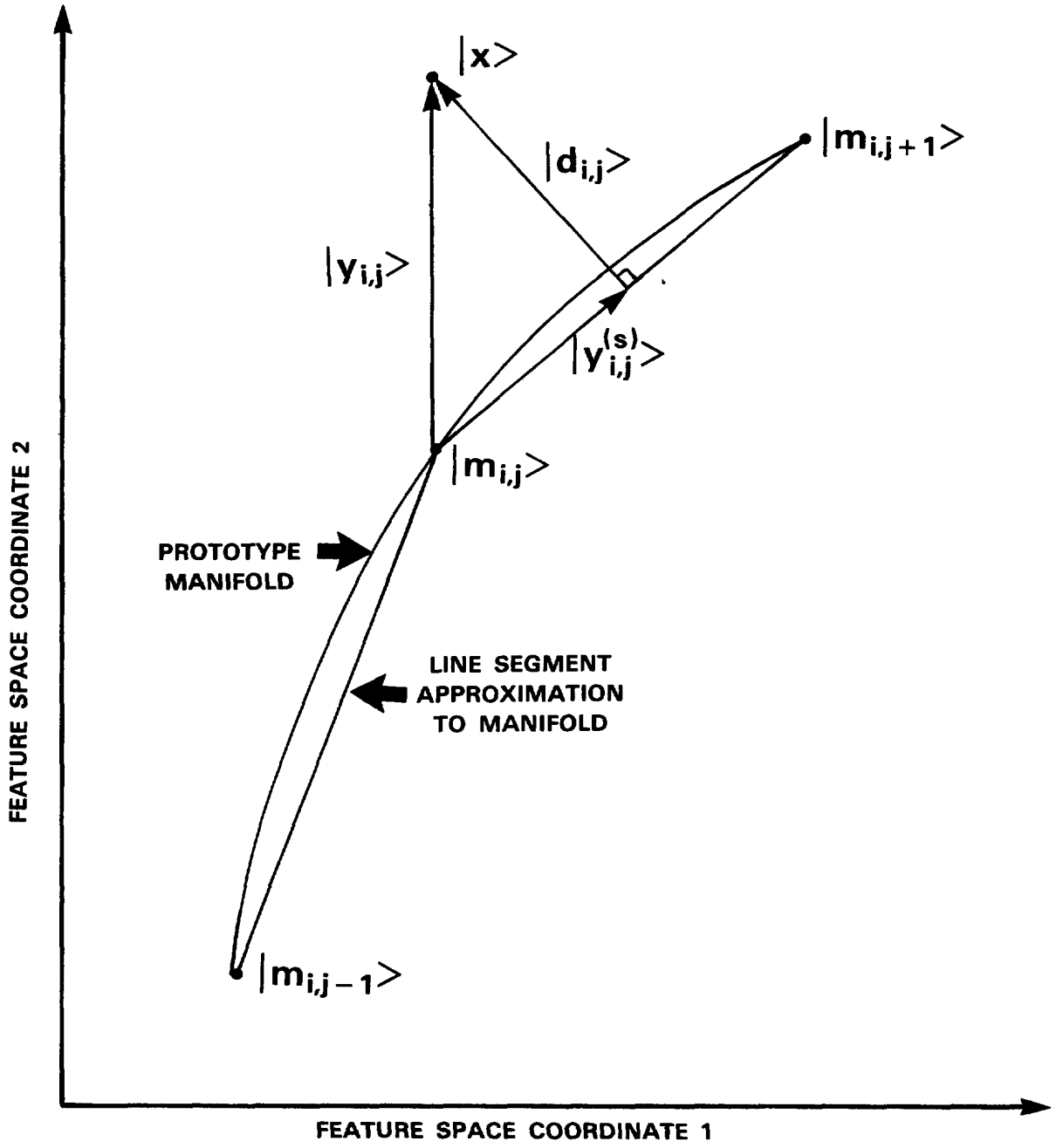

Figure 4.18

PORTION OF A ONE DIMENSIONAL PROTOTYPE MANIFOLD (A CURVE) IN AN *N* DIMENSIONAL FEATURE SPACE

(To allow it to be illustrated, the manifold has been projected onto the 2-space formed by two of its feature coordinates). Its approximation by a set of line segment unit cells is shown.

Unclassified
This Sheet Security Classification

DOCUMENT CONTROL DATA - R & D
(Security classification of title, body of abstract and indexing annotation must be entered when the overall document is classified)

1 ORIGINATING ACTIVITY Defence Research Establishment Suffield	2a. DOCUMENT SECURITY CLASSIFICATION Unclassified 2b. GROUP

3 DOCUMENT TITLE

Electromagnetic Remote Sensing:
Low Frequency Electromagnetics

4 DESCRIPTIVE NOTES (Type of report and inclusive dates)
Suffield Special Publication

5. AUTHOR(S) (Last name, first name, middle initial)

McFee, John E.

6 DOCUMENT DATE January 1989	7a. TOTAL NO. OF PAGES	7b. NO. OF REFS 85
8a. PROJECT OR GRANT NO. 031SD	9a. ORIGINATOR'S DOCUMENT NUMBER(S) Suffield Special Publication 124	
8b CONTRACT NO.	9b. OTHER DOCUMENT NO.(S) (Any other numbers that may be assigned this document)	

10. DISTRIBUTION STATEMENT

Unlimited

11. SUPPLEMENTARY NOTES N/A	12. SPONSORING ACTIVITY N/A

13. ABSTRACT

A series of lectures are presented on the topic of the location and identification of compact objects by low frequency electromagnetics. These lectures were presented as a portion of two graduate level courses in electrical engineering at the University of Toronto in 1985 and 1987. Magnetostatics, electrostatics and electromagnetic induction techniques are discussed in detail.

DSIS
78-078

KEY WORDS

Magnetics
Magnetostatics
Electromagnetic Induction
Electrostatics
Compact
Object
Detection
Location
Identification
Quasiremote
Remote Sensing

INSTRUCTIONS

1 ORIGINATING ACTIVITY Enter the name and address of the organization issuing the document

2a DOCUMENT SECURITY CLASSIFICATION Enter the overall security classification of the document including special warning terms whenever applicable

2b GROUP Enter security reclassification group number. The three groups are defined in Appendix 'M' of the DRB Security Regulations

3 DOCUMENT TITLE Enter the complete document title in all capital letters Titles in all cases should be unclassified. If a sufficiently descriptive title cannot be selected without classification show title classification with the usual one-capital-letter abbreviation in parentheses immediately following the title.

4 DESCRIPTIVE NOTES Enter the category of document, e.g. technical report technical note or technical letter If appropriate enter the type of document, e.g. interim, progress, summary, annual or final Give the inclusive dates when a specific reporting period is covered.

5 AUTHOR(S) Enter the name(s) of author(s) as shown on or in the document Enter last name, first name, middle initial. If military, show rank The name of the principal author is an absolute minimum requirement

6 DOCUMENT DATE Enter the date (month, year) of Establishment approval for publication of the document.

7a TOTAL NUMBER OF PAGES The total page count should follow normal pagination procedures, i.e., enter the number of pages containing information

7b NUMBER OF REFERENCES Enter the total number of references cited in the document.

8a PROJECT OR GRANT NUMBER If appropriate, enter the applicable research and development project or grant number under which the document was written

8b CONTRACT NUMBER If appropriate, enter the applicable number under which the document was written

9a ORIGINATOR'S DOCUMENT NUMBER(S) Enter the official document number by which the document will be identified and controlled by the originating activity This number must be unique to this document

9b. OTHER DOCUMENT NUMBER(S) If the document has been assigned any other document numbers (either by the originator or by the sponsor), also enter this number(s).

10 DISTRIBUTION STATEMENT Enter any limitations on further dissemination of the document, other than those imposed by security classification, using standard statements such as.

(1) "Qualified requesters may obtain copies of this document from their defence documentation center "

(2) "Announcement and dissemination of this document is not authorized without prior approval from originating activity "

11. SUPPLEMENTARY NOTES Use for additional explanatory notes.

12. SPONSORING ACTIVITY. Enter the name of the departmental project office or laboratory sponsoring the research and development. Include address.

13 ABSTRACT Enter an abstract giving a brief and factual summary of the document, even though it may also appear elsewhere in the body of the document itself It is highly desirable that the abstract of classified documents be unclassified. Each paragraph of the abstract shall end with an indication of the security classification of the information in the paragraph (unless the document itself is unclassified) represented as (TS), (S), (C), (R), or (U)

The length of the abstract should be limited to 20 single-spaced standard typewritten lines 7½ inches long.

14 KEY WORDS Key words are technically meaningful terms or short phrases that characterize a document and could be helpful in cataloging the document Key words should be selected so that no security classification is required. Identifiers, such as equipment model designation, trade name, military project code name, geographic location, may be used as key words but will be followed by an indication of technical context.